# Controlling Electromagnetic Surface Waves with Scalar and Tensor Impedance Surfaces

by

Amit M. Patel

A dissertation submitted in partial fulfillment
of the requirements for the degree of
Doctor of Philosophy
(Electrical Engineering)
in The University of Michigan
2013

Doctoral Committee:

Associate Professor Anthony Grbic, Chair
Assistant Professor A. John Hart, Massachusetts Institute of Technology
Professor Eric Michielssen
Professor Kamal Sarabandi

*To my grandparents, Nanoobhai and Santiben,*

who have shown me the meaning of hard work and unconditional love.

*To my parents, Madanlal and Ashaben,*

who have sacrificed everything just to give me a chance.

# ACKNOWLEDGEMENTS

I have had the privilege of working with my research advisor and dissertation committee chair, Professor Anthony Grbic. Tony, I want to thank you for support, invaluable guidance, and mentorship both in research and in other aspects of life. Your dedication to your work has truly inspired me. Additionally, I would like to thank the other members of my thesis committee, Dr. Eric Michielssen, Dr. Kamal Sarabandi, and Dr. John Hart for their service and insightful suggestions towards the completion of this work.

I would also like to express my gratitude to the many excellent teachers I've had at the University of Michigan and other schools throughout the years. In particular, I'm grateful to those who made a lasting impact on me at an early stage: Mrs. Carolyn Reid (4th grade), Mr. John Lupanoff (9th grade), Professor Edward Rothwell (MSU), Professor Leo Kempel (MSU), Professor Anthony Wojcik (MSU) and Dr. Subir Biswas (MSU). For their encouragement, I am thankful.

I would like to thank my many friends and colleagues. Ly Zhang, I am grateful for your companionship, kindness, generosity, and good nature. Mohammadreza F. Imani, I am thankful for your effort in editing parts of this thesis and more importantly, for your camaraderie from day one of graduate school. I am also grateful for my friendships with Dr. Onur Bakir, Dr. Scott Rudolph, Dr. Fikadu Dagefu, Dr. Young Jun Song, Pelumi Osoba, Yohan Kim, Michael Benson, Carl Pfeiffer, Victor Lee, Gurkan Gok, Xi Lin, and many others.

Eric Becker, Nathan Whitmore, Matthew Warpinski, Pantelis Karatsinides, Sergio

Duque, Jon Wilson, and Steve Joseph, I appreciate your patience throughout these years. You did not turn your back on our friendship even when trying times made me seem neglectful. My colleagues, office mates, and research group members at the Radiation Laboratory also deserve acknowledgement. I would like to sincerely thank you for all the good times we've had over the last six years. I also greatly enjoyed the enlightening conversations I had with Professor Dipak Sengupta.

Last, but certainly not least, I am most grateful to my parents, my sister, my brother, and my grandparents for their sacrifice, love, and unwavering faith in me. Without your support, none of this would have been possible.

# TABLE OF CONTENTS

# LIST OF FIGURES

**Figure**

# LIST OF TABLES

# LIST OF APPENDICES

**Appendix**

# ABSTRACT

Controlling Electromagnetic Surface Waves with Scalar and Tensor Impedance Surfaces

by

Amit M. Patel

Chair: Anthony Grbic

The propagation characteristics of electromagnetic waves on various isotropic (scalar) impedance surfaces have been studied for some time, in order to control surface waves and leaky-wave radiation. One and two dimensional periodic impedance surfaces as well as tensor impedance surfaces, have been explored for enhanced control of wave guidance. The desire to integrate antennas and electromagnetic devices onto the surfaces of vehicles and other platforms has driven recent interest in both scalar and tensor impedance surfaces. Great strides have been made in the design of devices based on impedance surfaces. To date, these devices are designed by first determining the surface impedance variation necessary to yield the desired performance. The surfaces are then implemented as printed-circuit board (PCB) structures consisting of a patterned metallic cladding over a grounded dielectric substrate. In other words, these two-layer structures are modeled with an idealized tensor impedance boundary condition.

In this work, we aim to capture the propagation characteristics of PCB-based ten-

sor impedance surfaces more accurately by modeling them as an impedance sheet over a grounded dielectric substrate. The impedance sheet represents the patterned metallic cladding of the PCB tensor impedance surface. Dispersion equations for scalar and tensor PCB versions are found. In addition, an extraction method is presented that allows the impedance sheet to be found using only two full-wave simulations. Using the dispersion equation and the extraction method together, the dispersion properties of the printed-circuit impedance surface can be predicted. A method for designing transformation electromagnetics devices using tensor impedance surfaces is also presented. Further, a printed leaky-wave antenna based on a sinusoidally modulated scalar impedance surface is presented.

# CHAPTER I

# Introduction

## 1.1 Background on Electromagnetic Metasurfaces

Metamaterials are materials that are structured at a subwavelength scale to exhibit desired effective material parameters. Achievable material parameters can include those not found in nature [2, 3, 4]. Metamaterials are typically designed by populating small inclusions in a three-dimensional lattice such that the resulting effective medium possesses desired bulk properties. Metasurfaces are two-dimensional equivalents of these volumetric metamaterials. They consist of scatterers or apertures, arranged along a surface, that exhibit unusual reflection, transmission, or dispersion properties [5]. Much like volumetric metamaterials, they are textured at a subwavelength scale. They occupy less space, may exhibit lower losses, and are often simpler to fabricate than volumetric metamaterials. Metasurfaces are distinct from classical periodic structures such as frequency selective surfaces (FSS), PBG (photonic band-gap), and EBG (electromagnetic band-gap) structures primarily because the lattice spacing is much smaller than a wavelength [6].

This thesis will focus primarily on impenetrable metasurfaces and their wave guidance properties. The properties of these surfaces can be described in terms of a surface impedance (analogous to material parameters for volumetric metamaterials), which relates the tangential electric and magnetics fields at the surface. Long before the

term "metasurface" was coined, the propagation characteristics of electromagnetic waves on isotropic (scalar) impedance surfaces were studied to control surface waves and leaky-wave radiation [7]. One dimensional [8] and two dimensional [9] periodic impedance surfaces as well as tensor impedance surfaces (TISs) [10, 11] have also been explored for manipulating bound and leaky waves.

## 1.2   Motivation

The desire to integrate electromagnetic devices onto the surfaces of vehicles and other existing platforms has driven interest in scalar, tensor, and periodic surface impedance in recent years. One of the more popular, and perhaps more obvious, applications of impedance surfaces is to create low profile, high gain, planar [12, 13, 14, 15] and conformal [16, 17, 18] antennas. Typically, the surface impedance variation along the device is designed to yield a desired far field pattern. For this purpose, holographic reflector antennas have been designed by recording the interference pattern between a source and a desired field distribution as a variation in surface impedance [11, 19, 20, 21, 22]. Planar Luneberg lens antennas have been designed using impedance surfaces where the surface impedance variation is designed to support surface waves with an index variation given by the Luneberg Law [23].

As an alternative to fixed surface impedance profiles, planar antennas with tunable surface impedances for dynamic beam-steering and beam-forming applications have also been designed [24, 25, 26, 27, 28]. Tunable surface impedance antennas show great promise for consuming less power and occupying less space than power-hungry phased arrays and bulky mechanical steering solutions. Fig. 1.1 shows a gimbal-based solution currently employed on UAVs for satellite communications. Planar, or conformal antenna solutions could reduce the antenna form factor while leveraging available space on the body of a vehicle for increased aperture.

Impedance surfaces have also been used to enhance the performance of existing

2

Figure 1.1: UAV with top panel removed showing bulky gimbal-based antenna steering mechanism [1].

devices. As an example, the Luneberg lens concept has been applied to horn antennas in order to enhance their directivity. In [29], one plate of a horn antenna is replaced with a variable surface impedance specially designed to create a uniform wave at the aperture of the horn. Additionally, artificial impedance substrates have been explored for antenna miniaturization and bandwidth enhancement [30, 31, 32] .

As with any technology, the current state-of-the-art has some limitations and disadvantages. Great strides have been made in the design of devices based on impedance surfaces [11, 16, 17, 18, 19, 20, 21, 22] but explanations of their design remains limited in literature. To date, these devices are designed by first determining the surface impedance (boundary condition) variation necessary to yield the desired performance. The surfaces are then implemented using printed circuit board (PCB) technology, consisting of a metallic cladding over a grounded dielectric substrate. In other words, the metallic layer of the PCB is patterned in order to achieve the desired surface impedance. In the past, the mapping between the patterned cladding and the surface impedance has been found by performing a number of eigenmode

simulations and then performing a data fit [11, 20, 22]. For the tensor-based devices, full-wave eigenmode simulations are performed (at multiple propagation angles along the surface) and a least squares fit is used to assign a single impedance tensor to each geometry. In other words, what is truly a two-layer structure (cladding and grounded dielectric) is modeled as single impedance boundary condition. A design database is constructed by repeating this procedure for various patterned metallic claddings. This procedure requires significant computational resources. This method is inherently approximate since the data is fit to the dispersion equation for a single impedance surface. Therefore, the dispersion characteristics of the PCB structure may not be accurately captured. Furthermore, the realized structures are limited to electrically thin structures so that the single surface approximation remains valid. A solid, theoretical approach for implementing idealized surface impedance profiles, particularly tensor impedance profiles, using printed-circuit structures is lacking.

In this thesis, we aim to capture the behavior of a PCB-based surface more accurately by modeling it as either a scalar or tensor impedance sheet over a grounded dielectric substrate. The impedance sheet models the subwavelength-patterned metallic cladding. The dispersion equations are found for both the scalar and tensor cases. Extraction methods are presented that allow the scalar or tensor sheet impedance to be found using one or two full-wave simulations, respectively. Using the dispersion equations and the extraction methods together, the electromagnetic properties of a PCB-based surface can be analytically predicted with accuracy.

One cutting-edge application of impedance surfaces includes a class of waveguiding structures. Devices such as polarization splitters, beams-shifters, collimators, beam-benders and cloaks based on transformation electromagnetics/optics concepts [33, 34] have been realized with metamaterial transmission lines [35, 36, 37, 38] or inside parallel plate wave guides [39] by using anisotropic material parameters. However, they have only recently been implemented with impedance surfaces [40]. In

transformation electromagnetics, a field distribution can be transformed from an initial state to a desired state through a change in material parameters via a coordinate transformation [33]. The fact that all space is transformed using this method poses a hurdle for the design of antennas and surface-wave structures that require the free space above the surface to remain untransformed. A method for designing transformation electromagnetics devices using TISs, which transforms the TIS alone, without transforming the space above the TIS, will be presented in this thesis. The design and implementation of these transformation electromagnetics-based surfaces as printed-circuit structures is also explored.

## 1.3   Goals

The goal of this thesis is to advance the state-of-the-art in scalar and tensor impedance surfaces by advancing the theoretical understanding of these surfaces, and addressing the limitations of the current implementation methods. The objectives of this thesis are organized into four main thrusts:

1. To provide improved understanding and intuition into the guidance characteristics of idealized scalar and tensor impedance surfaces. In the case of tensor impedance surfaces (TISs), this includes understanding the contributions of $TM$ and $TE$ modes as well as determining the group and phase velocities. This will enable the design of structures that support desired phase progression and power flow.

2. To develop step-by-step methodologies to design subwavelength textured surfaces that allow the desired control of the fields along the surface. The work will address questions such as: "How should the surface impedance profile vary along the surface?". Specifically, the sinusoidally modulated reactance surface (SMRS ) method (Ch. II), and a transformation electromagnetics method

(Ch. V) will be used to design surface impedance profiles. The transformation electromagnetics-based method allows wave vector and Poynting vector distributions to be specified on the surface. Additionally, it allows the surface to be transformed without transforming the free space above it, making it suitable for antenna applications.

3. To provide a tool-kit for not just the design, but also the implementation of devices based on metasurfaces using PCB technology. With the proposed two-layer model, the surface is represented as an impedance sheet over a grounded dielectric substrate. The sheet represents a subwavelength-patterned metallic cladding. We aim to answer the question, "What should the impedance sheet be in order achieve prescribed guidance properties?" The answer to this question brings us one step closer to answering the ultimate question, "How should the metallic cladding be textured in order achieve prescribed guidance properties?" The tool-kit minimizes the need for time-consuming full-wave simulations and least-squares approximations used in the past to characterize metasurfaces and construct a design database. The proposed modeling approach will yield more accurate results (within the homogenous limit), and in a shorter amount of time than earlier methods. Additionally, surfaces with arbitrary thicknesses can be analyzed.

4. To design and fabricate prototype devices using both scalar and tensor impedance surfaces to verify and demonstrate the utility of the proposed design procedures.

## 1.4   Thesis Outline

This thesis will address both scalar and tensor impedance surfaces. Each of these will have a theory associated with the idealized surface. Additionally, design methods will be introduced, which allow the designer to find the necessary surface impedance

variation to design devices. Lastly, implementation of these surfaces with PCBs, and the associated challenges, will be discussed. Prototype devices will be implemented to verify the design procedures and PCB implementation methods. The chapters of the thesis are structured such that each chapter includes the analysis of an idealized surface and its practical realization. This allows the idealized and practical structures to be easily compared.

### 1.4.1 Chapter II: Sinusoidally-Modulated Scalar Impedance Surfaces

Chapter II will present a step-by-step method for designing a scalar, SMRS, capable of radiating at an arbitrary off-broadside angle. The procedure allows for nearly independent control of the leakage and phase constants along the surface. Printing an array of metallic strips over a grounded dielectric substrate is discussed as a way to practically implement the theoretical SMRS. A method for mapping gaps between metallic strips to a desired surface impedance is presented as an efficient alternative to mapping methods used in the past. A printed leaky-wave antenna with a sinusoidally-modulated surface reactance is designed using the proposed method. The TM-polarized antenna radiates at 30° from broadside at 10 GHz, and exhibits an experimental gain of 18.4 dB. Theoretical, simulated, and experimental results are reported. The SMRS method is closely related to a holographic method. It provides added insight into the operation of holographic surfaces reported earlier [11, 19, 20].

### 1.4.2 Chapter III: Analytical Modeling and Dispersion Analysis of a Printed-Circuit Tensor Impedance Surface (PCTIS)

Chapter III is dedicated to TISs. Specifically, the idealized tensor impedance boundary condition (TIBC) and its practical realization as a printed-circuit tensor impedance surface (PCTIS) are studied. The eventual goal of this study is to design two-dimensional surfaces with prescribed wave vector and Poynting vector distribu-

tions. A PCTIS consists of a periodic, subwavelength-patterned metallic cladding over a grounded dielectric substrate. The metallic cladding is analytically modeled as a tensor impedance sheet. An in-depth analysis of TIBCs and PCTISs is presented. First, the dispersion equation for an idealized TIBC is derived by expressing the field in terms of $TE$ and $TM$ waves. A similar approach is then used to find the dispersion equation of the PCTIS consisting of a tensor sheet impedance over a grounded dielectric substrate. In addition, a method for extracting the tensor sheet impedance of an arbitrary periodic, metallic cladding printed over a grounded dielectric substrate, is reported (tensor sheet impedance extraction method). It involves performing two normal-incidence scattering simulations using a full-wave electromagnetic solver, and does not require prior knowledge of the principal axes. By combining the tensor sheet impedance extraction method with the dispersion equation, the full dispersion characteristics of the PCTIS are analytically predicted in the homogenous limit. The results are verified through full-wave eigenmode simulations. Both the accuracy of the dispersion contours, and the computational cost of generating them are improved compared to methods used in the past [16, 17, 18, 11, 19, 20, 21, 22].

### 1.4.3 Chapter IV: Effective Surface Impedance of a PCTIS

In Chapter III, the dispersion equations for a TIBC and a PCTIS are derived from field analysis. In this chapter, a modified transverse resonance technique is employed to provide a more elegant method for deriving the dispersion equations of a TIBC and a PCTIS. The modified transverse resonance technique is an adaptation of the traditional transverse resonance technique [41]. Additionally, an explicit expression for the effective surface impedance of a PCTIS is derived using the modified transverse resonance technique, allowing PCTISs and TIBCs to be directly related. The effective surface impedance of the PCTIS is found to be dependent on the angle of propagation along the surface. In other words, it exhibits spatial dispersion that is a function of

the dielectric thickness. A discussion of the principal axes and the propagation of $TM$ and $TE$ waves is provided. The special case of electrically thin PCTISs is also analyzed and discussed. The results presented in this chapter provide a more elegant, and in some ways, a simpler view of TISs.

### 1.4.4   Chapter V: Transformation Electromagnetics Using PCTISs

In transformation electromagnetics, fields can be transformed from an initial distribution to a desired one through a change in material parameters ($\epsilon$ and $\mu$), which is dictated by a coordinate transformation. The traditional transformation electromagnetics method results in a transformation of all space. However, when transforming surfaces, one wishes to transform the surface impedance (rather than the material parameters) without transforming the free space above the surface. Therefore, there is need to find an alternate method that can be applied to surfaces. In this chapter, a method for designing transformation electromagnetics devices using TISs is presented. The methods allows anisotropic TIBCs and PCTISs to be designed that support tangential wave vector distributions and power flow directions specified by a coordinate transformation. Beam-shifting devices are designed using anisotropic TIBCs and PCTISs that allow a surface wave with a Gaussian profile to be shifted laterally at 10 GHz. The designs are verified with a commercial full-wave solver. Expressions for the group velocity, and direction of power flow along a TIBC and PCTIS are derived to aid in the design. The design limitations of transformation electromagnetics devices based on PCTISs are also discussed.

# CHAPTER II

# Sinusoidally-Modulated Scalar Impedance Surfaces

## 2.1 Chapter Introduction

As mentioned in the previous chapter, one of the goals of this thesis is to explore methods for determining the surface impedance profile needed to yield desired radiation patterns or wave guiding properties. Transformation electromagnetics is one such method, and will be discussed in Chapter V. In this section, sinusoidally modulating the surface impedance about some average reactance value is explored. Sinusoidal impedance variation along one direction is considered. With sinusoidal impedance modulation, nearly independent control of the phase and leakage constants along the surface can be achieved. The concept lends itself well to the design of leaky-wave antennas.

In recent years, there has been strong interest in high gain, low profile antennas that can be easily integrated into the surfaces of vehicles or other platforms [12, 14, 13, 15]. Planar leaky-wave antennas are excellent candidates for this purpose as they leak power from traveling waves propagating along the antenna surface. They are typically characterized by a phase and leakage constant along the antenna. Independent control over these two leaky-wave parameters is highly desired since it allows beam shaping [42].

Electromagnetic propagation along a sinusoidally-modulated reactance surface

(SMRS) was theoretically investigated by A. A. Oliner in 1959, as a way to increase the gain of surface-wave antennas [43]. More recently, SMRSs have been used to develop holographic antennas [19, 22, 24]. These antennas use the interference pattern between the field of a source and the desired radiated field to establish a sinusoidally varying surface impedance. Holographic antennas have shown great promise, but literature explaining their design has been limited. Furthermore, since many of these antennas are reflectors, they need to be illuminated by a separate radiator such as a horn antenna or waveguide aperture [11, 16, 17]. A direct feeding solution would be preferred in many applications. To date, slotted parallel-plate waveguides have been used extensively as leaky-wave antennas, since they are simple to fabricate and feed. However, they lack the independent control over phase and leakage constants [44, 45, 46] that SMRSs provide.

In this chapter, a step-by-step procedure is outlined for designing an SMRS that radiates at a desired angle. The concepts of an SMRS and a periodically slotted parallel-plate waveguide antenna are then combined to design a printed leaky-wave antenna that possesses a sinusoidally varying surface reactance [47, 48]. The antenna is directly fed, simple to fabricate, and allows for nearly independent control of phase and attenuation constants.

In Section 2.2, an overview of SMRSs and related theory is presented. The step-by-step design procedure for designing a SMRS with desired radiation characteristics is discussed in Section 2.3. A detailed example is also presented in this section. Section 2.4 shows how the designed SMRS can be used to realize a PCB-based leaky-wave antenna by printing metallic strips (separated by varying gaps) over a grounded dielectric substrate. The extraction method used to determine the appropriate gap sizes (between metallic strips) is outlined. Finally, Section 2.5 reports simulation and experimental results for the antenna.

## 2.2  SMRS Theory

A SMRS refers to a surface whose modal surface impedance is modulated sinusoidally. The modal surface impedance of a scalar impedance surface is defined as the ratio of the tangential electric field to the tangential magnetic field of the surface wave guided by the surface. By convention, the surface impedance is defined such that the Poynting vector points into the surface. Since the modal surface impedance ($\eta_{surf}$) is modulated sinusoidally, three parameters ($X$,$M$,$a$) can be used to characterize it (see Fig. 2.1). The average surface reactance is denoted by $X$, the modulation factor by $M$, and the periodicity of the sinusoid by $a$. In the cases considered, $\eta_{surf}$ is inductive such that it supports a TM surface wave [7]. The $x$-direction is assumed to be the direction of propagation along the SMRS. As a result, the surface impedance is given by the following expression,

$$\eta_{surf}(z) = j\eta_0 X' \left[ 1 + M \cos\left( \frac{2\pi x}{a} \right) \right] \tag{2.1}$$

where $X'$ is the average surface reactance normalized by the free-space wave impedance ($X' = X/\eta_0$).

Due to the periodic nature of the surface impedance, the fields above the surface can be expanded in terms of spatial harmonics, as shown in Fig. 2.2. The fundamental wave number tangential to the surface (Bloch wave number) is written as $k_{x0} = \kappa$ and the tangential wave number of the $n^{th}$ spatial harmonic as $k_{xn} = \kappa + 2\pi n/a$. The corresponding normal wave numbers ($k_{zn}$) can be found using the separation relation

$$k_{zn} = \sqrt{k_0^2 - \left( \kappa + \frac{2\pi n}{a} \right)^2}. \tag{2.2}$$

Employing the definition of the surface impedance and (2.1), a dispersion relation

can be written in continued fraction form [43]:

$$
1 - \frac{j}{X'}\sqrt{1 - \left[\frac{\kappa}{k_0}\right]^2} = \tag{2.3}
$$

$$
\cfrac{M^2/4}{1 - \frac{j}{X'}\sqrt{1 - \left[\frac{\kappa}{k_0} + \frac{2\pi(-1)}{k_0 a}\right]^2}} \Bigg|
$$

$$
- \cfrac{M^2/4}{1 - \frac{j}{X'}\sqrt{1 - \left[\frac{\kappa}{k_0} + \frac{2\pi(-2)}{k_0 a}\right]^2}} \Bigg| \dots
$$

$$
+ \cfrac{M^2/4}{1 - \frac{j}{X'}\sqrt{1 - \left[\frac{\kappa}{k_0} + \frac{2\pi(1)}{k_0 a}\right]^2}} \Bigg|
$$

$$
- \cfrac{M^2/4}{1 - \frac{j}{X'}\sqrt{1 - \left[\frac{\kappa}{k_0} + \frac{2\pi(2)}{k_0 a}\right]^2}} \Bigg| \dots,
$$

where $\kappa = \beta - j\alpha$.

Explicit expressions for the relative amplitudes of the magnetic-field spatial harmonics have also been derived in [43]. Equation (2.3) is a function of $\kappa$, the primary quantity of interest. Once $\kappa$ is known, all of the spatial harmonic wave numbers are known, and the relative amplitudes of the spatial harmonics can be calculated. Numerically solving (2.3) for $\kappa$, for the case $X' = 1.2$ and $M = 0.2$, yields the dash-dot curve shown in Fig 2.3. Notice the appearance of the stop band and the higher-order spatial harmonics (dashed curves). It should be noted that if (2.3) was solved for the case of zero modulation ($M = 0$), the equation would simplify to the dispersion equation for a scalar inductive surface,

$$
\kappa = k_0 \sqrt{1 + X'^2}, \tag{2.4}
$$

and the solution would be given by the solid line in Fig. 2.3. For small values of modulation ($M = 0.2$ in this case), the full solution for $\kappa$ obtained from (2.3)
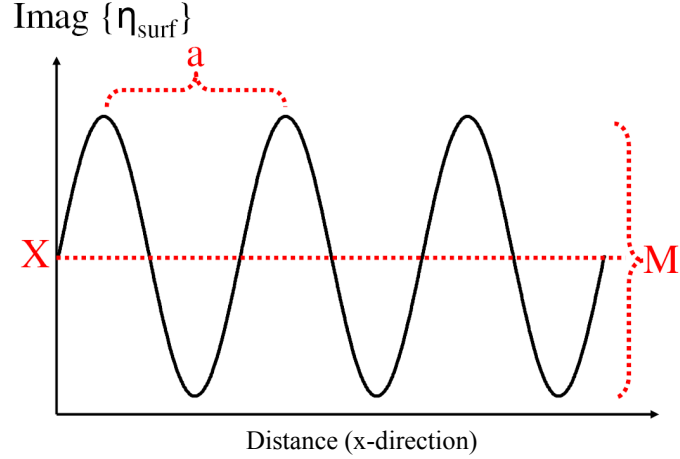
Figure 2.1: Sinusoidal form of the surface reactance.
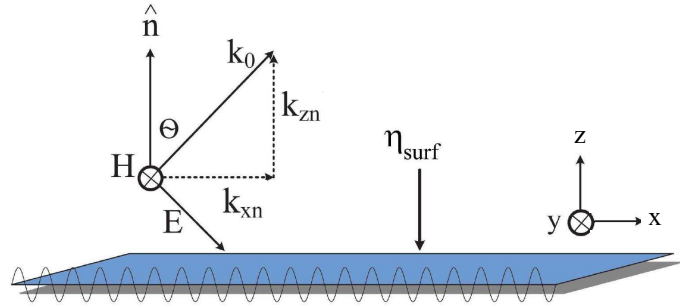


Figure 2.2: Spatial harmonic representation of fields due to SMRS and their corresponding wave numbers.

can be approximated by the solution of $\kappa$ obtained from (2.4). Since (2.4) assumes no modulation, it should be noted that this approximation is only valid away from the stop bands. Furthermore, it is evident that (2.4) is not a periodic function so it does not yield a periodic solution. Its solution only yields an approximation for the fundamental wave number along the surface and not for the higher-order spatial harmonics. However, since the higher-order spatial harmonics are simply shifted versions of the fundamental harmonic, it is still possible to approximate the higher-order spatial harmonics. These approximate solutions are exploited to construct a simplified design procedure.
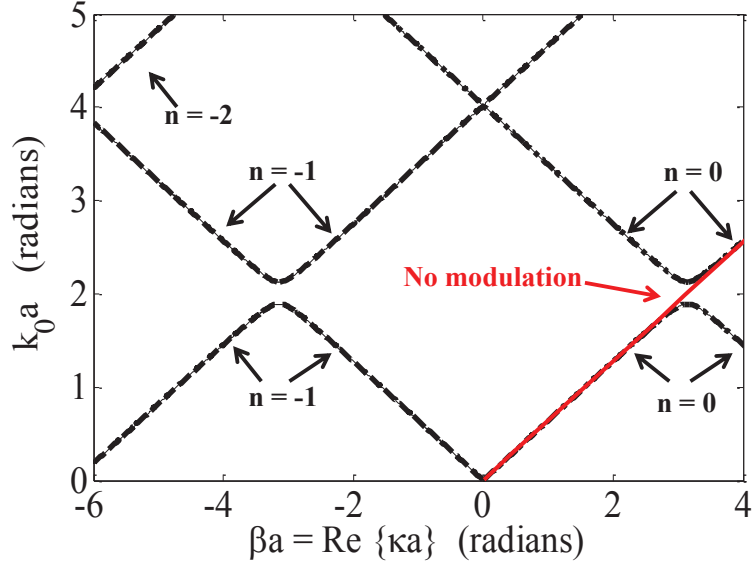
Figure 2.3: Solution of dispersion equation (2.3)for varying periodicity ($\kappa a$ vs. $k_0 a$ for $X = 1.2$, $M = 0.2$).

## 2.3 Surface Design

### 2.3.1 Simplified Design Procedure

This section outlines a step-by-step procedure for designing a SMRS that radiates at an arbitrary off-broadside angle. Specifically, a procedure is outlined that describes how the parameters $X, M$, and $a$ can be selected to generate directive radiation at a desired angle at a fixed frequency. The fundamental wave number along the surface can be decomposed into its real and imaginary parts, $\kappa = \beta - j\alpha$, where $\beta$ represents the propagation constant (or phase delay) and $\alpha$ represents the attenuation constant (or leakage rate) along the surface. For the un-modulated case ($M = 0$), the dispersion equation reduces to

$$\kappa_{approx} = k_0\sqrt{1 + X'^2} = \beta_{approx} \tag{2.5}$$

where $\beta_{approx}$ is close to the actual value of $\beta$ when the modulation of the surface is small. Since (2.5) only yields real solutions, $\kappa_{approx}$ will only yield a real-valued approximation for $\kappa$, implying that there is a phase delay along the surface ($\beta$ is

non-zero) but no attenuation due to radiation ($\alpha = 0$). In reality, $\kappa$ is complex, since leaky waves are excited. This will be reconciled later in the design process. The design process can be broken down into ten steps, which are outlined below.

1. Choose a design frequency ($f_0$) and its corresponding free space wave number, $k_0 = \frac{2\pi f_0}{c}$.

2. Choose the desired angle of radiation for the $n = -1$ spatial harmonic ($\theta_{n=-1}$) such that $90° > \theta_{n=-1} > -90°$.

3. Fix the value of either $X$ (average surface reactance) or $a$ (periodicity).

4. Solve for the remaining value using

$$\sin(\theta_{n=-1}) \approx \sqrt{1 + X'^2} - \frac{2\pi}{k_0 a}. \tag{2.6}$$

5. Solve for $\beta_{approx}$ using

$$\sin(\theta_{n=-1}) = \frac{\beta_{approx} - \frac{2\pi}{a}}{k_0}. \tag{2.7}$$

Equation (2.7) is derived from (2.5), which assumes that $M = 0$. In reality, M$\neq$0, but this assumption allows for an approximate $\beta$ (denoted by $\beta_{approx}$) to be computed, since low values of modulation only perturb $\beta$ slightly from the un-modulated case. The choice of $X$ and $a$ predominately determines $\beta$, and therefore the beam direction [42].

6. Choose a value for $M$, where $M \leq 1$. A non-zero modulation introduces an attenuation constant $\alpha$, which causes the wave number along the surface ($\kappa$) to become complex.

16

7. (Optional) Compute a more accurate value of $\kappa$, including the imaginary component, by using the full dispersion equation (2.3) if $M$ is large. The following perturbation equation can be used for small values of $M$ [43].

$$\kappa = \beta - j\alpha = k_0\sqrt{1 + X'^2}$$

$$-\frac{M^2}{4}\frac{k_0 X'^2}{\sqrt{1 + X'^2}}\left[\frac{1}{1 - \frac{j}{X'}\sqrt{1 - \left[\sqrt{1 + X'^2} - \frac{2\pi}{k_0 a}\right]}}\right.$$

$$\left. + \frac{1}{1 - \frac{j}{X'}\sqrt{1 - \left[\sqrt{1 + X'^2} + \frac{2\pi}{k_0 a}\right]}}\right].$$

$$(2.8)$$

The variables $X$ and $a$ control $\beta$ (beam pointing direction), while $M$ controls the attenuation constant (antenna beam width). Larger values of $M$ lead to larger values of $\alpha$ and therefore broader beam widths. A distribution of $\alpha$ can be used to control side lobe levels of the radiation pattern [42]. This can be achieved by varying $M$ along the antenna [49].

There are two advantages to dealing with low values of modulation. Firstly, the design procedure can be simplified significantly since the $M = 0$ approximation can be used away from stop bands. This removes the need for iteratively solving the dispersion equation (2.3). Secondly, the beam pointing direction can be designed by determining $X$ and $a$, and the beam width controlled by adjusting $M$ without significantly altering the beam pointing direction. This allows for nearly independent control of $\alpha$ and $\beta$. The definition of "low" values of modulation is discussed in the next subsection.

8. For the case where the accuracy of the beam direction is critical, compensate for the slight beam-shift that occurs due to the introduction of $M$ with a slight adjustment of $X$.
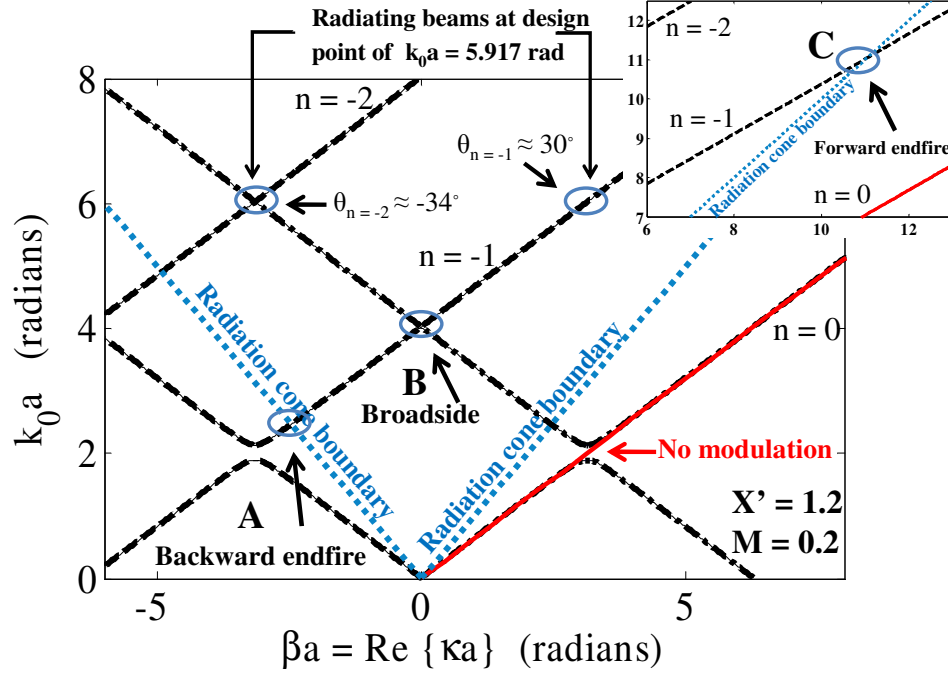
Figure 2.4: Brillouin diagram for a SMRS with design parameters: $X = 1.2$, $M = 0.2$.

9. Verify that the operating point $k_0a$ is not in the band-gap for the selected values of $X$, $M$, and $a$.

10. Finally, check if there are other radiating spatial harmonics besides the $n = -1$ harmonic. The $n^{th}$ harmonic radiates at an angle

$$\theta_n = \arcsin\left(\frac{\kappa a + 2\pi n}{k_0 a}\right) \tag{2.9}$$

when

$$(\kappa + \frac{2\pi n}{a})^2 < k_0. \tag{2.10}$$

In the next subsection, this ten step procedure is applied to design a surface that radiates at 30°.

18

### 2.3.2 Surface Design for $30°$ main beam at 10 GHz

A surface was designed that radiates at an angle of $\theta_{n=-1} = 30°$ from broadside at an operating frequency of 10 GHz. Using the design procedure described earlier, this surface was designed with the parameters $X' = 1.2$, $M = 0.2$, $a = 28.25$ mm. Fig. 2.4 shows the Brillouin diagram for the structure. The solid lines are light lines and define the radiation cone. The fundamental harmonic does not penetrate the radiation cone, and therefore is always bound to the surface. Point A represents the point where the $n = -1$ spatial harmonic enters the radiation cone (backward endfire). Point B is where it radiates in the broadside direction and point C (shown as an inset in Fig. 2.4) is where the $n = -1$ spatial harmonic exits the radiation cone, representing forward endfire. Therefore, points A and C mark the operating boundaries of the antenna. It should be noted that a directive beam cannot be designed exactly at broadside due to a dramatic increase in the attenuation constant at this point [50]. At the operating point of $k_0 a = 5.917$ radians, the $n = -1$ spatial harmonic radiates at $\theta_{n=-1} = 30°$, verifying the design procedure. A parasitic beam from the $n = -2$ spatial harmonic is also present at $\theta_{n=-2} = -34.18°$. These angles can easily be calculated using (2.9). Calculating the radiation angle for the other spatial harmonics shows that $\theta_{n=0,1,2..} \approx 90°$ and $\theta_{n=-3,-4,-5,...} \approx -90°$ corresponding to forward-bound and backward-bound waves, respectively. This is consistent with the Brillouin diagram of Fig. 2.4 with regard to which spatial harmonics appear in the radiation cone.

Fig. 2.5 and Fig. 2.6, generated using (2.4), show the dependance of $\alpha$ and $\beta$ on the modulation factor when $X' = 1.2$ is fixed and $k_0 a = 5.917$ radians is fixed. For low values of modulation, ($M < 0.6$ in this case), it is clear that $\alpha$ changes dramatically whereas $\beta$ is only slightly perturbed. This demonstrates nearly independent control of the parameters over a fairly wide range of modulation factor, $M$. The range over which $\beta$ remains fairly constant determines the values of $M$ that are considered to be
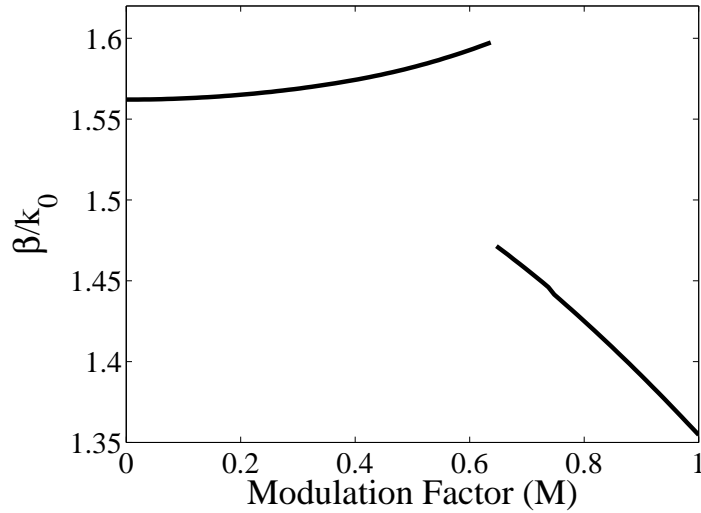
Figure 2.5: Theoretical variation in normalized propagation constant ($\beta/k_0$) along an ideal SMRS as a function of modulation (M) for $X' = 1.2$ and $k_0 a = 5.917$ radians.

"low". Fairly independent control of $\alpha$ and $\beta$ can be achieved for values of modulation up to $M \approx 0.6$. The sudden change in $\beta$ that occurs when $M \approx 0.6$ can also be seen in the band diagrams of Fig. 2.7 for four different modulation factors. For the designed surface with $M = 0.2$, the surface impedance ranges between $361.92j$ $\Omega$ and $542.88j$ $\Omega$. The impedance range corresponding to $M = 0.6$ is $180.96j$ $\Omega$ to $723.84j$ $\Omega$. Therefore, even "low" values of modulation correspond to fairly wide impedance ranges.

Now that a theoretical surface possessing the desired radiation characteristics has been designed, the question remains as to how this surface can be implemented and a leaky-wave antenna made from it. The next section addresses these two questions.
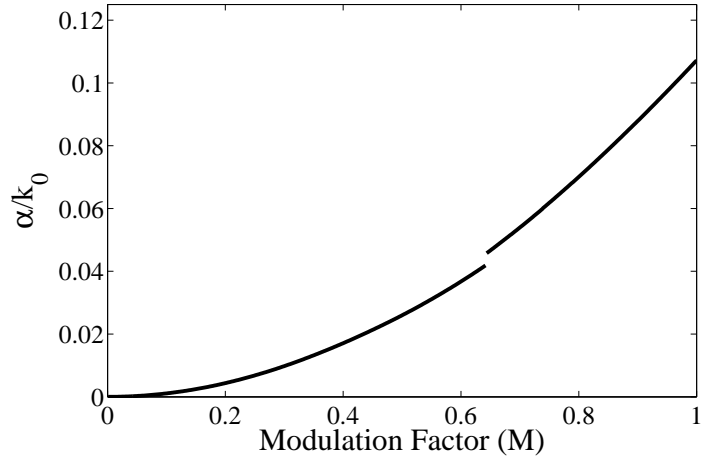
Figure 2.6: Theoretical variation in normalized attenuation constant $(\alpha/k_0)$ along an ideal SMRS as a function of modulation (M) for $X' = 1.2$ and $k_0 a = 5.917$ radians.
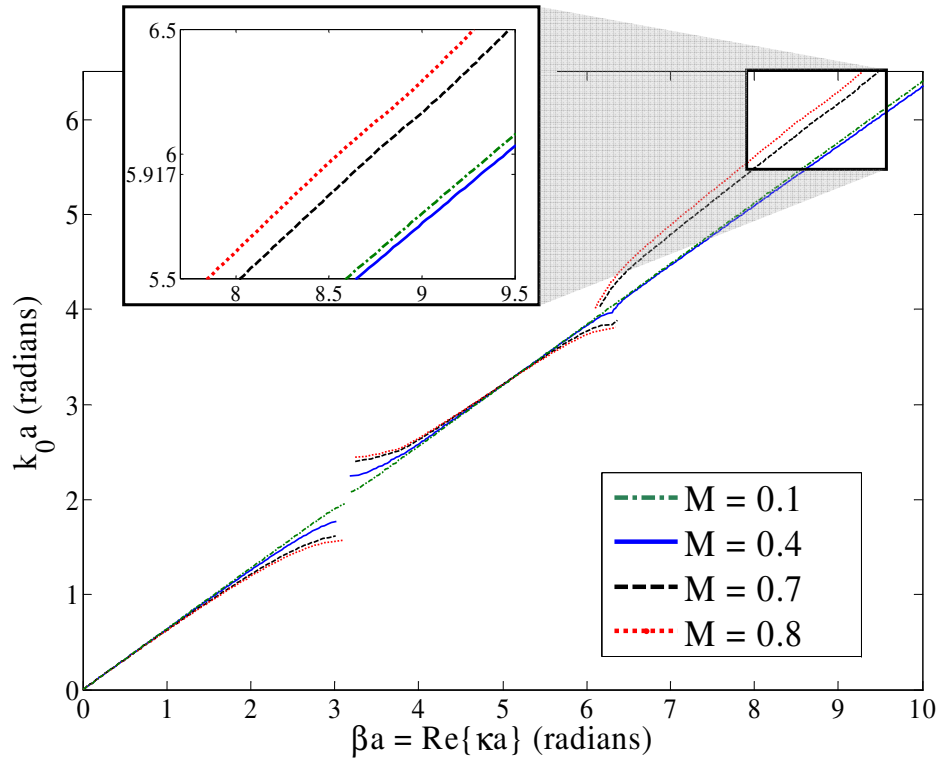


Figure 2.7: Band diagram showing the effect of increasing modulation while keeping $X' = 1.2$ fixed. At the fixed value of $k_0 a = 5.917$ radians, $\beta$ first increases and then decreases as modulation increases (inset).

## 2.4   Leaky-Wave Antenna Implementation

### 2.4.1   From a Theoretical Surface to a Realizable Antenna

Thus far, the discussion has been restricted to SMRSs and the design procedure for one that radiates the $n = -1$ spatial harmonic at a specified angle. In the previous section, a surface was designed to generate a beam at $\theta_{n=-1} = 30°$ at a frequency of 10 GHz. This section describes the implementation of the SMRS using a printed circuit board (PCB), in order to create a leaky-wave antenna that radiates at the same angle and frequency as the theoretical surface.

The SMRS was implemented as an array of copper strips over a grounded dielectric substrate, as shown in Fig. 2.8. One period ($a$) of the sinusoidal surface impedance is referred to as a unit cell. Each unit cell was implemented by sampling the surface impedance at ten discrete, equispaced points. The impedance at each point was realized as a gap between two copper strips over a grounded dielectric substrate. The strips were printed onto an ARLON AD-600 substrate ($\epsilon_r = 6.15$, $tan\delta \approx 0.0035$) with thickness $d = 2.54$ mm using a photolithographic etching procedure. The array of strips was designed to have periodically varying gaps to achieve the sinusoidal, modal surface impedance profile needed to realize the SMRS. The antenna, consisting of approximately eight unit cells, was 22.88 cm in length. The width of the surface was truncated (to 30 mm), such that a fairly uniform aperture illumination was still present, to form the leaky-wave antenna. The method used to map gap-sizes to desired surface impedances is described in detail in the next subsection.

### 2.4.2   Mapping Surface Impedance to Gap Size

The SMRS was implemented as a two-layer structure consisting of a periodically varying capacitive sheet (metallic strips) over a grounded dielectric substrate. A unit cell, corresponding to one period of the sinusoidal surface impedance, is shown in
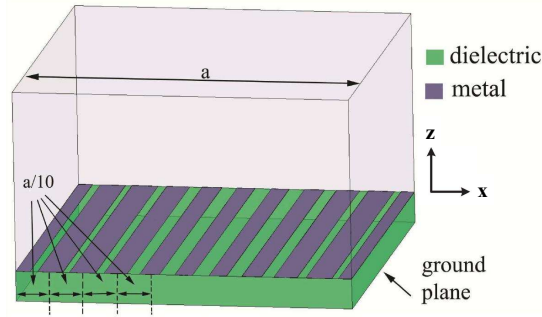
Figure 2.8: Unit cell representing one period of the SMRS.
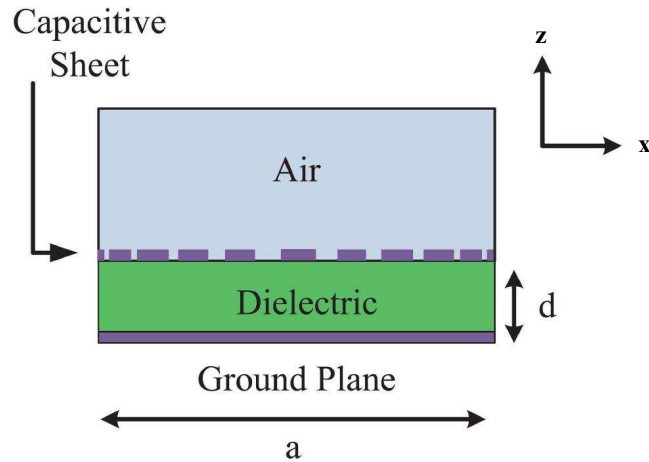


Figure 2.9: Side view of one unit cell representing one period of the SMRS.

Fig. 2.9. The capacitive sheet was designed such that the modal surface impedance looking into the two-layer structure has the same sinusoidal $\eta_{surf}$ as the theoretical SMRS designed in Section III. Each period ($a$) of the capacitive sheet was discretized into ten segments ($a/10$ in size). The capacitance over each segment was assumed to be constant, and was implemented as two copper strips separated by a gap. The capacitance of each segment is represented by a constant sheet impedance, $\eta_{sheet}$, shown in Fig. 2.10. This sheet impedance is defined as the ratio of tangential electric field to the surface current on the sheet. The sheet impedance in parallel with a short-circuited transmission line (representing the grounded dielectric substrate with thickness $d$) constitutes the transmission-line model of each segment. The

23
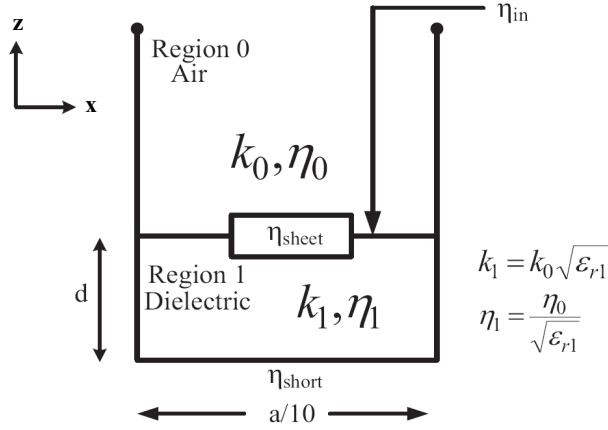
Figure 2.10: Normal-incidence transmission-line model for one discrete segment of the unit cell.

transmission-line model of each segment (Fig. 2.10) is first used to find $\eta_{sheet}$ from a normal-incidence scattering simulation. This sheet impedance is then used to find the TM modal surface impedance ($\eta_{surf}$) for that specific gap size. The value of the sheet impedance extracted at normal incidence ($\beta = 0$) is accurate even at oblique incidence (away from $\beta = 0$) if the transverse unit cell size is much smaller than the guided wavelength (see Appendix A). The overall goal here is to find the mapping between gap size and $\eta_{surf}$, so that a desired surface impedance profile can be realized by printing an array of metallic strips with varying gaps over a grounded dielectric substrate. Details of the procedure are outlined below.

1. The first step is to find the input impedance, $\eta_{in}$, of a single gap over the grounded dielectric substrate at normal incidence. This is accomplished by performing a simple normal-incidence scattering simulation, such as a driven-mode simulation in Ansys HFSS (see Fig. 2.11). The smallest gap allowed by one's fabrication facility marks a good starting point. Since $\eta_{in}$ is based on normal incidence, there is no phase delay along the surface and therefore no information can be gathered regarding the modal impedance of a surface wave

24

that can be guided. However, it is still possible to extract $\eta_{sheet}$ from $\eta_{in}$.

2. Using the circuit model shown in Fig. 2.10, $\eta_{sheet}$ can be extracted using the following expression:

$$\begin{aligned}
\frac{1}{\eta_{sheet}} &= \frac{1}{\eta_{in}} - \frac{1}{j\eta_1 \tan(k_1 d)} \\
&= \frac{1}{\eta_{in}} - \frac{1}{j\frac{\eta_0}{\sqrt{\epsilon_{r1}}} \tan(k_0\sqrt{\epsilon_{r1}}d)}.
\end{aligned} \tag{2.11}$$

Notice that the characteristic wave numbers and impedances in the transmission-line model are just those of free space in region 0 and the dielectric substrate with permittivity $\epsilon_{r1}$ in region 1, respectively.

3. Once $\eta_{sheet}$ is determined, it is possible to find $\eta_{surf}$ using a modified transmission-line model where the characteristic wave numbers and impedances are now represented by the TM wave numbers and impedances, as shown in Fig. 2.12. From this transmission-line model, it is apparent that $\eta_{surf}$ is given by the impedance looking down into the shunt combination of $\eta_{sheet}$ and a transmission-line section representing the grounded dielectric substrate with thickness $d$. The transverse resonance technique [42] can be applied to derive a dispersion equation for the TM surface waves guided by this multi-layer structure. Considering the transmission-line model shown in Fig. 2.12,

$$\frac{1}{\eta_{up}(x)} + \frac{1}{\eta_{down}(x)} = 0 \tag{2.12}$$

where $\eta_{up}$ and $\eta_{down}$ represent the impedances looking in opposite directions from any point on the transmission line. In this case, it is convenient to use the impedances observed above and below the capacitive sheet, as shown in Fig. 2.12. The dispersion relation from (2.12) can be written as

25

$$\frac{1}{\eta_{surf}} = \frac{1}{\eta_{sheet}} + \frac{1}{j\frac{\eta_0 k_{x1}}{k_0 \epsilon_{r1}}\tan(k_{x1}d)} \tag{2.13}$$

where

$$k_{x1} = \sqrt{k_0^2(\epsilon_{r1} - 1) + \left(\frac{\eta_{surf}k_0}{\eta_0}\right)^2}. \tag{2.14}$$

This equation can be solved numerically to find $\eta_{surf}$, from $\eta_{sheet}$ extracted for a given gap size.

4. Since the gap size is a free parameter, a design curve can be generated by parametrically sweeping the gap size in simulation and repeating the above procedure for the various gap sizes. A curve can be fitted to the data points to create a design curve which maps desired surface impedance values to the gap sizes needed to achieve them.

Fig. 2.13 represents the design curve used to map a desired surface impedance to its corresponding gap size for the antenna designed in this chapter. Methods used in the past for relating gap size to $\eta_{surf}$ included using an eigenmode simulator to parametrically sweep not only gap size, but also phase delay [19, 22]. For a given gap size, the phase delay across the unit cell was swept in order to find the phase delay that corresponds to the operating frequency. Once this phase delay was found (for a given gap size) the surface impedance could be computed using [19]

$$\eta_{surf} = j\eta_0\sqrt{\left(\frac{\phi}{k_0 l}\right)^2 - 1} \tag{2.15}$$

where $\phi$ represents the phase delay across the unit cell and $l = a/10$ represents the width of one-tenth of a unit cell, as shown in Fig. 2.11. This procedure had to be repeated for each gap size resulting in time consuming, two-dimensional sweeps over phase delay and gap size. Other methods include using custom MoM or FEM
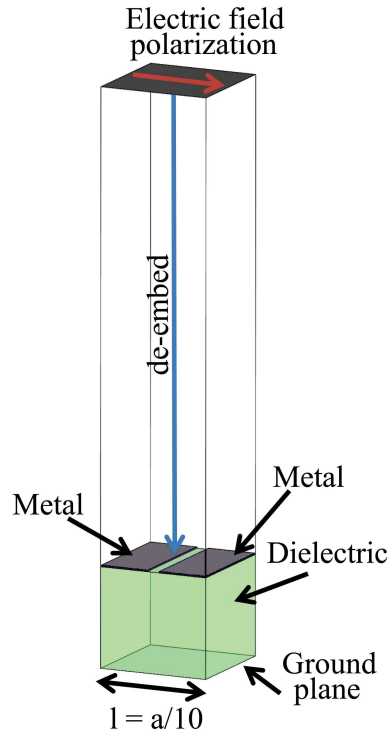
Figure 2.11: The normal-incidence scattering simulation performed on a single gap (segment) in order to find $\eta_{in}$ and the extracted sheet impedance ($\eta_{sheet}$).
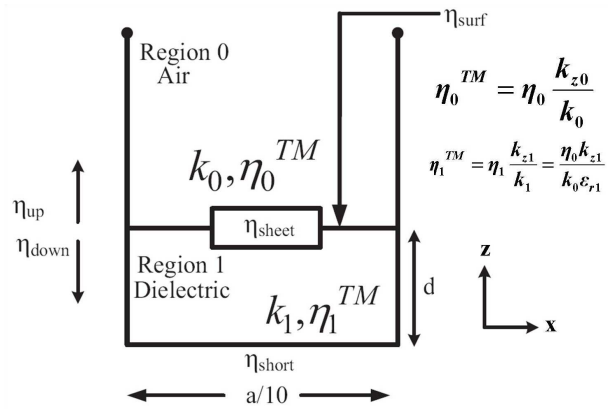


Figure 2.12: Modified transmission-line model for deriving the modal impedance.
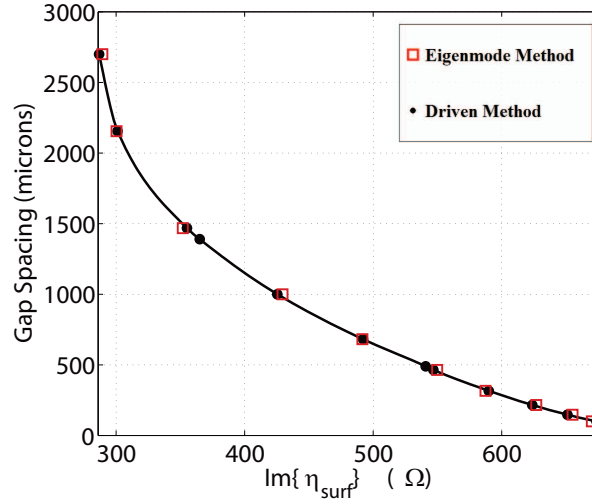
Figure 2.13: Gap spacing vs. surface reactance for the designed antenna. For the driven method, the sheet impedance is extracted from normal-incidence scattering simulations.

eigenmode solvers to numerically solve for phase delay across the periodic unit cell for a stipulated frequency. Equation (2.15) assumes that the segment, consisting of a multi-layer structure (capacitive sheet over a grounded dielectric substrate), can be approximated as a surface impedance. As will be shown in the next section, this approximation does not allow the attenuation constant to be predicted accurately if the net thickness of the multi-layer structure is not very small compared to a wavelength.

The main advantage of the method proposed here is that simulations can be done easily using a commercial solver. Furthermore, the commercial solver can be operated in scattering-solution mode, as opposed to eigen-solution mode. This eliminates the ambiguity of multiple modes corresponding to a single phase delay across the cell. In the method proposed here, only the gap size parameter needs to be swept, therefore significantly reducing the number of time consuming simulations that need to be performed. Fig. 2.13 compares the design curves generated using the eigenmode method [19] and the driven method proposed in this chapter. Close agreement between the

two methods is observed.

The driven method assumes that the only interaction between the ground plane and the capacitive sheet is via propagating waves through the dielectric. Therefore, the method is strictly valid when the dielectric thickness, $d$, is larger than the widest gap-size. This ensures that the evanescent wave interaction between the ground plane and the capacitive sheet is minimal [51].

## 2.5   Simulation and Experiment

A leaky-wave antenna, consisting of eight unit cells, was designed according to the procedure outlined in the previous section. Both ends of the antenna were tapered down to 50 $\Omega$ microstrip transmission lines and connected to edge-mount SMA connectors (see Fig. 2.14). This allowed return loss and insertion loss measurements to be performed. The tapers provided an impedance transition between the antenna and the 50$\Omega$ feed lines. During the radiation pattern measurements, the antenna was fed at one end while the other was terminated with a 50$\Omega$ SMA load to minimize reflections from the end of the antenna.

Fig. 2.15 shows good correspondence between the simulated (using Ansys HFSS) and measured radiation patterns along the E-plane, at the design frequency of 10 GHz. The angles of maximum radiation for the simulated and fabricated antennas were 30° and 29.25° respectively. The simulated HPBW along the E-plane was 8.51° in simulation and 7.57° in experiment. The simulated and measured gains were 17.04 dB and 18.4 dB respectively, and the measured cross-polarization remained below -22 dB over all angles, as seen in Fig. 2.16. The return loss and insertion loss from 9 GHz to 11 GHz is shown in Fig. 2.17. It should be noted that due to the complexity of the full-wave simulation, which involved a multiple wavelength long structure with many sub-wavelength features, the simulation did not reach a high level of convergence. This accounts for the discrepancy in gains between simulation and experiment.

Figure 2.14: Photograph of fabricated antenna with a 50Ω termination at one end.

The radiation patterns were also measured at discrete frequencies between 9 GHz and 11 GHz. Fig. 2.18 shows co-polarization and cross-polarization radiation patterns at 0.5 GHz increments between 9 GHz and 11 GHz, while Fig. 2.19 shows the simulated patterns versus the measured ones. The average beam squint was approximately 17.5°/GHz and the beam angle was ≈ 13° and ≈ 48° at 9 GHz and 11 GHz respectively. The directions and beam widths of the measured main beams were in close agreement with the simulated patterns.

At the design frequency, the beam angle was very close to the design angle of 30°, showing that the implemented SMRS was able to realize $\beta$ accurately. However, based on the beam width of the main beam in Fig. 2.15, the value of $\alpha$ for the implemented SMRS was significantly larger than that predicted by SMRS theory. Due to fabrication constraints on minimum gap size, the copper strips were printed on a 2.54 mm thick substrate in order to achieve the impedance values necessary to imple-
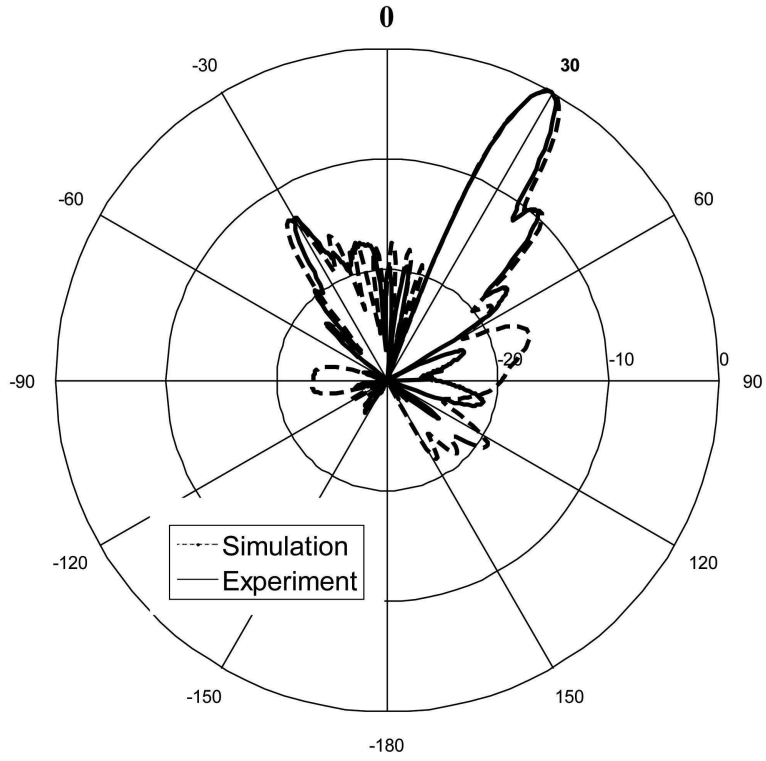
Figure 2.15: Simulated and measured co-polarization E-plane radiation patterns at $f_0 = 10$ GHz.
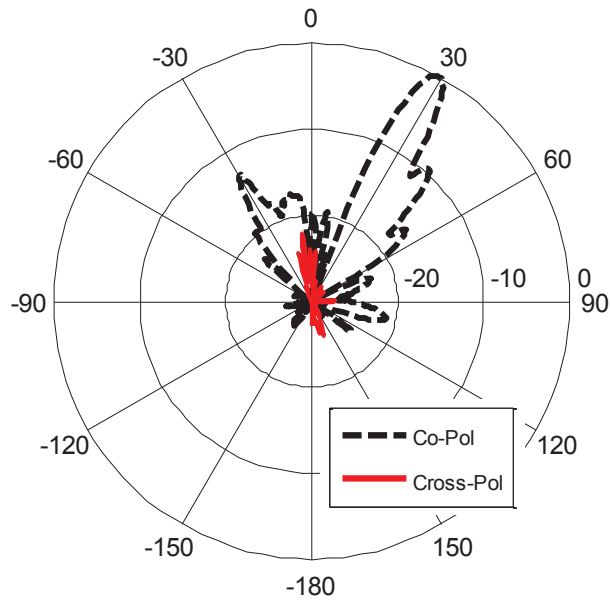


Figure 2.16: Measured co-polarization and cross-polarization E-plane radiation patterns at $f_0 = 10$ GHz.
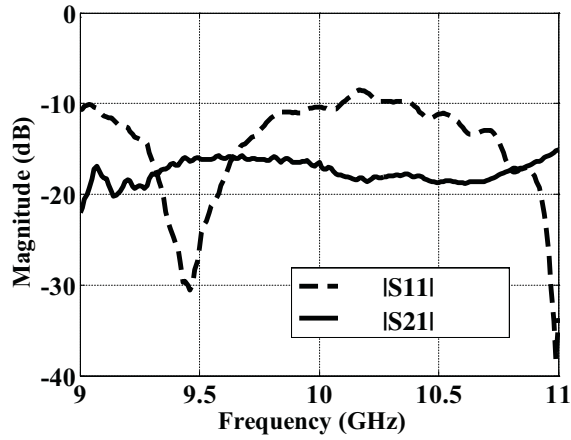
Figure 2.17:   Measured $|S11|$ and $|S21|$ from 9 GHz to 11 GHz.
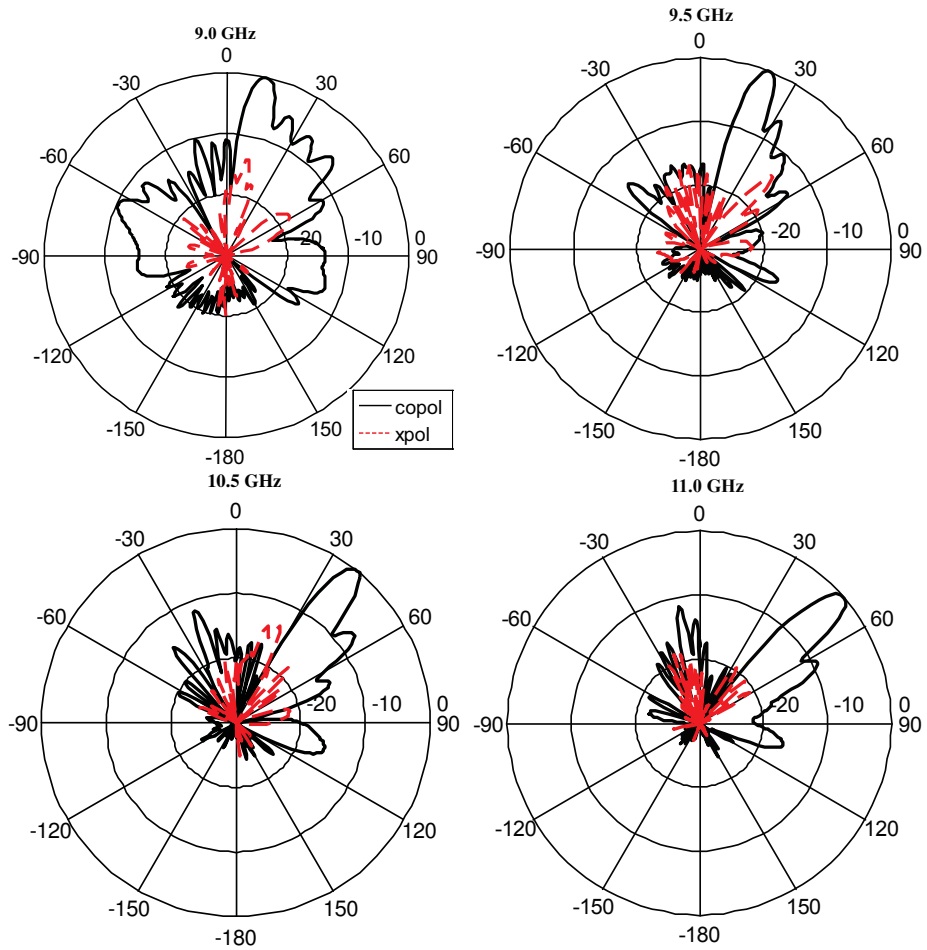


Figure 2.18: Measured co-polarization and cross-polarization E-plane radiation patterns for various frequencies between 9 GHz and 11 GHz.

32
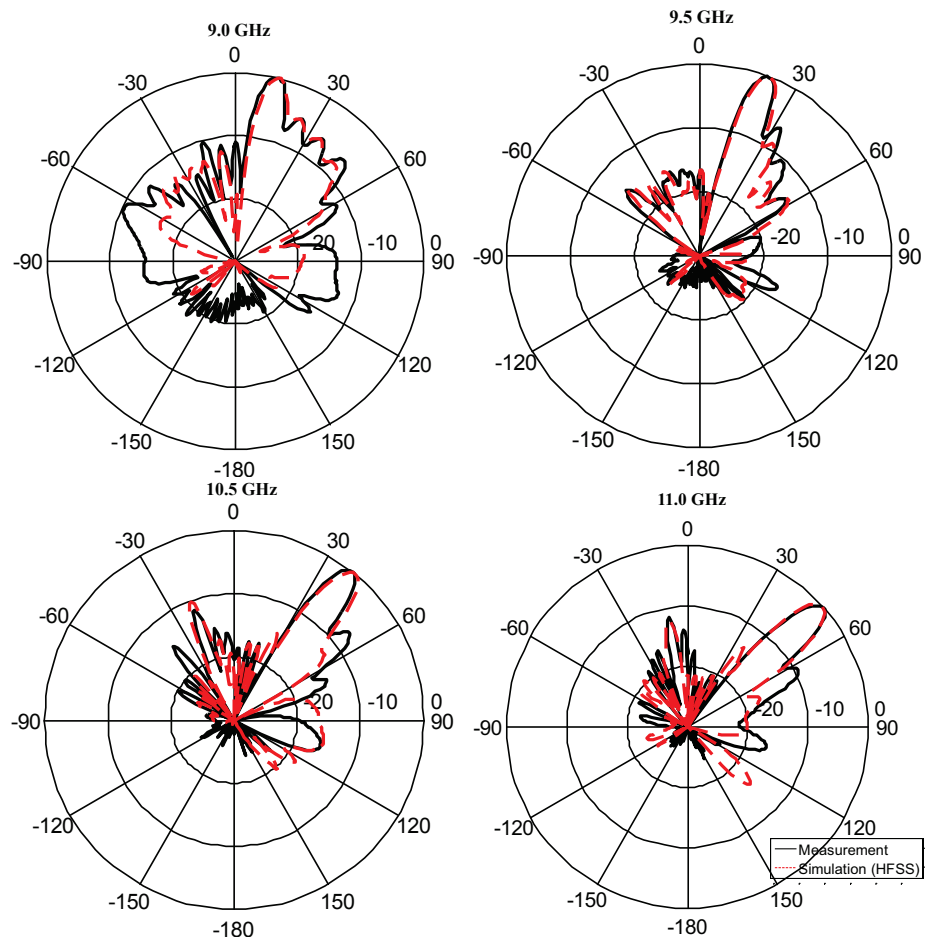
Figure 2.19: Measured and simulated co-polarization E-plane radiation patterns for frequencies between 9 GHz and 11 GHz.

ment the SMRS. This substrate, of approximately $\lambda_d/5$ thickness, was thick enough to introduce error into the sheet impedance approximation, used in Section 2.3, which assumes an infinitely thin sheet. This error was due to elements interacting through the dielectric, resulting from the considerable thickness of the dielectric substrate. Even though excellent correspondence between the theoretical and simulated values of $\beta$ is observed, disagreement between the theoretical and simulated value of $\alpha$ can be attributed to this source of error. A formulation that accounts for dielectric thickness, and therefore allows $\kappa = \beta - j\alpha$ to be found more accurately is given in Appendix B. Despite not being able to accurately predict $\alpha$ from SMRS theory, Table 2.1 presents full-wave simulation results that show that $\alpha$ can be controlled nearly independently of $\beta$ by varying the modulation factor, $M$ while keeping $X$ and $a$ fixed. Table 2.1 reports values of $\alpha$ and $\beta$ extracted from full-wave simulation for an antenna that is eight unit cells in length. Fig. 2.20 shows the simulated radiation patterns for the cases corresponding to Table 2.1. The beam direction is approximately the same for all the radiation patterns, but the beam width increases with increasing modulation. This confirms that the leakage rate can be controlled nearly independently of the phase constant.

Table 2.1: Extracted values of $\kappa = \beta - j\alpha$ for various values of modulation factor.

| $M$ | $\beta/k_0$ | $\alpha/k_0$ | $\kappa$ (rad/m) | $\theta_{n=-1}$ (degrees) |
|------|-----------|-----------|----------------|------------------------|
| 0.1  | 1.568949 | 0.021147 | 328.6 - 4.42906j | 29.3 |
| 0.2  | 1.568949 | 0.026375 | 328.6 - 5.52393j | 30.0 |
| 0.27 | 1.574297 | 0.066588 | 329.7 - 13.9461j | 30.1 |

## 2.6   Chapter Summary

In this chapter, a design procedure for a SMRS allowing directive radiation at an arbitrary off-broadside angle was outlined. The implementation of the SMRS using printed metallic strips over a grounded dielectric substrate was also presented. An extraction method for finding the sheet impedance of the metallic strips, using a
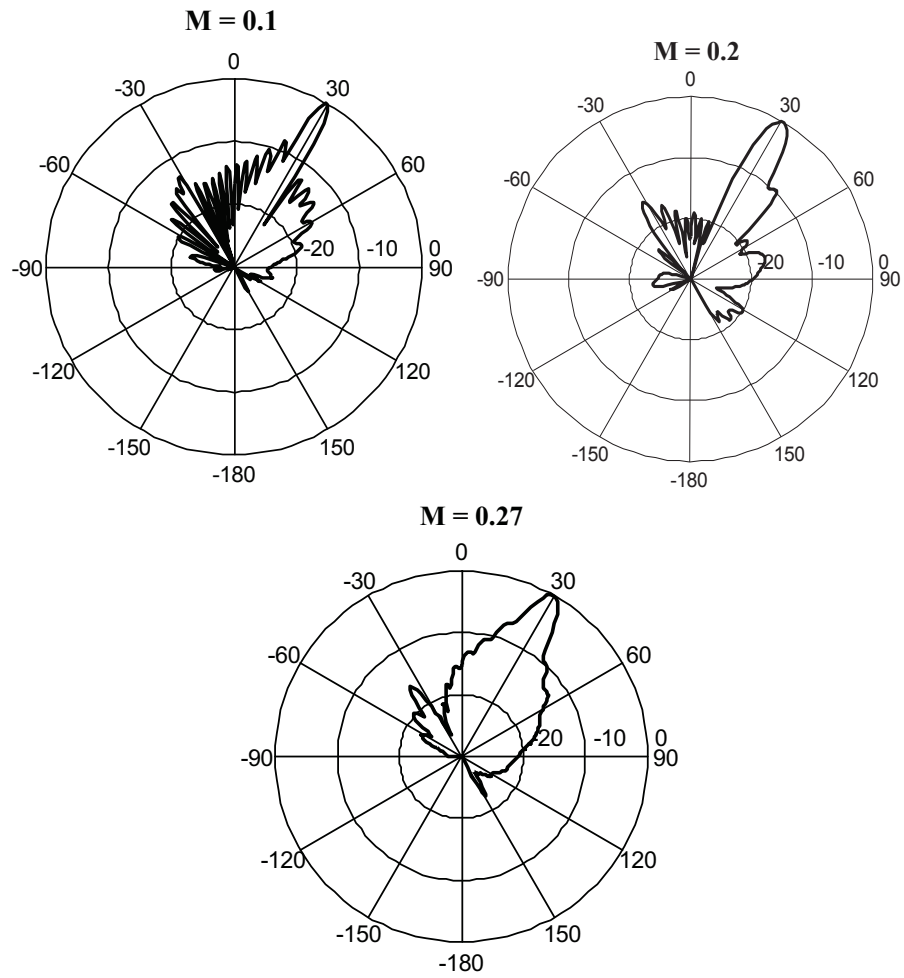
Figure 2.20: Simulated E-plane radiation patterns for eight unit-cell leaky-wave antennas with different modulation factors.

normal incidence scattering simulation, was presented. Using the extraction method, a design curve that maps the surface impedance to the gap size between metallic strips is generated. The design procedure for the surface allows for nearly independent control of the leakage rate and the phase constant along the SMRS. A printed leaky-wave antenna based on an SMRS was reported. The antenna is directly fed and simple to fabricate. At the design frequency of 10 GHz, the antenna radiates at approximately 30° from broadside, and exhibits an experimental gain of 18.4 dB. Good agreement between simulation and experiment was observed. SMRS theory accurately predicted the phase constant ($\beta$) along the antenna, but the simulated attenuation constant ($\alpha$) differed due to the antenna's electrical thickness. Despite the inaccuracy in the theoretical prediction of $\alpha$, it was shown through simulation that $\alpha$ can be controlled by varying the modulation factor without significantly perturbing $\beta$. This verifies the claim of nearly independent control of leakage rate and phase constant along the antenna.

Other forms of periodic surface impedance modulation (other than sinusoidal), may also be advantageous for controlling side lobes due other radiating harmonics (other than the $n = -1$ harmonic). Appendix B provides a formulation for finding $\alpha$ and $\beta$ for arbitrary periodic sheet impedances. Tapering the modulation factor along the extent of the surface (tailoring $\alpha$ along the surface) may also be useful for controlling side lobes.

In this chapter, the scalar surface impedance was varied in order to control the electromagnetic fields along the surface. Chapter III launches the study of tensor impedance surfaces (TISs), which continues for the remainder of this thesis. TISs allow enhanced control of the fields along a surface. Many of the concepts presented in this chapter, including the transverse resonance technique and the sheet impedance extraction method, are modified and applied to TISs in the upcoming chapters. In Chapter III, the dispersion equations for both idealized tensor impedance bound-

ary conditions (TIBCs) and printed-circuit tensor impedance surfaces (PCTISs) are derived, and their propagation characteristics predicted.

# CHAPTER III

# Analytical Modeling and Dispersion Analysis of Tensor Impedance Surfaces and Printed-Circuit Tensor Impedance Surfaces

## 3.1  Introduction

In the previous chapter, a scalar, sinusoidally modulated impedance surface was designed. A leaky-wave antenna based on this surface was then realized using printed-circuit board (PCB) technology. That is, the metallic cladding above a grounded dielectric substrate was patterned to achieve the desired surface impedance profile. Since propagation only along one direction was considered, it was possible to implement the scalar surface impedance using printed metallic strips above a grounded dielectric substrate. When considering propagation in two dimensions, square patches or other fully symmetric shapes could be used to implement scalar impedances (see Fig. 3.1). The propagation characteristics of electromagnetic waves on isotropic (scalar) impedance surfaces have been studied for some time, to control surface waves and leaky-wave radiation [7]. Extensive analytical modeling has been reported for open, printed structures such as the mushroom structure [52], which support isotropic forward-wave and backward-wave in-plane propagation. Tensor impedance surfaces (TISs) [10, 11] have also been explored for manipulating bound and leaky

38
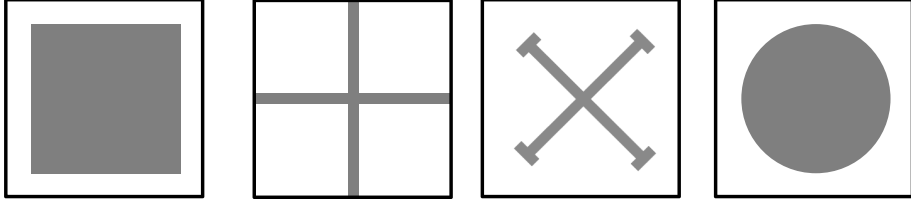
Figure 3.1: Examples of isotropic unit cells consisting of a printed metallic cladding over a grounded dielectric substrate (top view). Dark areas indicate metallization.
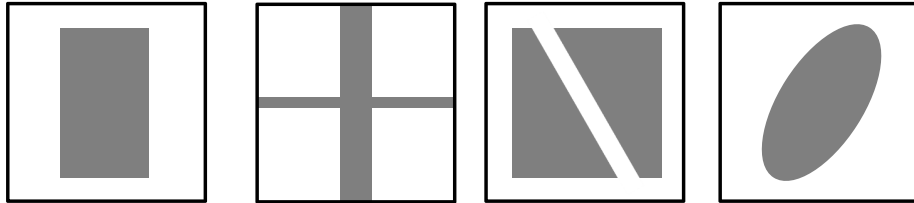


Figure 3.2: Examples of anisotropic unit cells consisting of a printed metallic cladding over a grounded dielectric substrate (top view). All four unit cells are anisotropic but the first two unit cells are represented with diagonal impedance tensor. The last two unit cells are represented with a full tensor. Dark areas indicate metallization.

waves. Great strides have been made in realizing practical printed devices such as holographic antennas and polarization controlling surfaces using the anisotropic properties of tensor surfaces [11, 16, 17, 18, 20, 22].

A single, idealized tensor impedance boundary condition (TIBC) [10, 11] has been used to design and analyze TISs. However, their implementation has been with printed-circuit structures, consisting of a patterned metallic cladding printed over a grounded dielectric substrate (see Fig. 3.2). In other words, it has been assumed that these structures can be approximated as single surfaces. Using this approximation can simplify the design process but may inadequately model radiation and guidance characteristics. A more accurate method for designing and analyzing these TISs is described in detail here in this chapter [53, 54, 55]. The method involves modeling printed-circuit structures as printed-circuit tensor impedance surfaces (PCTISs) con-

sisting of a tensor impedance sheet over a grounded dielectric substrate. The tensor impedance sheet models the patterned metallic cladding (see Fig. 3.2). It relates the tangential electric field to the current density on the sheet.

In this chapter, a method for analytically predicting the guidance characteristics of a PCTIS from two normal-incidence full-wave simulations is presented. The various parts of the procedure are outlined in separate sections of the chapter. In Section 3.2, the dispersion equation for an idealized TIBC [10] is derived by expressing the electromagnetic field in terms of the normal components of $TM$ and $TE$ waves. A similar approach is used in Section 3.3 to find the dispersion equation for an arbitrary tensor impedance sheet over a grounded dielectric substrate. This structure is used to model a PCTIS. In Section 3.4, the one-dimensional sheet impedance extraction method presented in Chapter II [47] is expanded to include two-dimensional tensor sheet impedances. Specifically, this section introduces a method for extracting the tensor sheet impedance of an arbitrary patterned metallic cladding. The method employs two simple normal-incidence simulations using a full-wave electromagnetic solver. Methods already exist for extracting the sheet impedance tensor if it is diagonal [56, 57]. In contrast, the method introduced here does not require a priori knowledge of the structure's principal axes, and therefore can be used to extract the full non-diagonal tensor sheet impedance. The method assumes there is no evanescent-wave interaction between the metallic cladding and ground plane. Therefore, they should be sufficiently displaced from each other. It is also assumed that the unit cell of the patterned metallic cladding is small compared to a guided wavelength, allowing it to be homogenized and modeled as an impedance sheet. By combining the dispersion equation for the PCTIS and the sheet impedance extraction method, the guidance characteristics of three example geometries are predicted analytically and verified using a full-wave eigenmode solver in Section 3.5.
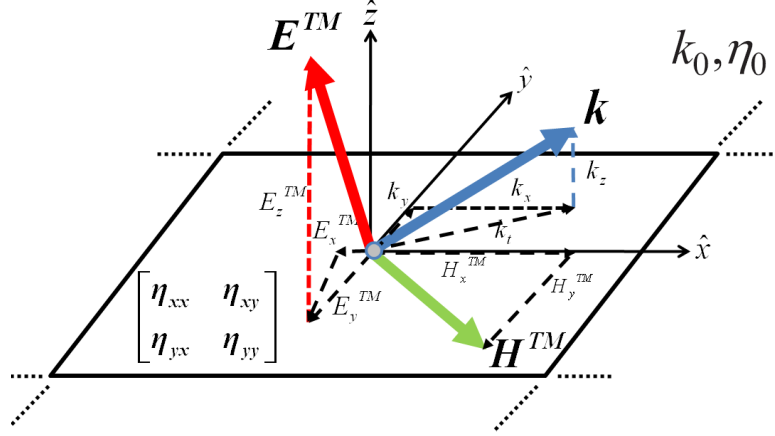
Figure 3.3: TIS supporting a $TM$ polarized wave.

## 3.2 Dispersion Equation for an Idealized Tensor Impedance Boundary Condition (TIBC)

TISs can be challenging to design since altering the printed geometry in even one direction generally affects all the tensor entries. Furthermore, depending on the reactance entries of the tensor surface impedance, the surface can support either $TM$, $TE$, or mixed modes. In this section, the dispersion equation for an idealized TIBC is derived using a procedure distinct from [10]. This procedure casts the dispersion equation in terms of the normal field components, $E_z^{TM}$ and $H_z^{TE}$. For a $TM$ wave, $H_z^{TM} = 0$ so it can be completely characterized by the $E_z^{TM}$ component (Fig. 3.3). Similarly, for a $TE$ wave, $E_z^{TE} = 0$, so it can be characterized by $H_z^{TE}$. The total electric and magnetic fields at the surface of the boundary are given by [58]

$$
\begin{aligned}
\overline{E}_{total} =& \overline{E}^{TM} + \overline{E}^{TE} \\
=& E_z^{TM} \hat{z} + \\
& \frac{1}{k_t^2} \left[ \nabla_s \frac{\partial E_z^{TM}}{\partial z} - j\omega\mu \nabla_s \times H_z^{TE} \hat{z} \right]
\end{aligned}
\tag{3.1}
$$

and

$$\overline{H}_{total} = \overline{H}^{TM} + \overline{H}^{TE}$$

$$= H_z^{TE}\hat{z} +$$

$$\frac{1}{k_t^2}\left[\nabla_s \frac{\partial H_z^{TE}}{\partial z} + j\omega\epsilon\nabla_s \times E_z^{TM}\hat{z}\right], \tag{3.2}$$

where $\nabla_s = -j(k_x\hat{x} + k_y\hat{y})$ and $k_t^2 = k_x^2 + k_y^2$. $\overline{E}_{total}$ and $\overline{H}_{total}$ are the sum of the $TM$ and $TE$ electric and magnetic fields at the surface $(z = 0)$.

The surface impedance tensor, $\overline{\overline{\eta}}_{surf}$, is defined as $\overline{E}_t = \overline{\overline{\eta}}_{surf}\hat{z} \times \overline{H}_t$ where $\overline{E}_t$ and $\overline{H}_t$ are the tangential components of $\overline{E}_{total}$ and $\overline{H}_{total}$, respectively. This boundary condition can equivalently be expressed as

$$\begin{pmatrix} E_x \\ E_y \end{pmatrix} = \begin{pmatrix} \eta_{xx} & \eta_{xy} \\ \eta_{yx} & \eta_{yy} \end{pmatrix} \begin{pmatrix} -H_y \\ H_x \end{pmatrix}. \tag{3.3}$$

The elements of $\overline{\overline{\eta}}_{surf}$ are the surface impedance entries of interest. Since the tangential electric and magnetic fields are composed of $TM$ and $TE$ waves,

$$\begin{pmatrix} \left(E_x^{TM} + E_x^{TE}\right) \\ \left(E_y^{TM} + E_y^{TE}\right) \end{pmatrix} = \\ \begin{pmatrix} \eta_{xx} & \eta_{xy} \\ \eta_{yx} & \eta_{yy} \end{pmatrix} \begin{pmatrix} -\left(H_y^{TM} + H_y^{TE}\right) \\ \left(H_x^{TM} + H_x^{TE}\right) \end{pmatrix}. \tag{3.4}$$

By expressing all field components in terms of $E_z^{TM}$ and $H_z^{TE}$, and noting that $\eta_0 = \sqrt{\frac{\mu}{\epsilon}}$, it is possible to re-cast the matrix equation as

$$\begin{pmatrix} b_{11} & b_{12} \\ b_{21} & b_{22} \end{pmatrix} \begin{pmatrix} E_z^{TM} \\ H_z^{TE} \end{pmatrix} = 0, \tag{3.5}$$

where

$$b_{11} = k_x k_z + \frac{k_x k \eta_{xx}}{\eta_0} + \frac{k_y k \eta_{xy}}{\eta_0}$$

$$b_{12} = k k_y \eta_0 + k_y k_z \eta_{xx} - k_x k_z \eta_{xy}$$

$$b_{21} = k_y k_z + \frac{k_x k \eta_{yx}}{\eta_0} + \frac{k_y k \eta_{yy}}{\eta_0}$$

$$b_{22} = -k k_x \eta_0 + k_y k_z \eta_{yx} - k_x k_z \eta_{yy}.$$

(3.6)

By setting the determinant of matrix $\bar{\bar{b}}$ in (3.5) to zero, the dispersion equation can be found

$$
\begin{aligned}
0 = {} & \left( 1 + \frac{\eta_{xx}}{\eta_0} \frac{\eta_{yy}}{\eta_0} - \frac{\eta_{xy}}{\eta_0} \frac{\eta_{yx}}{\eta_0} \right) k k_z \\
& + \left( \frac{\eta_{xy}}{\eta_0} + \frac{\eta_{yx}}{\eta_0} \right) k_x k_y + \left( \frac{\eta_{xx}}{\eta_0} + \frac{\eta_{yy}}{\eta_0} \right) k^2 \\
& - \left( \frac{\eta_{xx}}{\eta_0} \right) k_y^2 - \left( \frac{\eta_{yy}}{\eta_0} \right) k_x^2,
\end{aligned}
$$

(3.7)

which agrees with (19) in [10].

Since $\bar{\bar{b}}$ is a full matrix, the surface impedance can support mixed modes (both $TE$ and $TM$ modes). The principal axes (crystal axes) of the TIS are given by the eigenvectors that diagonalize the surface impedance tensor, $\bar{\bar{\eta}}_{surf}$. In the event that the direction of propagation, $k_t$, aligns with one of the principal axes, $\bar{\bar{b}}$ becomes diagonal matrix, $\bar{\bar{b'}}$, and the modes decouple. Therefore, equation (3.5) becomes

$$
\begin{pmatrix} b'_{11} & 0 \\ 0 & b'_{22} \end{pmatrix} \begin{pmatrix} E_z^{TM} \\ H_z^{TE} \end{pmatrix} = 0.
$$

(3.8)

Propagation along the principal axes results in purely $TM$ or $TE$ modes supported by the surface impedance. The determinant of $\bar{\bar{b'}}$ is zero when either $b'_{11} = 0$ or $b'_{22} = 0$, where $b'_{11}$ is associated only with $E_z^{TM}$ and $b'_{22}$ is associated only with $H_z^{TE}$. In the next section, the general method of separating the field into $TM$ and $TE$ waves is
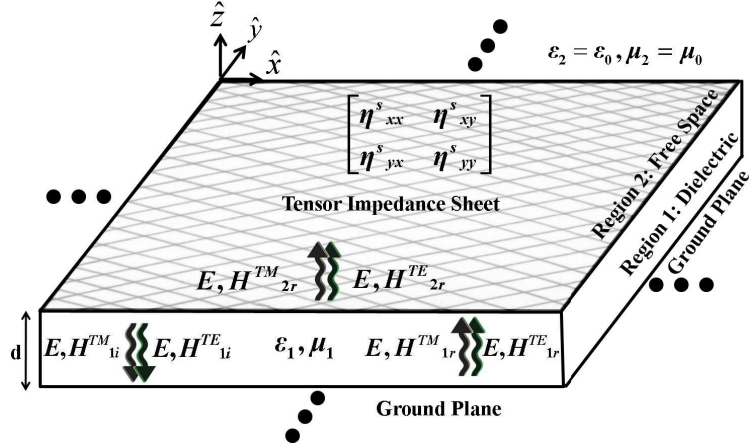
Figure 3.4: PCTIS consisting of a patterned metallic cladding over a grounded dielectric substrate. The cladding is modeled as a tensor impedance sheet.

applied to the analytical model for a PCTIS, in order to find its dispersion equation. The model consists of a tensor sheet impedance over a grounded dielectric substrate, where the sheet impedance models a periodically patterned metallic cladding.

## 3.3 Dispersion Equation for a Printed-Circuit Tensor Impedance Surface (PCTIS)

Equation (3.7) is the dispersion equation for an idealized TIBC. However, a PCTIS (see Fig. 3.4), consisting of a patterned metallic cladding over a grounded dielectric substrate, more accurately represents TISs described in literature [11, 16, 17, 18, 20, 22]. The metallic cladding is modeled as a tensor impedance sheet. The derivation of the dispersion equation for this two-layer surface is presented in this section. Using a similar procedure of separating the field into $TM$ and $TE$ waves, the incident and reflected electric and magnetic fields in the dielectric substrate (region 1) and free space (region 2) can be expressed as

44

$$E_{1i} = E_{z1i}^{TM} \hat{z} +$$
$$\frac{1}{k_t^2} \left[ (j\bar{k}_t) \frac{\partial E_{z1i}^{TM}}{\partial z} - \omega \mu_1 (\bar{k}_t) \times H_{z1i}^{TE} \hat{z} \right] \tag{3.9}$$

$$E_{nr} = E_{znr}^{TM} \hat{z} +$$
$$\frac{1}{k_t^2} \left[ (-j\bar{k}_t) \frac{\partial E_{znr}^{TM}}{\partial z} - \omega \mu_n (\bar{k}_t) \times H_{znr}^{TE} \hat{z} \right] \tag{3.10}$$

and

$$H_{1i} = H_{z1i}^{TE} \hat{z} +$$
$$\frac{1}{k_t^2} \left[ (j\bar{k}_t) \frac{\partial H_{z1i}^{TE}}{\partial z} + \omega \epsilon_1 (\bar{k}_t) \times E_{z1i}^{TM} \hat{z} \right], \tag{3.11}$$

$$H_{nr} = H_{znr}^{TE} \hat{z} +$$
$$\frac{1}{k_t^2} \left[ (-j\bar{k}_t) \frac{\partial H_{znr}^{TE}}{\partial z} + \omega \epsilon_n (\bar{k}_t) \times E_{znr}^{TM} \hat{z} \right], \tag{3.12}$$

where $n = 1$ for the reflected wave in region 1, and $n = 2$ for the reflected wave in region 2. No incident wave is present in region 2. Enforcing a vanishing tangential electric field at the ground plane ($z = -d$), yields two equations: one for each of the $x$ and $y$ components of the electric field,

$$0 = (k_{x1} k_{z1}) E_{z1_i}^{TM} e^{-jk_{z1}d} - (k_x k_{z1}) E_{z1_r}^{TM} e^{jk_{z1}d}$$
$$- \left( \frac{k_1^2 k_y}{\omega \epsilon_1} \right) H_{z1_i}^{TE} e^{-jk_{z1}d} - \left( \frac{k_1^2 k_y}{\omega \epsilon_1} \right) H_{z1_r}^{TE} e^{jk_{z1}d} \tag{3.13}$$

and

$$0 = (k_y k_{z1}) E_{z1_i}^{TM} e^{-jk_{z1}d} - (k_y k_{z1}) E_{z1_r}^{TM} e^{jk_{z1}d}$$
$$+ \left( \frac{k_1^2 k_x}{\omega \epsilon_1} \right) H_{z1_i}^{TE} e^{-jk_{z1}d} + \left( \frac{k_1^2 k_x}{\omega \epsilon_1} \right) H_{z1_r}^{TE} e^{jk_{z1}d}. \tag{3.14}$$

Enforcing the continuity of the tangential electric field at $z = 0$, $(\overline{E}_2 - \overline{E}_1) \times \hat{z} = 0$ yields another two equations:

$$(3.15)$$

$$\left(\frac{k_x k_{z2}}{k_2^2 - k_{z2}^2}\right) E_{z2_r}^{TM} + \frac{k_2^2}{\omega \epsilon_2} \left(\frac{k_y k_{z2}}{k_2^2 - k_{z1}^2}\right) H_{z2_r}^{TE}$$
$$= \left(\frac{k_x k_{z1}}{k_1^2 - k_{z1}^2}\right) E_{z1_i}^{TM} - \left(\frac{k_x k_{z1}}{k_1^2 - k_{z1}^2}\right) E_{z1_r}^{TM} \qquad (3.16)$$
$$- \frac{k_1^2}{\omega \epsilon_1} \left(\frac{k_y}{k_1^2 - k_{z1}^2}\right) H_{z1_i}^{TE} - \frac{k_1^2}{\omega \epsilon_1} \left(\frac{k_y}{k_1^2 - k_{z1}^2}\right) H_{z1_r}^{TE}$$

for the $x$-component of $\overline{E}_t$ and

$$\left(\frac{k_{y2} k_{z2}}{k_2^2 - k_{z2}^2}\right) E_{z2_r}^{TM} + \frac{k_2^2}{\omega \epsilon_2} \left(\frac{k_{x2} k_{z2}}{k_2^2 - k_{z1}^2}\right) H_{z2_r}^{TE}$$
$$= \left(\frac{-k_y k_{z1}}{k_1^2 - k_{z1}^2}\right) E_{z1_i}^{TM} + \left(\frac{k_y k_{z1}}{k_1^2 - k_{z1}^2}\right) E_{z1_r}^{TM} \qquad (3.17)$$
$$+ \frac{k_1^2}{\omega \epsilon_1} \left(\frac{k_x k_{z1}}{k_1^2 - k_{z1}^2}\right) H_{z1_i}^{TE} + \frac{k_1^2}{\omega \epsilon_1} \left(\frac{k_x k_{z1}}{k_1^2 - k_{z1}^2}\right) H_{z1_r}^{TE}$$

for the $y$-component. The tensor sheet impedance, defined by

$$\overline{\overline{\eta}}_{sheet} = \begin{pmatrix} \eta_{xx}^s & \eta_{xy}^s \\ \eta_{yx}^s & \eta_{yy}^s \end{pmatrix}, \qquad (3.18)$$

relates the tangential electric field at the sheet to the current density across the sheet as

$$\begin{pmatrix} E_x \\ E_y \end{pmatrix} = \begin{pmatrix} \eta_{xx}^s & \eta_{xy}^s \\ \eta_{yx}^s & \eta_{yy}^s \end{pmatrix} \begin{pmatrix} J_x \\ J_y \end{pmatrix} \qquad (3.19)$$

at $z = 0$. This equation can be recast as

$$\begin{pmatrix} J_x \\ J_y \end{pmatrix} = \begin{pmatrix} Y_{xx}^s & Y_{xy}^s \\ Y_{yx}^s & Y_{yy}^s \end{pmatrix} \begin{pmatrix} E_x \\ E_y \end{pmatrix} \qquad (3.20)$$

where

$$\begin{pmatrix} Y_{xx}^s & Y_{xy}^s \\ Y_{yx}^s & Y_{yy}^s \end{pmatrix} = \overline{\overline{Y}}_{sheet} = \overline{\overline{\eta}}_{sheet}^{-1}. \tag{3.21}$$

Substituting the tangential electric field in region 2 at $z = 0$, into (3.20), it is clear that

$$J_x = Y_{xx}^s \left( E_{x2_r}^{TM} + E_{x2_r}^{TE} \right) + Y_{xy}^s \left( E_{y2_i}^{TM} + E_{y2_i}^{TE} \right), \tag{3.22}$$

and

$$J_y = Y_{yx}^s \left( E_{x2_r}^{TM} + E_{x2_r}^{TE} \right) + Y_{yy}^s \left( E_{y2_i}^{TM} + E_{y2_i}^{TE} \right). \tag{3.23}$$

Enforcing Ampere's Law, $\hat{z} \times (\overline{H}_2 - \overline{H}_1) = \overline{J}$, at the impedance sheet ($z = 0$) and substituting in (3.22) and (3.23) results in the last two equations:

$$\begin{aligned} Y_{yx}^s &\left[ \frac{k_2}{\eta_2} \left( \frac{k_y}{k_t^2} \right) H_{z2_r}^{TE} + \frac{k_x k_{z2}}{k_t^2} E_{z2_r}^{TM} \right] \\ -Y_{yy}^s &\left[ \frac{k_2}{\eta_2} \left( \frac{k_x}{k_t^2} \right) H_{z2_r}^{TE} - \frac{k_x k_{z2}}{k_t^2} E_{z2_r}^{TM} \right] \\ =& \frac{k_1}{\eta_1} \left( \frac{k_y}{k_t^2} \right) E_{z1_i}^{TM} + \frac{k_1}{\eta_1} \left( \frac{k_y}{k_t^2} \right) E_{z1_r}^{TM} \\ &+ \left( \frac{k_x k_{z1}}{k_t^2} \right) H_{z1_i}^{TE} - \left( \frac{k_x k_{z1}}{k_t^2} \right) H_{z1_r}^{TE} \\ &- \frac{k_2}{\eta_2} \left( \frac{k_y}{k_t^2} \right) E_{z2_r}^{TM} + \left( \frac{k_x k_{z2}}{k_t^2} \right) H_{z2_r}^{TE} \end{aligned} \tag{3.24}$$

and

$$\begin{aligned} Y_{xx}^s &\left[ \frac{k_2}{\eta_2} \left( \frac{k_y}{k_t^2} \right) H_{z2_r}^{TE} + \frac{k_x k_{z2}}{k_t^2} E_{z2_r}^{TM} \right] \\ -Y_{xy}^s &\left[ \frac{k_2}{\eta_2} \left( \frac{k_x}{k_t^2} \right) H_{z2_r}^{TE} - \frac{k_x k_{z2}}{k_t^2} E_{z2_r}^{TM} \right] \\ =& \frac{k_1}{\eta_1} \left( \frac{-k_x}{k_t^2} \right) E_{z1_i}^{TM} + \frac{k_1}{\eta_1} \left( \frac{-k_x}{k_t^2} \right) E_{z1_r}^{TM} \\ &- \left( \frac{k_y k_{z1}}{k_t^2} \right) H_{z1_i}^{TE} + \left( \frac{k_y k_{z1}}{k_t^2} \right) H_{z1_r}^{TE} \\ &- \frac{k_2}{\eta_2} \left( \frac{k_x}{k_t^2} \right) E_{z2_r}^{TM} - \left( \frac{k_y k_{z2}}{k_t^2} \right) H_{z2_r}^{TE}. \end{aligned} \tag{3.25}$$

47

That is, one equation for each tangential component of $\overline{H}$.

The six equations ((3.13)-(3.17),(3.24), and (3.25)) given by the boundary conditions on the electric and magnetic fields can be cast as a matrix equation. This equation can be further reduced to the following,

$$0 = \begin{pmatrix} a_{11} & a_{12} \\ a_{21} & a_{22} \end{pmatrix} \begin{pmatrix} E_{z1_i}^{TM} \\ H_{z1_i}^{TE} \end{pmatrix}. \tag{3.26}$$

The elements of $\overline{\overline{a}}$ can be used to find the ratio of $TM$ to $TE$ components in the mixed modes. Setting the determinant of $\overline{\overline{a}}$ equal to zero yields the dispersion equation for the two-layer tensor impedance surface:

$$\epsilon_1 k_2^2 k_{z1} \omega \cos{(k_{z1}d)}$$

$$\left[ jk_{z1}\mu_1 \sin{(k_{z1}d)} \left( k_2^2(k_x^2 + k_y^2) + k_{z2}\mu_2\omega \left( k_x^2 Y_{xx}^s + k_x k_y (Y_{xy}^s + Y_{yx}^s) + k_y^2 Y_{yy}^s \right) \right) \right.$$

$$\left. + k_1^2 k_{z2}\mu_2(k_x^2 + k_y^2) \cos{(k_{z1}d)} \right]$$

$$+ jk_1^2 \sin{(k_{z1}d)}\epsilon_2 k_{z2}\omega$$

$$\left[ jk_{z1}\mu_1 \sin{(k_{z1}d)} \left( k_2^2(k_x^2 + k_y^2) + k_{z2}\mu_2\omega \left( k_x^2 Y_{xx}^s + k_x k_y (Y_{xy}^s + Y_{yx}^s) + k_y^2 Y_{yy}^s \right) \right) \right.$$

$$\left. + k_1^2 k_{z2}\mu_2(k_x^2 + k_y^2) \cos{(k_{z1}d)} \right]$$

$$+ jk_1^2 \sin{(k_{z1}d)}k_2^2$$

$$\left[ k_{z2}\mu_2 \left( k_1^2 \cos{(k_{z1}d)} \left( k_x^2 Y_{yy}^s - k_x k_y (Y_{xy}^s + Y_{yx}^s) + k_y^2 Y_{xx}^s \right) \right. \right.$$

$$\left. - jk_{z1}\mu_1\omega(k_x^2 + k_y^2) \sin{(k_{z1}d)}(Y_{xy}^s Y_{yx}^s - Y_{xx}^s Y_{yy}^s) \right)$$

$$\left. + jk_2^2 k_{z1}\mu_1 \sin{(k_{z1}d)} \left( k_x^2 Y_{yy}^s - k_x k_y \left( Y_{xy}^s + Y_{yx}^s \right) + k_y^2 Y_{xx}^s \right) \right] = 0,$$

$$\tag{3.27}$$

The derived dispersion equation can predict the propagation characteristics of a tensor impedance sheet over a grounded dielectric substrate, provided the tensor sheet admittance entries ($Y_{xx}^s$, $Y_{xy}^s$, $Y_{yx}^s$, and $Y_{yy}^s$) are known. The sheet impedance bound-

ary condition, given by (3.19), can be used to model the patterned metallic cladding when the unit cell size is much smaller than a guided wavelength.

A method for finding the tensor sheet impedance/admittance for a patterned metallic cladding is outlined in the next section. The procedure involves performing two normal-incidence scattering simulations using a full-wave electromagnetic solver.

## 3.4 Tensor Sheet Extraction Method

In this section, a method for finding the tensor sheet impedance that models the periodically patterned metallic cladding of a PCTIS is outlined. It is an extension of the one-dimensional sheet impedance extraction method presented in Chapter II [47]. Since the structure is periodic, a single unit cell with periodic boundary conditions is considered. Two normal incidence simulations are performed on the unit cell: one with the incident electric field polarized in the $x$-direction (illumination $I$), and another with a $y$-directed electric field (illumination $II$). For illumination $I$, the incident and scattered electric and magnetic fields in regions 1 and 2, can be expressed in terms of unknown field amplitudes $(A_I, B_I, C_I, D_I, E_I, F_I, G_I)$,

$$\overline{E}^i_{1I} = (B_I\hat{x} + C_I\hat{y})\, e^{jk_1z} \tag{3.28}$$

$$\overline{H}^i_{1I} = \frac{1}{\eta_1}\,(C_I\hat{x} - B_I\hat{y})\, e^{jk_1z} \tag{3.29}$$

$$\overline{E}^r_{1I} = (D_I\hat{x} + E_I\hat{y})\, e^{-jk_1z} \tag{3.30}$$

$$\overline{H}^r_{1I} = \frac{1}{\eta_1}\,(-E_I\hat{x} + D_I\hat{y})\, e^{-jk_1z} \tag{3.31}$$

$$\overline{E}^i_{2I} = A_I\hat{x}e^{jk_2z} \tag{3.32}$$

$$\overline{H}^i_{2I} = -\frac{1}{\eta_2}\,(A_I\hat{y})\, e^{jk_2z} \tag{3.33}$$

$$\overline{E}^r_{2I} = (F_I\hat{x} + G_I\hat{y})\, e^{-jk_2z} \tag{3.34}$$

$$\overline{H}^r_{2I} = \frac{1}{\eta_2}\,(-G_I\hat{x} + F_I\hat{y})\, e^{-jk_2z}, \tag{3.35}$$

where the subscript $I$ indicates the fields associated with illumination $I$. It should be noted that even though the incident field, $\overline{E}^i_{2I}$, is only $x$-polarized, the reflected field in region 2 as well as the fields in region 1 have mixed $x$- and $y$-polarizations due to the tensor nature of the sheet.

Applying the boundary condition, $E_t = 0$, at the ground plane $(z = d)$ yields

$$B_I e^{-jk_1 d} + D_I e^{jk_1 d} = 0 \tag{3.36}$$

for the $x$-component and

$$C_I e^{-jk_1 d} + E_I e^{jk_1 d} = 0 \tag{3.37}$$

for the $y$-component of the total electric field. Enforcing continuity of the tangential components of the electric field at the surface $(z = 0)$, yields

$$B_I + D_I = A_I + F_I \tag{3.38}$$

for the $x$-component and

$$C_I + D_I = G_I \tag{3.39}$$

for the $y$-component. Ampere's Law at the impedance sheet $(z = 0)$,

$$H_{2x} - H_{1x} = J_y \tag{3.40}$$

$$H_{1y} - H_{2y} = J_x \tag{3.41}$$

yields

$$\begin{aligned}
\frac{k_2}{\omega \mu_2} \left( A_I - F_I \right) + \frac{k_1}{\omega \mu_1} \left( D_I - B_I \right) \\
= Y^s_{xx} \left( A_I + F_I \right) + Y^s_{xy} \left( G_I \right)
\end{aligned} \tag{3.42}$$

and

$$\frac{k_1}{\omega\mu_1}(E_I - C_I) + \frac{k_2}{\omega\mu_2}(-G_I)$$
$$= Y_{yx}^s (A_I + F_I) + Y_{yy}^s (G_I). \tag{3.43}$$

Dividing equations (3.36-3.39), (3.42), and (3.43) by $A_I$ and expressing them as a matrix system gives

$$\begin{pmatrix} 0 \\ 0 \\ 1 \\ 0 \\ Y_{xx}^s - \frac{1}{\eta_2} \\ Y_{yx}^s \end{pmatrix} = \overline{\overline{Q}} \begin{pmatrix} B_I/A_I \\ C_I/A_I \\ D_I/A_I \\ E_I/A_I \\ F_I/A_I \\ G_I/A_I \end{pmatrix}, \tag{3.44}$$

where

$$\overline{\overline{Q}} =$$

$$\begin{pmatrix} e^{-jk_1 d} & 0 & e^{jk_1 d} & 0 & 0 & 0 \\ 0 & e^{-jk_1 d} & 0 & e^{jk_1 d} & 0 & 0 \\ 1 & 0 & 1 & 0 & -1 & 0 \\ 0 & 1 & 0 & 1 & 0 & -1 \\ \frac{-1}{\eta_1} & 0 & \frac{1}{\eta_1} & 0 & \frac{-1}{\eta_2} - Y_{xx}^s & -Y_{xy}^s \\ 0 & \frac{-1}{\eta_1} & 0 & \frac{1}{\eta_1} & -Y_{yx}^s & \frac{-1}{\eta_2} - Y_{yy}^s \end{pmatrix}. \tag{3.45}$$

Solving this system provides the relative field amplitudes in terms of wavenumbers and physical parameters of the structure (see (C.2) in Appendix C).

Similarly, for illumination $II$, the incident electric and magnetic fields in region 2

can be written as

$$\overline{E}^i_{2II} = A_{II}\hat{y}e^{jk_2z} \tag{3.46}$$

$$\overline{H}^i_{2II} = \frac{1}{\eta_2}\left(A_{II}\hat{x}\right)e^{jk_2z}, \tag{3.47}$$

and the expressions for the remaining field quantities are identical to (3.28)-(3.31), (3.34) and (3.35) with the subscript $II$ replacing the subscript $I$. The matrix system can be expressed as

$$\begin{pmatrix} 0 \\ 0 \\ 0 \\ 1 \\ Y^s_{xy} \\ Y^s_{yy} - \frac{1}{\eta_2} \end{pmatrix} = \overline{\overline{Q}} \begin{pmatrix} B_{II}/A_{II} \\ C_{II}/A_{II} \\ D_{II}/A_{II} \\ E_{II}/A_{II} \\ F_{II}/A_{II} \\ G_{II}/A_{II} \end{pmatrix} \tag{3.48}$$

and the relative field amplitudes $(A_{II}, B_{II}, C_{II}, D_{II}, E_{II}, F_{II}, G_I)$ can be found by solving this system (see (C.3) in Appendix C).

In order to find the sheet impedance, we first find $\overline{\overline{\eta}}_{in}$, the tensor input impedance (at $z = 0$) for normal incidence. In this case, it is easier to work with $\overline{\overline{Y}}_{in}$, the input admittance tensor $(\overline{\overline{Y}}_{in} = \overline{\overline{\eta}}^{-1}_{in})$, since the ground plane and the tensor impedance sheet are in parallel. At $z = 0$,

$$\begin{pmatrix} -H_{y2} \\ H_{x2} \end{pmatrix} = \begin{pmatrix} Y^{in}_{xx} & Y^{in}_{xy} \\ Y^{in}_{yx} & Y^{in}_{yy} \end{pmatrix} \begin{pmatrix} E_{x2} \\ E_{y2} \end{pmatrix}. \tag{3.49}$$

52

Two equations can be written using this boundary condition,

$$-H_{y2} = Y_{xx}^{in} E_{x2} + Y_{xy}^{in} E_{y2}$$
$$H_{x2} = Y_{yx}^{in} E_{x2} + Y_{yy}^{in} E_{y2},$$

(3.50)

where the $E_{x2}$, $E_{y2}$, $H_{x2}$, and $H_{y2}$ are the total (incident plus scattered) electric and magnetic fields in their respective directions in region 2, at $z = 0$. Using two instances of (3.50), one for each illumination, we can recast the matrix equation as

$$
\begin{pmatrix}
-H_{y2}^{I} \\
-H_{y2}^{II} \\
H_{x2}^{I} \\
H_{x2}^{II}
\end{pmatrix}
=
\begin{pmatrix}
E_{x2}^{I} & E_{y2}^{I} & 0 & 0 \\
E_{x2}^{II} & E_{y2}^{II} & 0 & 0 \\
0 & 0 & E_{x2}^{I} & E_{y2}^{I} \\
0 & 0 & E_{x2}^{II} & E_{y2}^{II}
\end{pmatrix}
\begin{pmatrix}
Y_{xx}^{in} \\
Y_{xy}^{in} \\
Y_{yx}^{in} \\
Y_{yy}^{in}
\end{pmatrix}
$$

(3.51)

where the superscript represents the illumination number.

Performing the matrix inverse of the electric field matrix and multiplying by the $\overline{H}$ vector allows the elements of the $\overline{\overline{Y}}_{in}$ matrix to be found,

$$Y_{xx}^{in} = \frac{E_{y2}^{I} H_{y2}^{II} - E_{y2}^{II} H_{y2}^{I}}{E_{x2}^{I} E_{y2}^{II} - E_{x2}^{II} E_{y2}^{I}}$$

(3.52)

$$Y_{xy}^{in} = \frac{E_{x2}^{II} H_{y2}^{I} - E_{x2}^{I} H_{y2}^{II}}{E_{x2}^{I} E_{y2}^{II} - E_{x2}^{II} E_{y2}^{I}}$$

(3.53)

$$Y_{yx}^{in} = \frac{E_{y2}^{II} H_{x2}^{I} - E_{y2}^{I} H_{x2}^{II}}{E_{x2}^{I} E_{y2}^{II} - E_{x2}^{II} E_{y2}^{I}}$$

(3.54)

$$Y_{yy}^{in} = \frac{E_{x2}^{I} H_{x2}^{II} - E_{x2}^{II} H_{x2}^{I}}{E_{x2}^{I} E_{y2}^{II} - E_{x2}^{II} E_{y2}^{I}}.$$

(3.55)

As previously mentioned, $E_{x2}$, $E_{y2}$, $H_{x2}$, and $H_{y2}$ are the total (incident plus scattered) electric and magnetic fields in their respective directions in region 2. The

total fields at the sheet $(z = 0)$ for illumination $I$ are given by (3.32-3.35)

$$E_{x2}^{I} = E_{x2I}^{i} + E_{x2I}^{r} = A_I + F_I \tag{3.56}$$

$$E_{y2}^{I} = E_{y2I}^{i} + E_{y2I}^{r} = G_I \tag{3.57}$$

$$H_{x2}^{I} = H_{x2I}^{i} + H_{x2I}^{r} = \frac{k_2}{\omega\mu_2} G_I \tag{3.58}$$

$$H_{y2}^{I} = H_{y2I}^{i} + H_{y2I}^{r} = \frac{k_2}{\omega\mu_2}(A_I - F_I). \tag{3.59}$$

The analogous fields at the sheet for illumination II are given by

$$E_{x2}^{II} = E_{x2II}^{i} + E_{x2II}^{r} = F_{II} \tag{3.60}$$

$$E_{y2}^{II} = E_{y2II}^{i} + E_{y2II}^{r} = A_{II} + G_{II} \tag{3.61}$$

$$H_{x2}^{II} = H_{x2I}^{i} + H_{x2I}^{r} = \frac{k_2}{\omega\mu_2}(A_{II} + G_{II}) \tag{3.62}$$

$$H_{y2}^{II} = H_{y2I}^{i} + H_{y2I}^{r} = \frac{-k_2}{\omega\mu_2} F_{II}. \tag{3.63}$$

Substituting equations (3.32-3.35), (3.46-3.47), and the relative field amplitudes into (3.52-3.55) and simplifying, a simple result is reached [53],

$$\begin{pmatrix} Y_{xx}^{in} & Y_{xy}^{in} \\ Y_{yx}^{in} & Y_{yy}^{in} \end{pmatrix} = \begin{pmatrix} Y_{xx}^{s} + \frac{\cot(k_1 d)}{\eta_1 j} & Y_{xy}^{s} \\ Y_{yx}^{s} & Y_{yy}^{s} + \frac{\cot(k_1 d)}{\eta_1 j} \end{pmatrix} \tag{3.64}$$

$$= \overline{\overline{Y}}_{sheet} + \begin{pmatrix} \frac{1}{j\eta_1 \tan(k_1 d)} & 0 \\ 0 & \frac{1}{j\eta_1 \tan(k_1 d)} \end{pmatrix}. \tag{3.65}$$

Once $\overline{\overline{Y}}_{in}$ is known, $\overline{\overline{Y}}_{sheet}$ can be found from $\overline{\overline{Y}}_{in}$ by merely subtracting the contribution of the ground plane and dielectric. It is apparent from (3.65) that the contribution of the ground plane and dielectric is isotropic. Another method of arriving at expression (3.65) using a transmission-line model, once $\overline{\overline{Y}}_{in}$ is known, is shown in Appendix A.

54

The tensor sheet impedance extraction method can be summarized as follows:

1. Perform two normal incidence simulations on the PCTIS unit cell: one with the incident electric field polarized in the $x$-direction (illumination $I$), and another with the incident electric field polarized in the $y$-direction (illumination $II$).

2. Measure the $x$- and $y$-directed scattered fields $(F_I, G_I)$, and $(F_{II}, G_{II})$ at the sheet for the first and second simulations, respectively. The incident fields, $A_I$ and $A_{II}$, need not be measured since they are stipulated in the simulation (amplitude of one and a phase of zero are convenient choices).

3. Calculate the total electric and magnetic fields at the sheet ($z = 0$) using (3.56) - (3.63).

4. Calculate the input admittance tensor $(\overline{\overline{Y}}_{in})$ using (3.52)-(3.55). An alternate, more elegant, method of finding $\overline{\overline{Y}}_{in}$ based on measured or simulated reflection coefficients is given in Appendix E.

5. Calculate the tensor sheet admittance $(\overline{\overline{Y}}_{sheet})$ from (3.65).

In the method outlined above, the tensor sheet admittance has been found using two normal-incidence scattering simulations without prior knowledge of the principal axes. Assuming that the frequency dependence of the sheet is $\overline{\overline{\eta}}_{sheet} = \frac{1}{(j\omega)\overline{\overline{c}}_{sheet}}$ for capacitive sheets and $\overline{\overline{\eta}}_{sheet} = (j\omega)\overline{\overline{l}}_{sheet}$ for inductive sheets, the dispersion equation of the two-layer structure can be used to predict the propagation characteristics of the simulated structure for all frequencies where the transverse unit cell dimension is much smaller than a guided wavelength. For more complicated geometries where the extracted sheet impedance tensor has mixed entries (both inductive and capacitive), the extraction procedure can be repeated for a number of frequencies to reveal its frequency dependence, as long as the homogenization process remains valid over the

frequency range of interest. In other words, curves can be generated for each element $(\eta_{xx}^s, \eta_{xy}^s, \eta_{yx}^s, \eta_{yy}^s)$ as a function of frequency.

The extraction method outlined above assumes that the only interaction between the ground plane and the impedance sheet is via propagating waves through the dielectric. Therefore, this method is strictly valid when the dielectric thickness, $d$, is larger than the widest printed feature size on the patterned metallic cladding [51]. If the ground plane is too close to the metallic cladding, the extracted tensor sheet impedance will not be accurate. In the next section, the tensor sheet impedance is extracted for example geometries and the propagation characteristics of the PCTISs is predicted using the dispersion equation (3.27). The results are then verified using a commercial full-wave electromagnetic solver (Ansys HFSS).

## 3.5 Verification of the Dispersion Equation and Sheet Extraction Method

In this section, the tensor sheet extraction method is applied to three example geometries and the propagation characteristics of the structures are predicted analytically using (3.27). The results are then compared to full-wave eigenmode simulations of the structures.

### 3.5.1 Anisotropic Capacitive Sheet over a Grounded Dielectric Substrate

An example geometry is shown in Fig. 3.5 [11]. The patterned metallic cladding is printed on a grounded dielectric substrate ($\epsilon_r = 10.2$) of thickness $d = 1.27$ mm. Two normal-incidence scattering simulations were performed at 10 GHz to extract the $\overline{\overline{Y}}_{sheet}$ of the patterned metallic cladding at this frequency. The first simulation (Fig. 3.6), denoted by subscript $I$, had a $x$-polarized incident electric field and the second simulation, denoted by subscript $II$, had a $y$-polarized incident electric field.

56

Figure 3.5: Example of a patterned metallic cladding printed over a RO3010 grounded dielectric substrate with thickness, $d = 1.27$ mm , $\epsilon_{r1} = 10.2$, and unit cell length, $a = 3$ mm. The grey areas represent metallization.
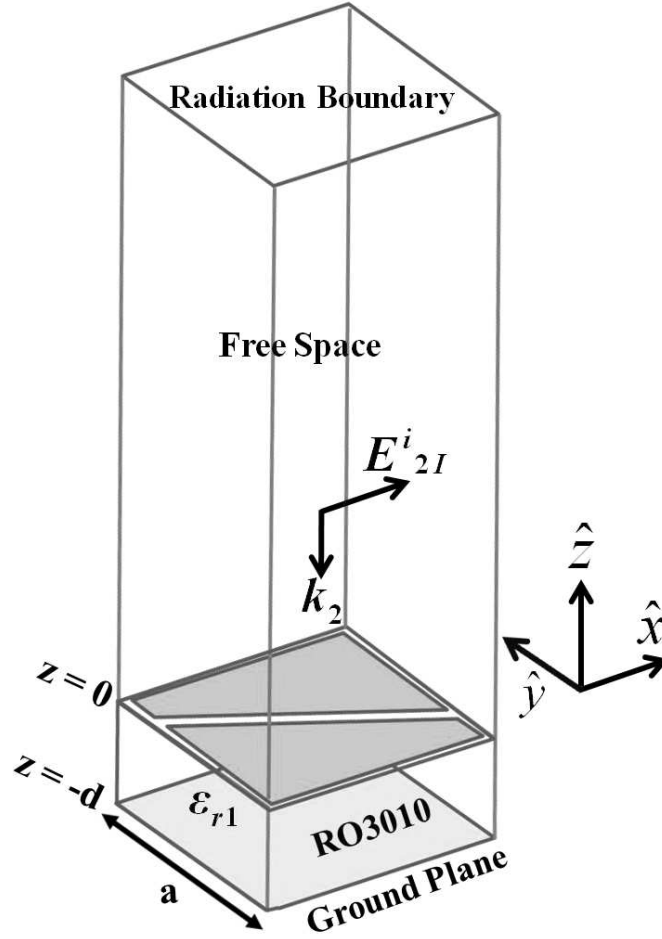
Figure 3.6: Scattering simulation setup for illumination $I$ with an incident plane wave polarized in the x-direction.

For simplicity, the incident field amplitudes ($A_I$ and $A_{II}$) were set equal to one with zero phase at the sheet ($z = 0$).

Using the fields calculator in Ansys HFSS, the scattered field amplitudes ($F_I$, $G_I$), and ($F_{II}$, $G_{II}$) were measured in the first and second simulations, respectively. The fields were measured at a plane $\lambda/2$ away from the sheet. This allowed sufficient space for the highly oscillatory fields near the gaps to subside. The phase of the measured field values were then de-embedded to find the fields at the sheet. The values were also averaged over the area of the unit cell for accuracy.

The measured values of the real and imaginary parts of the electric field at the

surface ($z = 0$) are given in Table 3.1. The incident fields, $A_I$ and $A_{II}$, were not

Table 3.1: Measured field amplitudes from illuminations $I$ and $II$ using Ansys HFSS.

| Description of Field Amplitudes | Variable | Re (V/m) | Im (V/m) |
|---|---|---|---|
| Scattered E-field in x-dir for I | $F_I$ | -0.51835 | -0.43308 |
| Scattered E-field in y-dir for I | $G_I$ | 0.29015 | 0.66711 |
| Scattered E-field in x-dir for II | $F_{II}$ | 0.28756 | 0.66685 |
| Scattered E-field in y-dir for II | $G_{II}$ | -0.05039 | 0.67177 |

measured since they are stipulated in the simulation (with an amplitude of one and a phase of zero in this example). The total electric and magnetic fields at $z = 0$ were calculated using (3.32-3.35) and (3.46-3.47). These fields were then substituted into (3.52-3.55) to find the input admittance tensor. Finally, the tensor sheet admittance was found from (3.65). Ignoring the negligible real parts of the impedance, the capacitive sheet impedance corresponding to the simulated geometry is:

$$\overline{\overline{\eta}}_{sheet} = \begin{pmatrix} -97.54j & -47.73j \\ -47.81j & -176.40j \end{pmatrix} \Omega \qquad (3.66)$$

at the simulation frequency of 10 GHz. The sheet impedance entries, $\eta^s_{xy}$ and $\eta^s_{yx}$, should be equal for a reciprocal system and are shown to be in very close agreement. The sheet impedance corresponds to a sheet capacitance of

$$\overline{\overline{C}}_{sheet} = \begin{pmatrix} 163.1681 & 333.4519 \\ 332.86472 & 90.2254 \end{pmatrix} fF. \qquad (3.67)$$

The principal axes are the directions in which the sheet impedance, and also the surface impedance, is diagonal. By finding the eigenvectors that diagonalize the sheet impedance (3.66), the angles of the principal axes are found to be $-25.25°$ and $64.79°$, and the diagonalized sheet impedance is given by

$$\overline{\overline{\eta}}^d_{sheet} = \begin{pmatrix} -75.03j & 0 \\ 0 & -198.91j \end{pmatrix} \Omega. \qquad (3.68)$$
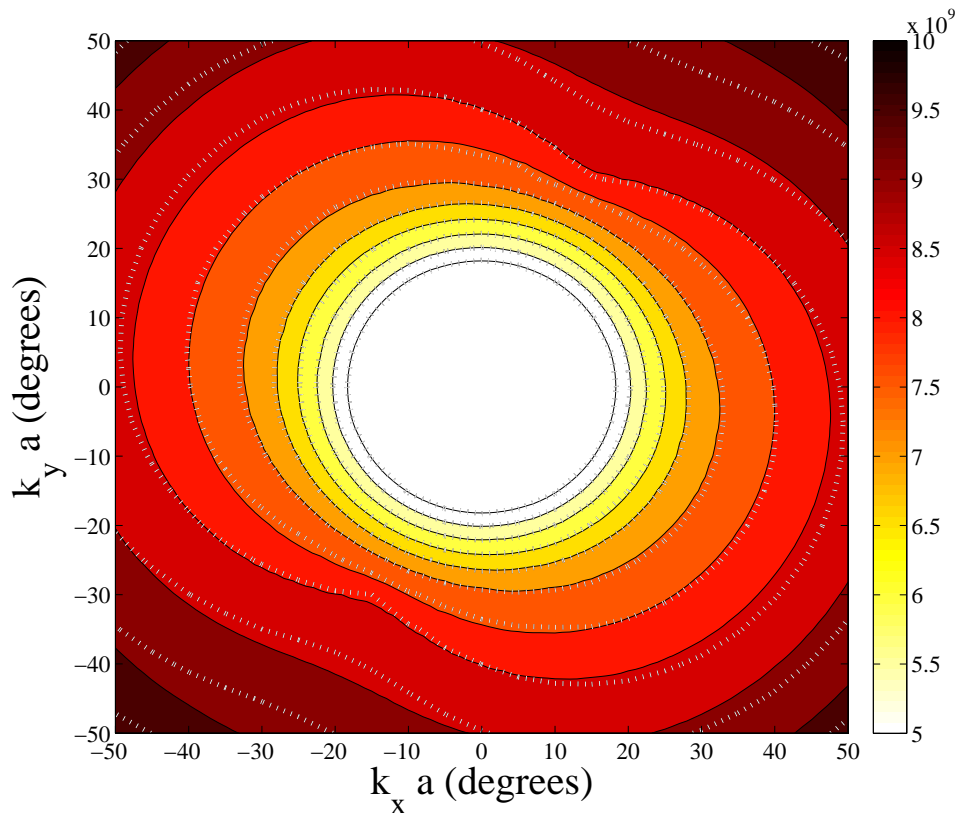
Figure 3.7: Full-wave eigenmode simulation vs. analytical prediction of the dispersion characteristics for the PCTIS shown in Fig. 3.5. The contour plot represents analytically predicted isofrequency contours from 5 GHz to 10 GHz. White dotted lines are the simulated result.

In theory, the angle between the two principal axes should be 90° but is found to be 90.04° due to the same numerical error that caused $\eta_{xy}^s$ and $\eta_{yx}^s$ to slightly differ. An analytically generated dispersion diagram showing isofrequency contours for the extracted sheet impedance over the grounded dielectric substrate are shown in Fig. 3.7 as colored contours. These are the dispersion contours for the first surface mode of the structure. They show close agreement with full-wave simulation results (dotted white lines) in the homogeneous limit: where the electrical size of the unit cell is much smaller than a guided wavelength. The Brillouin diagram, shown in Fig. 3.8, further verifies the agreement between the full-wave simulation results and analytical predictions below 10 GHz. Above 10 GHz, the agreement degrades since the unit cell
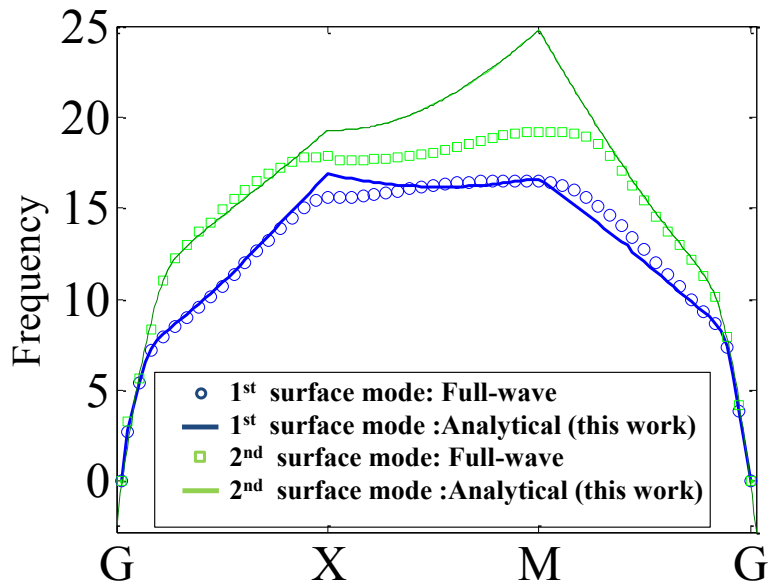
Figure 3.8: Brillouin diagram showing full-wave eigenmode simulation vs. analytical prediction of the dispersion characteristics for the PCTIS. The first two surface modes are shown. The first surface mode (lower in frequency) corresponds to the one shown in Fig. 3.7.

becomes larger with respect to a guided wavelength and the homogenization condition is less valid. Therefore, using the dispersion equation, it is possible to predict the propagation characteristics of the PCTIS depicted in Fig. 3.5 by simply performing two normal-incidence scattering simulations that characterize the metallic cladding as a tensor impedance sheet.

In order to compare results from the two-layer model described in this chapter, to methods used previously, the example geometry was also modeled as a single TIBC [10, 11]. A least squares method was used to fit the full-wave simulated dispersion curves to the dispersion equation for an idealized TIBC (3.7). Fig. 3.9(a) shows a comparison of dispersion contours for the fitted tensor vs. the dispersion diagram generated using full-wave simulation for three separate frequencies. The TIBC roughly approximates the dispersion curve at the fitting frequency of 8 GHz. It does not accurately predict the dispersion curves at other frequencies when a linear frequency dependence for the fitted surface impedance is assumed. Fig. 3.9(b) compares the

same three contours from full-wave simulation to dispersion contours generated analytically using the two-layer model presented in this chapter. These results show that the idealized TIBC does not accurately model the physics of the structure shown in Fig. 3.5. In general, the two-layer structure cannot be lumped into a single surface and analyzed using (3.7) if accurate propagation characteristics are desired.

### 3.5.2 Anisotropic Inductive Sheet over a Grounded Dielectric Substrate

Another example geometry (shown in Fig. 3.10) is analyzed to further verify the extraction method and dispersion analysis. In this case, the sheet impedance is inductive instead of capacitive and the dielectric substrate is significantly thicker than that of the first example ($\epsilon_r = 10.2$, $d = 6.0$ mm). The extracted sheet impedance tensor for the structure at 7 GHz is

$$\bar{\bar{\eta}}_{sheet} = \begin{pmatrix} 121.32j & 11.16j \\ 10.98j & 41.25j \end{pmatrix} \Omega. \tag{3.69}$$

A comparison between the analytically predicted and full-wave simulated dispersion contours is shown in Fig. 3.11, and close agreement is observed. One may predict that the principal axes are close to 0° and 90° based on the cell's topology. The calculated values are 7.50° and 97.88°. The slight tilt is due to the extreme curves in the meandered line. This agreement verifies that the method described in this chapter can model even electrically thick structures.

### 3.5.3 Rotated Anisotropic Inductive Sheet over a Grounded Dielectric Substrate

As a final example, the geometry of Fig. 3.10 was rotated by $-45°$ and then analyzed. This results in the geometry depicted in Fig. 3.12. Mathematically rotating
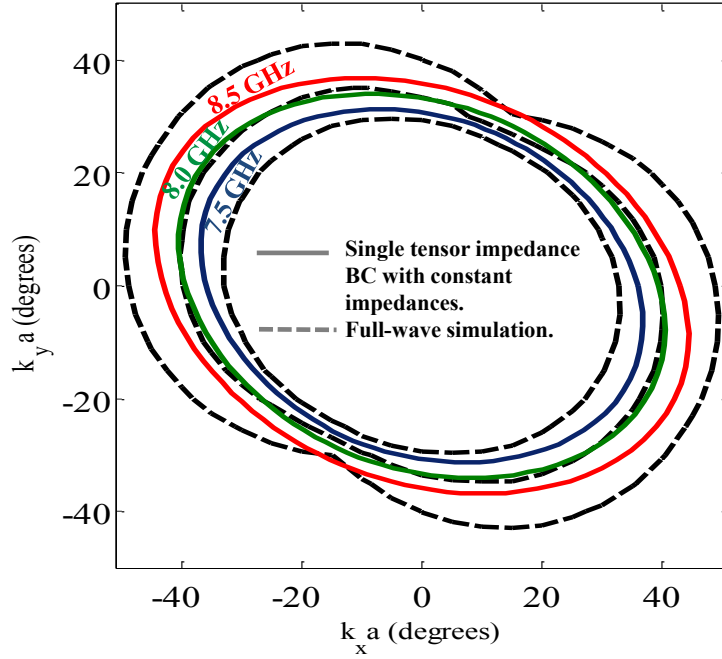
(a) Comparison of three isofrequency contours from full-wave simulation vs. analytically generated dispersion contours using the single, TIBC with a constant tensor surface inductance. The least squares fit was performed at 8 GHz. Other frequencies were projected using a linear frequency dependence.
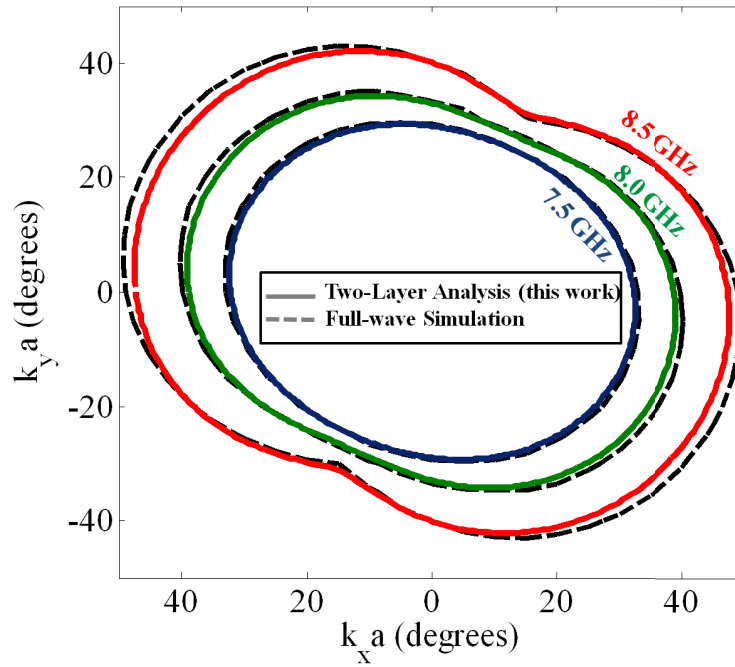


(b) Comparison of three isofrequency contours from full-wave simulation vs. analytically generated dispersion contours using the two-layer model with constant tensor sheet capacitance (this work).

Figure 3.9: Dispersion contours at 7.5 GHz, 8.0 GHz, and 8.5 GHz.
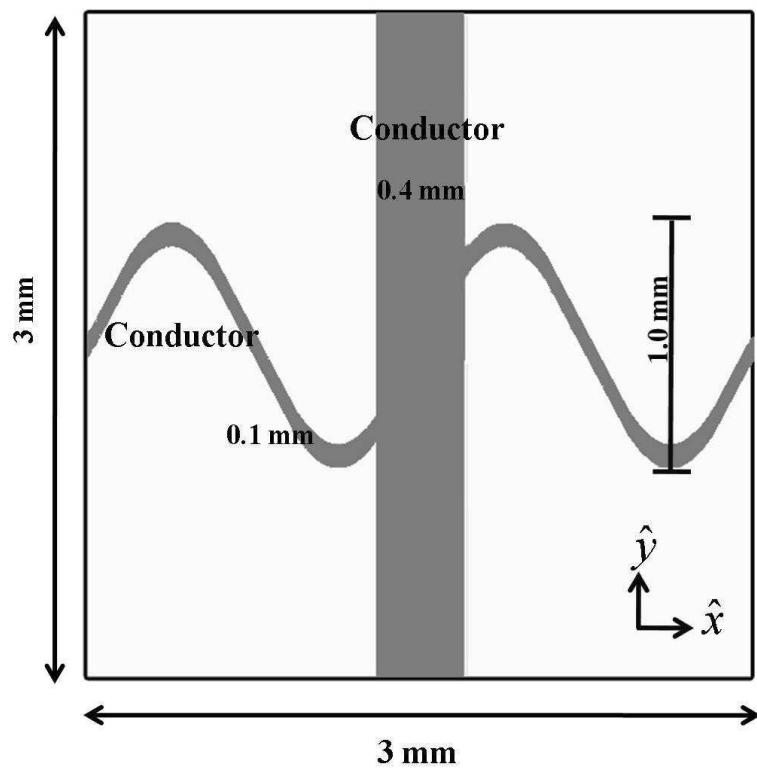
Figure 3.10: Example of a patterned metallic cladding printed over a grounded dielectric substrate with thickness, $d = 6.0$ mm , $\epsilon_{r1} = 10.2$, and unit cell length, $a = 3$ mm. Grey areas represent metallization.
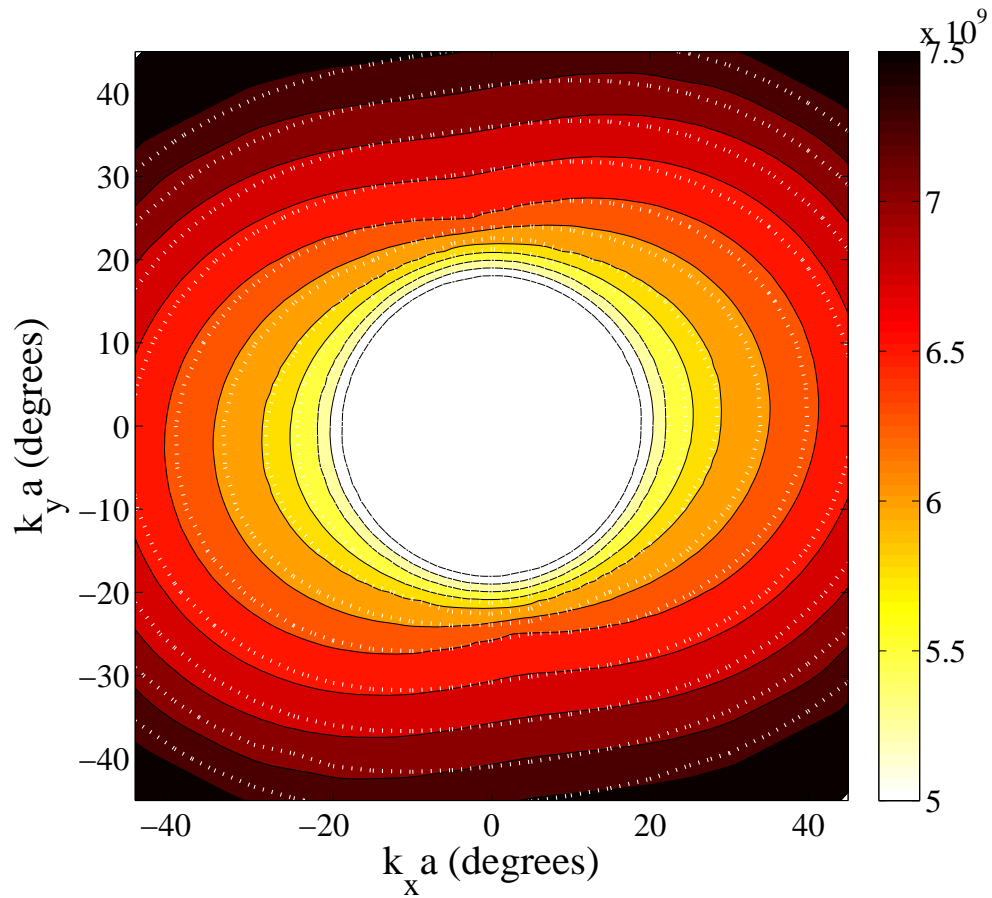
Figure 3.11: Full-wave eigenmode simulation vs. analytical prediction of the disper-sion characteristics for the PCTIS shown in Fig. 3.10. The contour plot represents analytically predicted isofrequency contours from 5 GHz to 7.5 GHz. White dotted lines are the simulated results.

the extracted sheet impedance tensor from the previous example by $-45°$ results in

$$\overline{\overline{\eta}}_{sheet} = \begin{pmatrix} 92.35j & -40.12j \\ -39.95j & 70.21j \end{pmatrix} \Omega. \tag{3.70}$$

The extraction at 7 GHz of the structure shown in Fig. 3.12 gives a sheet impedance tensor of

$$\overline{\overline{\eta}}_{sheet} = \begin{pmatrix} 91.46j & -39.27j \\ -39.26j & 69.29j \end{pmatrix} \Omega, \tag{3.71}$$

which agrees closely with (3.70). Fig. 3.13 shows the dispersion contours comparing full-wave results and analytically predicted results for the rotated structure shown in Fig. 3.12, and there is close agreement. The principal axes are found to be $-37.12°$ and $52.88°$. Fig. 3.14(a) and Fig. 3.14(b) show that these principal axes are indeed offset by about $-45°$ from those of the un-rotated version shown in Fig. 3.10.

## 3.6 Limitations

There are some limitations to the work presented in this chapter. The frequency dependence of the tensor impedance sheet, that models the patterned metallic cladding, cannot be directly inferred when the tensor sheet impedance is not purely capacitive or inductive. This can be overcome with interpolation, as described in Section 3.4.

In addition, the analytically predicted dispersion properties of a given structure are only valid within the homogeneous limit, since the metallic cladding is approximated as an impedance sheet extracted at normal incidence. Therefore, the unit cell size must be much smaller than the guided wavelength. The pole-zero method presented in [56] is valid for unit cell sizes on the order of a wavelength, but requires several full-wave simulations to characterize the sheet impedance. It also requires knowledge
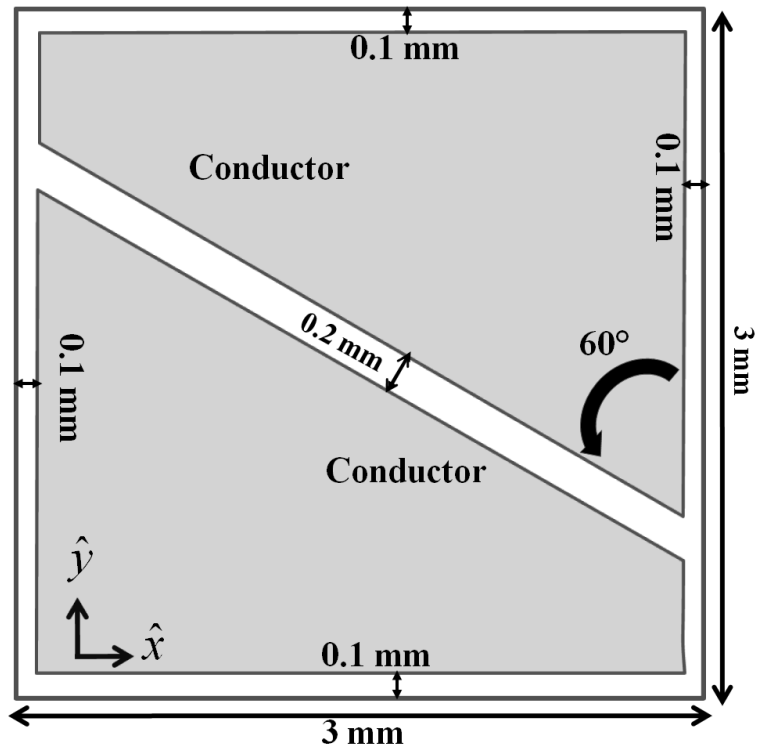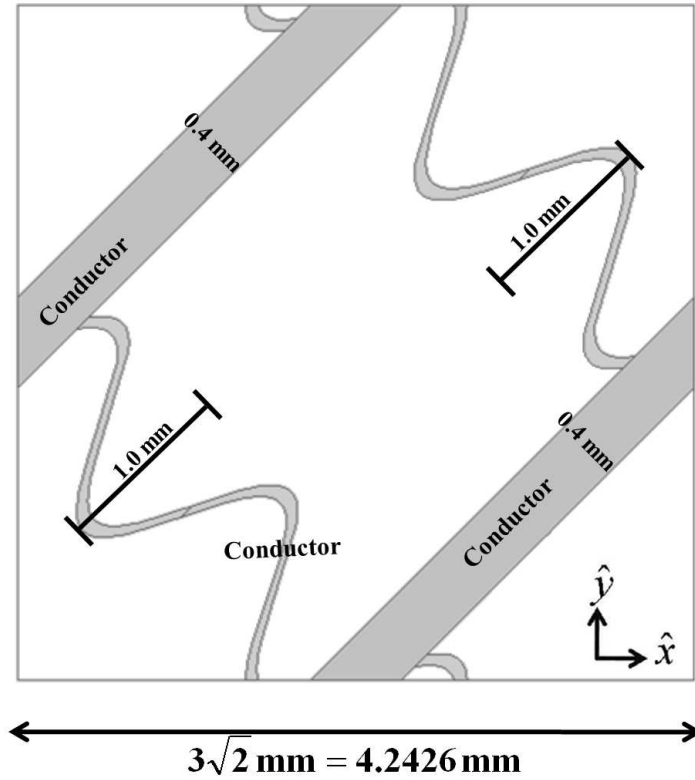
Figure 3.12: Example of a patterned metallic cladding printed over a grounded dielectric substrate with thickness, $d = 6.0$ mm , $\epsilon_{r1} = 10.2$, and unit cell length, $a = 3\sqrt{2}$ mm. Grey areas represent metallization. This PCTIS is the same as that in Fig. 3.10 rotated by $-45°$.
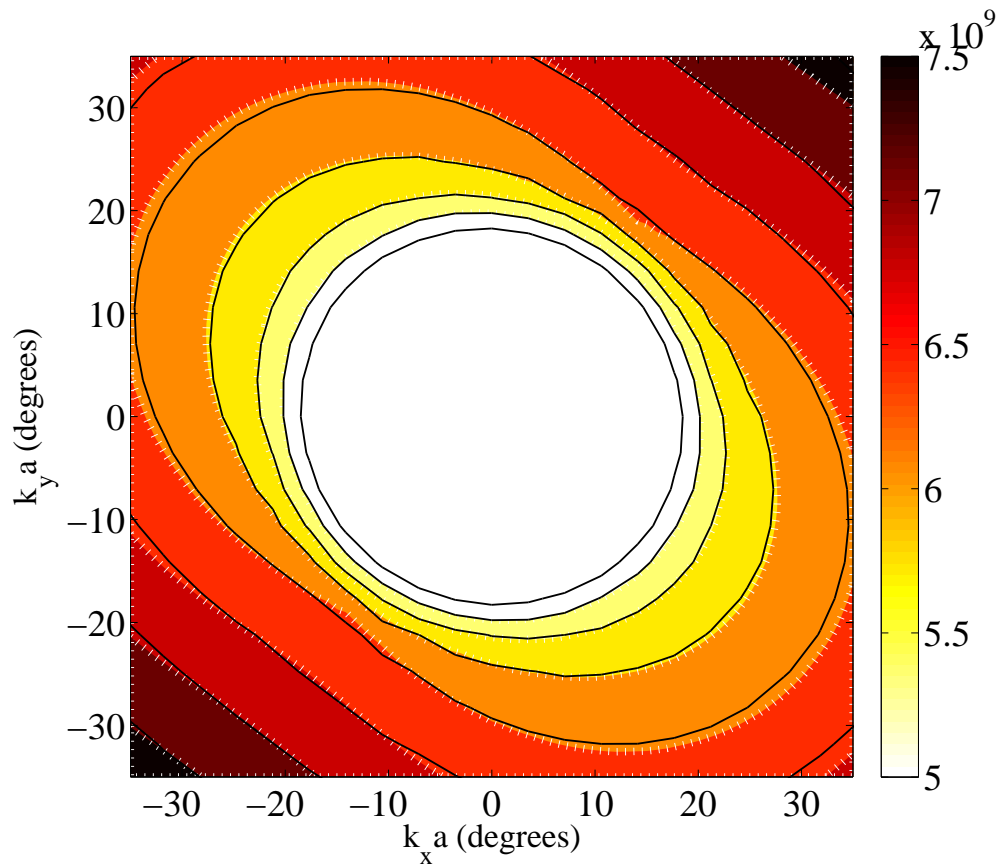
Figure 3.13: Full-wave eigenmode simulation vs. analytical prediction of the dispersion characteristics for the PCTIS shown in Fig. 3.12. The contour plot represents analytically predicted isofrequency contours from 5 GHz to 7.5 GHz. White dotted lines are the simulated results.

of the principal axes of the structure a priori. The method we present requires only two scattering simulations at normal incidence and does not require prior knowledge of the principal axes of the patterned metallic cladding.

Fabrication constraints impose certain limitations on minimum unit cell size. For example, maintaining a desired sheet inductance per unit length while reducing the unit cell size requires a lower inductance per unit cell. Lower inductance values can be achieved with wider traces. In order to maintain a desired sheet capacitance per unit length while reducing the unit cell size, a higher capacitance must be achieved in each unit cell. Higher capacitance values are typically achieved by patterning the metallic cladding of the PCTIS with smaller gaps. Therefore, fabrication processes (which dictate the smallest fabricable feature sizes) impose a limitation. For printed-circuit boards, commercial etching processes are limited to approximately 50 $\mu$m features. At optical frequencies, feature sizes as small as 40 nm have been reported [59].

When using unit cells to realize a surface impedance profile, the discretization must be smaller than the wavelength corresponding to the local wave number. Exactly how much smaller is determined by how much variation in the wave's phase and group velocity (spatial dispersion) one can tolerate for a particular design. This tradeoff between discretization and spatial dispersion is analogous to that in numerical methods for differential equations (such as TLM and FDTD) [60]. For printed circuit board structures based on transmission line networks, a typical guideline is that the unit cell size should be no larger than $\lambda/10$ for tolerable spatial dispersion [61, 62].

Additionally, while the methodology presented in this chapter is useful for analyzing PCTISs with arbitrarily large electrical thickness, the ground plane should be far enough from the metallic cladding to avoid evanescent coupling between it and the ground plane.

The method reported here is also limited to printed-circuit type structures, without vias. However, as in [52], vias could be modeled using an anisotropic substrate.

Further, the derived dispersion equation is valid for leaky-waves, but we have not solved for the complex leaky-wave roots since our focus has been on surface waves. Finally, spatial dispersion is also not taken into account in this initial work, but is a logical extension moving forward.

## 3.7 Chapter Summary

In this chapter, impedance surfaces that are tensorial (anisotropic) in nature are explored. A PCTIS consisting of an arbitrary patterned metallic cladding printed above a grounded dielectric substrate is studied analytically to find its dispersion equation. A novel method for extracting the tensor sheet impedance of the patterned metallic cladding using two normal incidence scattering simulations is also reported. Combining the dispersion equation with the extracted sheet impedance, the propagation characteristics of the PCTIS can be predicted analytically from two scattering simulations alone. The findings are verified using full-wave eigenmode simulations. In summary, (3.65) can be used to extract the tensor sheet impedance/admittance of an arbitrary periodic, metallic cladding printed over a grounded dielectric substrate from two normal incidence scattering simulations, without knowing the principal axes a priori. The extracted sheet admittance entries ($Y^s_{xx}$, $Y^s_{xy}$, $Y^s_{yx}$, and $Y^s_{yy}$) can then be used in (3.27) to analytically predict the structure's dispersion properties in the homogeneous limit. The approach described in this chapter more accurately predicts the dispersion properties of PCTISs than earlier analytical models [11, 16, 17, 18, 20, 22]. Two scattering simulations and post-processing are needed to describe the dispersion characteristics as opposed to performing time consuming eigenmode simulations over multiple propagation angles in order to characterize the structure. This speedup is especially useful when designing practical surfaces, which are typically electrically large, inhomogeneous surfaces consisting of electrically small unit cells [11, 22]. Hundreds of metallic cladding patterns need to be analyzed in order to build a sufficient

design database.

In the next chapter, the analysis of PCTISs is extended. A modified transverse resonance technique is presented, which provides an elegant method for finding the dispersion equations for TIBCs and PCTISs. The effective surface impedance of a PCTIS (analogous to the surface impedance of a TIBC) is found as a result of insight provided by the modified transverse resonance equations. Expressions for the group velocity and direction of power flow are also found for TIBCs and PCTISs.
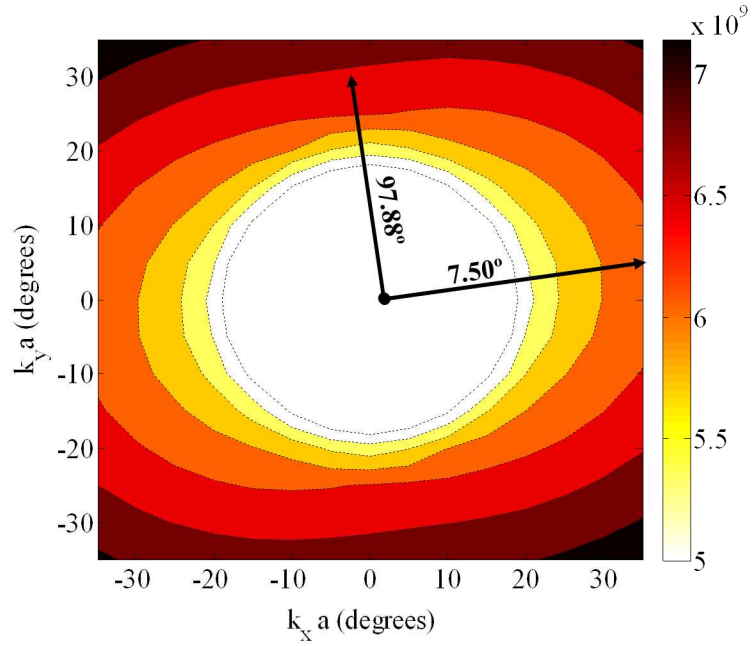
(a) Dispersion contours for the PCTIS shown in Fig. 3.10.
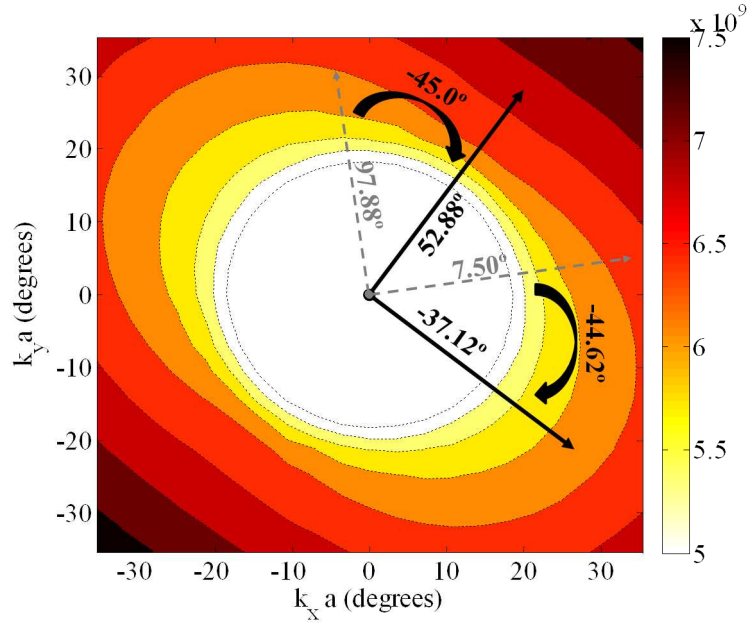


(b) Dispersion contours for the PCTIS shown in Fig. 3.10 rotated by $-45°$, as shown in Fig.3.12. As expected, this dispersion diagram is the same as Fig. 3.14(a) but with a $-45°$ rotation.

Figure 3.14: Dispersion contours from full-wave simulation. The principal axes (computed from the extracted tensor sheet impedances) are shown on the plots. The wave numbers have been scaled to account for differences in unit cell size between the unit cells pictured in Fig. 3.10 and Fig. 3.12.

# CHAPTER IV

# Effective Surface Impedance of a Printed-Circuit Tensor Impedance Surface

## 4.1   Introduction

In the previous chapter, printed-circuit tensor impedance surfaces (PCTISs) were analytically modeled as two-layer structures [53, 54, 55], as opposed to an idealized TIBC. The patterned metallic cladding was approximated as a tensor impedance sheet and the dispersion equation was derived through field analysis [53]. The unit cell of the patterned metallic cladding must be small compared to a wavelength and the ground plane sufficiently displaced from the cladding to avoid evanescent wave interaction. A method that allows one to extract the tensor sheet impedance of an arbitrary periodic metallic cladding was also proposed in the previous chapter [53]. In Chapter II, the transverse resonance technique was used to derive the dispersion equation for scalar impedance surfaces [47]. In this chapter, a modified transverse resonance technique is developed in order to analyze tensor impedance surfaces (TISs).

The transverse resonance technique was introduced by Marcuvitz in 1951 as a method for analyzing composite waveguide structures [41]. The technique was applied to traveling-wave antennas for the first time in [63]. Others applied the technique (and variants of it) to a large class of traveling-wave antennas with both rectangular

and circular cross-sections. [64, 65, 66, 67]. In the 1970's, the transverse resonance technique was used to model periodic, dielectric waveguides [68, 69] in order to study their propagation characteristics. More recently, printed-circuit structures [56, 70], multi-layer grating structures [71], as well as photonic bandgap [72] and electromagnetic bandgap [73] structures were analyzed and designed.

Historically, the transverse resonance technique has been used to analyze scalar impedance surfaces. In this chapter, we introduce a modified transverse resonance technique to analyze TISs. We use the modified transverse resonance approach to derive the dispersion equation for an arbitrary tensor sheet impedance over a grounded dielectric substrate. The approach provides added physical insight over the field analysis presented in Chapter III.

Section 4.2 reviews the application of the traditional transverse resonance method to a printed-circuit scalar impedance surface, which consists of a scalar sheet impedance over a grounded dielectric substrate. In Section 4.3, the modified transverse resonance technique is applied to an idealized TIBC, and the dispersion equation is derived. In Section 4.4, insights from the previous two sections are used to derive the dispersion equation of a PCTIS. A PCTIS consists of a subwavelength-patterned metallic cladding over a grounded dielectric substrate. The patterned metallic cladding is approximated as a homogenized tensor impedance sheet. We also use the modified transverse resonance technique to define an effective surface impedance for the PCTIS that is analogous to the idealized TIBC. The expression for the effective surface impedance of a PCTIS is verified through an analytical example. It is found that the effective surface impedance is, in general, dependent on the direction of propagation along the PCTIS. Therefore, it exhibits spatial dispersion. In Section 4.5, expressions for the group velocity and direction of power flow along a TIBC are found. It is shown that a PCTIS and a TIBC can have the same surface impedance but different directions of power flow due to the spatial dispersion of the PCTIS [74]. Expressions

for the group velocity and direction of power flow for a PCTIS, that take spatial dispersion into account, are also derived. Finally, Section 4.6 provides a discussion on the conditions necessary to approximate the PCTIS as an angle-independent TIBC.

The goal of this chapter is to advance the understanding of TISs (particularly those of the printed-circuit type) in order to facilitate the design of holographic and transformation-electromagnetics devices based on these surfaces [33]. A detailed understanding of TISs is an important step toward the control of surface and leaky waves for guided-wave or radiative applications. In the design of these surfaces, holographic or transformation-based methods would provide the surface impedance tensor and wave vector along the surface of interest. From these two quantities, the required sheet impedance could be determined.

## 4.2 Surface Impedance of a Printed-Circuit Scalar Impedance Surface.

A printed-circuit impedance surface consists of a periodically-patterned metallic cladding over a grounded dielectric substrate. In the case of a printed-circuit scalar impedance surface (Fig. 4.1), the metallic cladding is approximated as an isotropic impedance sheet of constant reactance. This allows the structure to be analytically modeled using a transmission-line model (Fig. 4.2) and its modal surface impedance found.

In Chapter II [47, 48], the transverse resonance technique was applied to a printed-circuit surface consisting of copper strips (modeled as a capacitive sheet) over a grounded dielectric substrate to calculate its $TM$ modal surface impedance. A method for extracting the sheet impedance of the metallic strips was discussed in Section 2.4 [47]. A general method to analyze printed-circuit scalar impedance surfaces using the transverse resonance technique is described next. Referring to Fig.
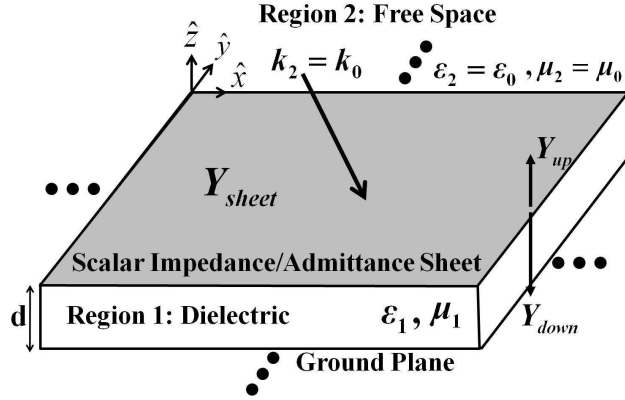
Figure 4.1: Analytical model for a printed-circuit scalar impedance surface consisting of a metallic cladding printed over a grounded dielectric substrate. The metallic cladding is modeled as an isotropic reactive impedance sheet.

4.1, the transverse resonance condition allows us to write

$$Y_{down}(z = 0^+) + Y_{up}(z = 0^+) = 0, \tag{4.1}$$

where $Y_{up}$ is the admittance looking up into free space from a plane just above the admittance sheet. $Y_{down}$ is the admittance looking down from the same plane, and is equal to the surface admittance. It is often convenient to use admittances instead of impedances since the impedance sheet and the ground plane are in parallel. A matrix representation of the transverse resonance condition can be written as

$$\overline{\overline{Y}}_{down}(z = 0^+)\overline{E}_t + \overline{\overline{Y}}_{up}(z = 0^+)\overline{E}_t = 0, \tag{4.2}$$

where $\overline{E}_t$ is the tangential electric field just above the sheet. This expression results from the continuity of the tangential magnetic field just above the impedance sheet. Referring to the $TM$ and $TE$ transmission-line models in Fig. 4.2, the admittance looking down is given by the sum of the admittance of the sheet, and that of the ground plane transferred through the dielectric by the distance, $d$. The transmission-line impedances and normal wave numbers used in the models are the $TM$ and $TE$

76

wave impedances and wave numbers, as shown in Fig. 4.2. Therefore, (4.2) can be expressed as

$$
\begin{pmatrix} Y_{sheet} & 0 \\ 0 & Y_{sheet} \end{pmatrix} \overline{E}_t
$$

$$
+ \begin{pmatrix} -j\left(Y_1 \frac{k_1}{k_{z1}}\right)\cot(k_{z1}d) & 0 \\ 0 & -j\left(Y_1 \frac{k_{z1}}{k_1}\right)\cot(k_{z1}d) \end{pmatrix} \overline{E}_t \tag{4.3}
$$

$$
- \begin{pmatrix} Y_0 \frac{k_0}{k_{z0}} & 0 \\ 0 & Y_0 \frac{k_{z0}}{k_0} \end{pmatrix} \overline{E}_t = 0,
$$

where the tangential wave number is assumed to be along the $x$ direction. It is clear that the $\overline{E}_t$ terms can be eliminated since all the matrices are diagonal. This yields two equations, a $TM$ dispersion equation,

$$
Y_0 \frac{k_0}{k_{z0}} = Y_{sheet} - j\left(Y_1 \frac{k_1}{k_{z1}}\right)\cot(k_{z1}d) \tag{4.4}
$$

and a $TE$ dispersion equation,

$$
Y_0 \frac{k_{z0}}{k_0} = Y_{sheet} - j\left(Y_1 \frac{k_{z1}}{k_1}\right)\cot(k_{z1}d). \tag{4.5}
$$

These are the dispersion equations for the $TM$ and $TE$ modes of a printed-circuit scalar impedance surface. These results are combined with the analysis of the TIBC (Section 4.3), in order to model two-dimensional anisotropic PCTISs in Section 4.4.

(a) TM transmission-line model.  (b) TE transmission-line model.
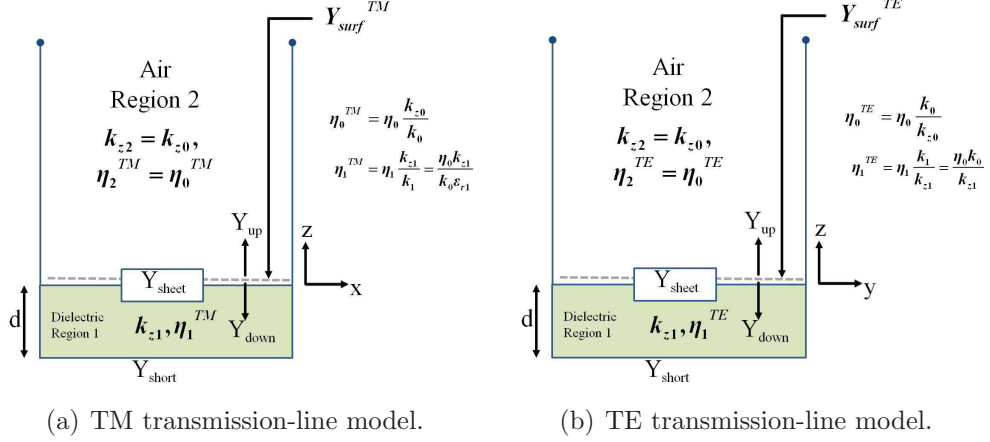
Figure 4.2: Modal transmission-line models for a isotropic impedance sheet over a grounded dielectric substrate.

## 4.3 Modified Transverse Resonance Technique applied to a TIS Modeled by Single Tensor Impedance Boundary Condition (TIBC)

The modified transverse resonance condition is a matrix representation analogous to that of (4.1), when the matrices are non-diagonal. In order to extend the modified transverse resonance technique to two-dimensional PCTISs, we first analyze an idealized tensor impedance surface: a tensor impedance boundary condition (TIBC) [10]. The surface impedance tensor,

$$\overline{\overline{\eta}}_{surf} = \begin{pmatrix} \eta_{xx} & \eta_{xy} \\ \eta_{yx} & \eta_{yy} \end{pmatrix}, \tag{4.6}$$

relates the tangential electric and magnetic fields at the surface,

$$\begin{pmatrix} E_x \\ E_y \end{pmatrix} = \begin{pmatrix} \eta_{xx} & \eta_{xy} \\ \eta_{yx} & \eta_{yy} \end{pmatrix} \begin{pmatrix} -H_y \\ H_x \end{pmatrix}. \tag{4.7}$$

The TIBC can support $TM$ waves (Fig. 4.3(a)), $TE$ waves (Fig. 4.3(b)), or a mixture of both. In general, this boundary condition is anisotropic, since $\eta_{xx}$, $\eta_{yy}$, and $\eta_{xy}$ can all have different values. Here, we assume that $\overline{\overline{\eta}}_{surf}$ is purely reactive (lossless) and reciprocal ($\eta_{xy} = \eta_{yx}$). We examine a few cases and eventually build up to the general case which considers propagation at an arbitrary angle along the surface. For consistency, we use a surface admittance tensor in the analysis, where

$$
\begin{pmatrix} Y_{xx} & Y_{xy} \\ Y_{yx} & Y_{yy} \end{pmatrix} = \begin{pmatrix} \eta_{xx} & \eta_{xy} \\ \eta_{yx} & \eta_{yy} \end{pmatrix}^{-1}.
\tag{4.8}
$$

### 4.3.1 Surface-wave propagation along the x-axis on a diagonal TIBC

First, let's examine the simplest anisotropic case where the surface impedance is diagonal:

$$
\overline{\overline{Y}}_{surf} = \begin{pmatrix} Y_{xx} & 0 \\ 0 & Y_{yy} \end{pmatrix}
\tag{4.9}
$$

and $Y_{xx} \neq Y_{yy}$. The separation relation is

$$
k_0^2 = k_t^2 + k_z^2,
\tag{4.10}
$$

where the wave number tangential to the surface, $k_t$, is given by

$$
k_t^2 = k_x^2 + k_y^2.
\tag{4.11}
$$

Let's assume that propagation along the surface is only along the $x$-axis ($k_t = k_x$, $k_y = 0$). Therefore, for a diagonal surface admittance (4.9), propagation is aligned with a principal axis of the surface. The principal axes are the directions in which the surface admittance tensor is diagonal. Enforcing the continuity of tangential magnetic
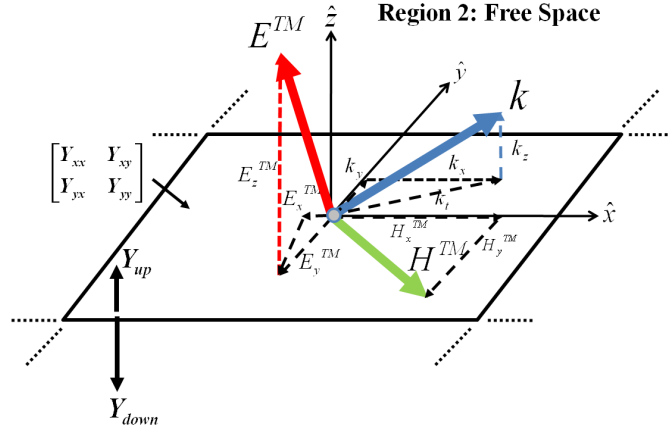
(a) TIS supporting a $TM$ wave.
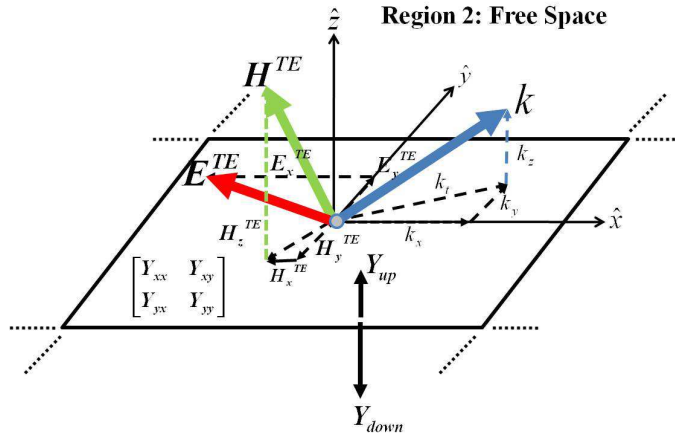


(b) TIS supporting a $TE$ wave.

Figure 4.3: Waves supported by a tensor impedance surface (TIS). In general, the surface can support $TM$, $TE$, or a mixture of both waves.

fields just above the surface, we can write:

$$\overline{\overline{Y}}_{down}\overline{E_t} + \overline{\overline{Y}}_{up}\overline{E_t} = 0 \tag{4.12}$$

or

$$\overline{\overline{Y}}_{down}\begin{pmatrix} E_x \\ E_y \end{pmatrix} + \overline{\overline{Y}}_{up}\begin{pmatrix} E_x \\ E_y \end{pmatrix} = 0 \tag{4.13}$$

Noting that $\overline{\overline{Y}}_{down}$ is the surface admittance tensor, and $\overline{\overline{Y}}_{up}$ is a diagonal matrix containing the $TM$ and $TE$ wave admittances of region 2 (free space), yields

$$\begin{pmatrix} Y_{xx} & 0 \\ 0 & Y_{yy} \end{pmatrix} \begin{pmatrix} E_x \\ E_y \end{pmatrix} + \begin{pmatrix} Y_0 \frac{k_0}{k_z} & 0 \\ 0 & Y_0 \frac{k_z}{k_0} \end{pmatrix} \begin{pmatrix} E_x \\ E_y \end{pmatrix} = 0. \qquad (4.14)$$

or

$$\begin{pmatrix} Y_{xx} + Y_0 \frac{k_0}{k_z} & 0 \\ 0 & Y_{yy} + Y_0 \frac{k_z}{k_0} \end{pmatrix} \begin{pmatrix} E_x \\ E_y \end{pmatrix} = 0. \qquad (4.15)$$

Setting the determinant of this matrix equal to zero yields the dispersion equation,

$$\left( Y_{xx} + Y_0 \frac{k_0}{k_z} \right) \left( Y_{yy} + Y_0 \frac{k_z}{k_0} \right) = 0. \qquad (4.16)$$

It is clear that (4.16) is satisfied when

$$Y_{xx} = -Y_0 \frac{k_0}{k_z} \qquad (4.17)$$

or

$$Y_{yy} = -Y_0 \frac{k_z}{k_0} \qquad (4.18)$$

Therefore, for propagation along the $x$-axis, a $TM$ mode is supported by $Y_{xx}$, or a $TE$ mode is supported by $Y_{yy}$. Equation (4.16) expands to

$$k_0^2 \left( \frac{1}{Y_{xx}} \right) + k_z^2 \left( \frac{1}{Y_{yy}} \right) + k_0 k_z \left( 1 + \frac{1}{Y_{xx}} \frac{1}{Y_{yy}} \right) = 0. \qquad (4.19)$$

This matches the dispersion equation (23) given in [10] under the condition that $\eta_{xy} = 0$ and $\eta_{yx} = 0$.

### 4.3.2 Surface-wave propagation along the x-axis on a non-diagonal TIBC

Next, we consider propagation along the $x$-axis ($k_t = k_x$, $k_y = 0$) of a full (non-diagonal) TIBC. Since the surface impedance tensor is not diagonal ($Y_{xx}$, $Y_{xy} = Y_{yx}$, and $Y_{yy}$ are all non-zero), the propagation direction does not align with either of the principal axes of the TIBC. Applying continuity of the tangential magnetic fields (see (4.12)) yields the modified transverse resonance condition:

$$
\begin{pmatrix} Y_{xx} & Y_{xy} \\ Y_{yx} & Y_{yy} \end{pmatrix} \begin{pmatrix} E_x \\ E_y \end{pmatrix} + \begin{pmatrix} Y_0 \frac{k_0}{k_z} & 0 \\ 0 & Y_0 \frac{k_z}{k_0} \end{pmatrix} \begin{pmatrix} E_x \\ E_y \end{pmatrix} = 0, \tag{4.20}
$$

or

$$
\begin{pmatrix} Y_{xx} + Y_0 \frac{k_0}{k_z} & Y_{xy} \\ Y_{yx} & Y_{yy} + Y_0 \frac{k_z}{k_0} \end{pmatrix} \begin{pmatrix} E_x \\ E_y \end{pmatrix} = 0. \tag{4.21}
$$

Setting the determinant of the matrix equal to zero, results in the dispersion equation

$$
\left( Y_{xx} + Y_0 \frac{k_0}{k_z} \right) \left( Y_{yy} + Y_0 \frac{k_0}{k_z} \right) - Y_{xy} Y_{yx} = 0. \tag{4.22}
$$

This expands to

$$
k_0^2 \left( \frac{Y_{yy}}{Y_0} \right) + k_z^2 \left( \frac{Y_{xx}}{Y_0} \right) + k_0 k_z \left( 1 + \frac{Y_{xx}}{Y_0} \frac{Y_{yy}}{Y_0} - \frac{Y_{xy}}{Y_0} \frac{Y_{yx}}{Y_0} \right) = 0. \tag{4.23}
$$

Expressed in terms of surface impedance values, the dispersion equation becomes:

$$
k_0^2 \frac{\eta_{xx}}{\eta_0} + k_z^2 \frac{\eta_{yy}}{\eta_0} + k_0 k_z \left( 1 + \frac{\eta_{xx}}{\eta_0} \frac{\eta_{yy}}{\eta_0} - \frac{\eta_{xy}}{\eta_0} \frac{\eta_{yx}}{\eta_0} \right) = 0, \tag{4.24}
$$

which exactly matches dispersion equation (23) from [10], for $x$-directed propagation. As expected, the $TM$ and $TE$ waves are mixed and are not separable as they were in (4.16) because propagation is not along a principal axis of the structure.
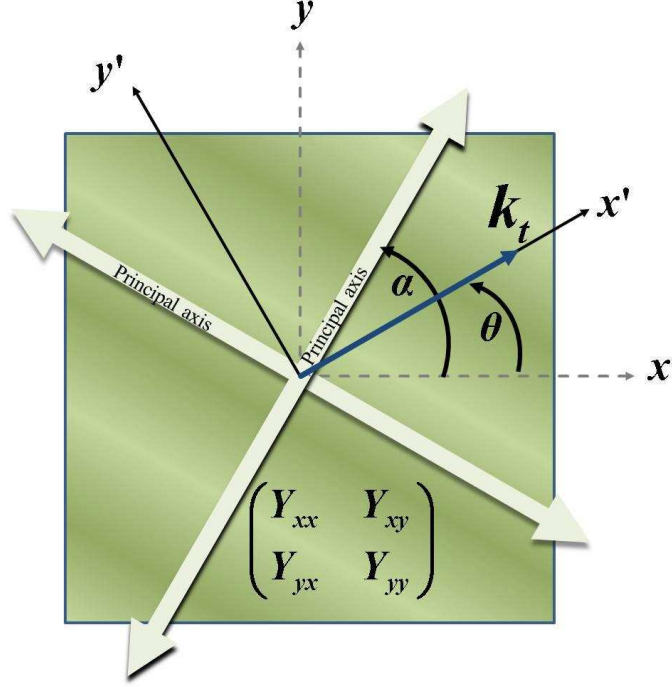
Figure 4.4: Diagram of an arbitrary tensor impedance surface with principal axes at $\alpha$ and $\alpha + 90°$. Tangential propagation, $(\overline{k}_t)$ occurs at an angle $\theta$ with respect to the $x$-axis. The $x'$ axis is aligned with $\overline{k}_t$.

### 4.3.3 Surface-wave propagation at an arbitrary angle along a non-diagonal TIBC

So far, we have only considered propagation along the $x$-direction. In order to analyze propagation at an arbitrary angle $\theta$ (with respect to the $x$-axis) along the surface, a new coordinate system (primed coordinates) is defined such that propagation is purely along the $x'$-axis, as shown in Fig. (4.4). The new coordinate system is given by the $x'$ and $y'$ axes. The primed system is a rotated version (about the $z$-axis) of the original $x, y$ system by an angle $\theta$.

The surface impedance in the primed coordinate system is given by rotating the original surface impedance by $\theta$,

$$\overline{\overline{Y}}_{surf}' = \begin{pmatrix} Y'_{xx} & Y'_{xy} \\ Y'_{yx} & Y'_{yy} \end{pmatrix} = R^T(\theta) \begin{pmatrix} Y_{xx} & Y_{xy} \\ Y_{yx} & Y_{yy} \end{pmatrix} R(\theta), \qquad (4.25)$$

83

where $R(\theta)$ is the rotation matrix,

$$R(\theta) = \begin{pmatrix} \cos\theta & -\sin\theta \\ \sin\theta & \cos\theta \end{pmatrix}.$$  (4.26)

Applying continuity of the tangential magnetic fields in the primed coordinate system yields,

$$R^T(\theta) \begin{pmatrix} Y_{xx} & Y_{xy} \\ Y_{yx} & Y_{yy} \end{pmatrix} R(\theta) \begin{pmatrix} E'_x \\ E'_y \end{pmatrix} + \begin{pmatrix} Y_0 \frac{k_0}{k_z} & 0 \\ 0 & Y_0 \frac{k_z}{k_0} \end{pmatrix} \begin{pmatrix} E'_x \\ E'_y \end{pmatrix} = 0.$$  (4.27)

or

$$\begin{pmatrix} Y'_{xx} & Y'_{xy} \\ Y'_{yx} & Y'_{yy} \end{pmatrix} \begin{pmatrix} E'_x \\ E'_y \end{pmatrix} + \begin{pmatrix} Y_0 \frac{k_0}{k_z} & 0 \\ 0 & Y_0 \frac{k_z}{k_0} \end{pmatrix} \begin{pmatrix} E'_x \\ E'_y \end{pmatrix} = 0.$$  (4.28)

Comparing (4.28) and (4.20), it is clear that the dispersion equation is identical to (4.23), if the unprimed admittances are replaced by primed admittances:

$$k_0^2 \left( \frac{Y'_{yy}}{Y_0} \right) + k_z^2 \left( \frac{Y'_{xx}}{Y_0} \right) + k_0 k_z \left( 1 + \frac{Y'_{xx}}{Y_0} \frac{Y'_{yy}}{Y_0} - \frac{Y'_{xy}}{Y_0} \frac{Y'_{yx}}{Y_0} \right) = 0.$$  (4.29)

As a special case, let's assume the principal axes of the structure are at the angles $\alpha$ and $\alpha + 90°$, as shown in Fig. 4.4. By definition, these are the rotation angles that result in a diagonalized $\overline{\overline{Y}}_{surf}{}'$. When propagation is along the principal axes of the TIBC, the $TM$ and $TE$ waves decouple as they did in (4.14).
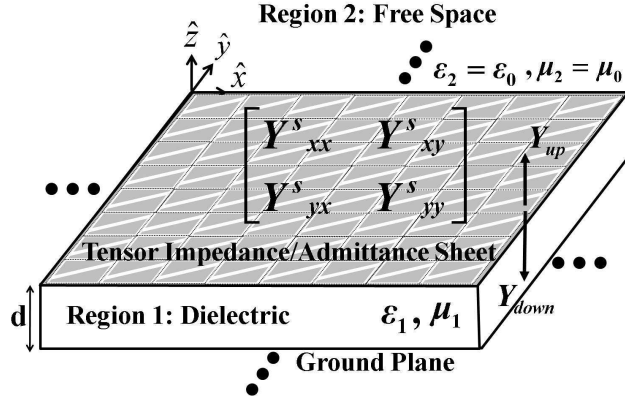
Figure 4.5: Analytical model for a PCTIS consisting of a subwavelength-patterned metallic cladding over a grounded dielectric substrate. The metallic cladding is modeled as a tensor sheet impedance.

## 4.4 Effective Surface Impedance of a PCTIS

The patterned metallic cladding of a PCTIS will again be modeled as a tensor admittance sheet. A method for extracting the tensor sheet admittance of a patterned metallic cladding was presented in Chapter III and Appendix E [53]. Here, we combine the analysis of printed-circuit scalar impedance surfaces from Section 4.2, with the analysis of single TIBCs from Section 4.3, in order to derive the dispersion equation of PCTISs and define their effective surface impedance/admittance.

As shown in Fig. 4.5, the PCTIS is modeled as a tensor admittance sheet over a grounded dielectric substrate. It should be noted that the tensor admittance sheet, denoted with the superscript $s$, is distinct from the tensor surface admittance discussed in Section 4.3. The tensor sheet admittance is defined in terms of surface current density $\overline{J}$,

$$\begin{pmatrix} J_x \\ J_y \end{pmatrix} = \begin{pmatrix} Y_{xx}^s & Y_{xy}^s \\ Y_{yx}^s & Y_{yy}^s \end{pmatrix} \begin{pmatrix} E_x \\ E_y \end{pmatrix}. \tag{4.30}$$

Continuity of magnetic fields just above the sheet (modified transverse resonance condition) dictates that

$$\overline{\overline{Y}}_{down}\overline{E}_t + \left[\overline{\overline{Y}}_{up}\right]\overline{E}_t = 0 \tag{4.31}$$

Using the primed coordinate system that aligns with the direction of propagation (direction of $\bar{k}_t$) yields

$$\begin{pmatrix} Y_{xx}^{s'} & Y_{xy}^{s'} \\ Y_{yx}^{s'} & Y_{yy}^{s'} \end{pmatrix} \begin{pmatrix} E_x' \\ E_y' \end{pmatrix}$$

$$+ \left[ \begin{pmatrix} -j\left(Y_1 \frac{k_1}{k_{z1}}\right)\cot(k_{z1}d) & 0 \\ 0 & -j\left(Y_1 \frac{k_{z1}}{k_1}\right)\cot(k_{z1}d) \end{pmatrix} \right.$$

$$\left. + \begin{pmatrix} Y_2 \frac{k_2}{k_{z2}} & 0 \\ 0 & Y_2 \frac{k_{z2}}{k_2} \end{pmatrix} \right] \begin{pmatrix} E_x' \\ E_y' \end{pmatrix} = 0, \tag{4.32}$$

where $\overline{\overline{Y}}_{down}$ includes the $TM$ and $TE$ admittances of the tensor sheet impedance, dielectric, and ground plane. $\overline{\overline{Y}}_{up}$ includes the $TM$ and $TE$ admittances of free space. By setting the determinant of the system equal to zero, the following dispersion equation is obtained,

$$k_1 k_2 k_{z1} k_{z2} Y_2^2 + k_1 k_{z1} k_{z2}^2 Y_2 Y_{xx}^{s'}$$

$$- k_1 k_2 k_{z1} k_{z2} Y_{xy}^{s'} Y_{yx}^{s'} + k_1 k_2^2 k_{z1} Y_2 Y_{yy}^{s'}$$

$$+ k_1 k_2 k_{z1} k_{z2} Y_{xx}^{s'} Y_{yy}^{s'}$$

$$- j k_2^2 k_{z1}^2 Y_1 Y_2 \cot(k_{z1}d)$$

$$- j k_1^2 k_{z2}^2 Y_1 Y_2 \cot(k_{z1}d)$$

$$- j k_2 k_{z1}^2 k_{z2} Y_1 Y_{xx}^{s'} \cot(k_{z1}d)$$

$$- j k_1^2 k_2 k_{z2} Y_1 Y_{yy}^{s'} \cot(k_{z1}d)$$

$$- k_1 k_2 k_{z1} k_{z2} Y_1^2 \cot^2(k_{z1}d) = 0. \tag{4.33}$$

This is the dispersion equation of a PCTIS as a function of frequency, the normal

wave number, and sheet admittance. Given that

$$
\begin{pmatrix} Y_{xx}^{s\prime} & Y_{xy}^{s\prime} \\ Y_{yx}^{s\prime} & Y_{yy}^{s\prime} \end{pmatrix} = R^T(\theta) \begin{pmatrix} Y_{xx}^{s} & Y_{xy}^{s} \\ Y_{yx}^{s} & Y_{yy}^{s} \end{pmatrix} R(\theta) \tag{4.34}
$$

and noting that $k_1 = \omega\sqrt{\mu_1\epsilon_1}$, $k_2 = \omega\sqrt{\mu_2\epsilon_2}$, $Y_1 = \sqrt{\frac{\epsilon_1}{\mu_1}}$, and $Y_2 = \sqrt{\frac{\epsilon_2}{\mu_2}}$, the dispersion equation (4.33) can be written as

$$
\begin{aligned}
&4\epsilon_1 k_1^2 k_2^2 k_{z1} k_{z2} \mu_2 \omega \cos^2(k_{z1}d) \\
&+ j\sin(2k_{z1}d) \\
&\quad [2\epsilon_1 k_2^4 k_{z1}^2 \mu_1 \omega + 2\epsilon_2 k_1^4 k_{z2}^2 \mu_2 \omega \\
&\quad + k_1^4 k_2^2 k_{z2} \mu_2 Y_{xx}^s + \epsilon_1 k_2^2 k_{z1}^2 k_{z2} \mu_1 \mu_2 \omega^2 Y_{xx}^s \\
&\quad + k_1^4 k_2^2 k_{z2} \mu_2 Y_{yy}^s + \epsilon_1 k_2^2 k_{z1}^2 k_{z2} \mu_1 \mu_2 \omega^2 Y_{yy}^s \\
&\quad - k_2^2 k_{z2} \mu_2 (k_1^4 - \epsilon_1 k_{z1}^2 \mu_1 \omega^2)(Y_{xx}^s - Y_{yy}^s)\cos(2\theta) \\
&\quad - k_2^2 k_{z2} \mu_2 (k_1^4 - \epsilon_1 k_{z1}^2 \mu_1 \omega^2)(Y_{xy}^s + Y_{yx}^s)\sin(2\theta)] \\
&- 2k_1^2 k_{z1} \mu_1 \sin^2(k_{z1}d) \\
&\quad [2\epsilon_2 k_2^2 k_{z2} \omega + k_2^4 Y_{xx}^s + \epsilon_2 k_{z2}^2 \mu_2 \omega^2 Y_{xx}^s \\
&\quad - 2k_2^2 k_{z2} \mu_2 \omega Y_{xy}^s Y_{yx}^s + k_2^4 Y_{yy}^s + \epsilon_2 k_{z2}^2 \mu_2 \omega^2 Y_{yy}^s \\
&\quad + 2k_2^2 k_{z2} \mu_2 \omega Y_{xx}^s Y_{yy}^s \\
&\quad - (k_2^4 - \epsilon_2 k_{z2}^2 \mu_2 \omega^2)(Y_{xx}^s - Y_{yy}^s)\cos(2\theta) \\
&\quad - (k_2^4 - \epsilon_2 k_{z2}^2 \mu_2 \omega^2)(Y_{xy}^s + Y_{yx}^s)\sin(2\theta)] = 0.
\end{aligned} \tag{4.35}
$$

It is identical to (3.27) in Chapter III [53] when $k_x$ and $k_y$, are replaced with $k_x = k_t\cos(\theta)$ and $k_y = k_t\sin(\theta)$. In order to find the effective surface admittance of a PCTIS, we compare the expression derived using the modified transverse resonance condition for a TIBC, to the one derived for the PCTIS. The dispersion equation of a idealized TIBC (4.27) can be rewritten in the primed coordinate system as:

$$
\left[ R^T(\theta) \begin{pmatrix} Y_{xx} & Y_{xy} \\ Y_{yx} & Y_{yy} \end{pmatrix} R(\theta) \right] \begin{pmatrix} E'_x \\ E'_y \end{pmatrix} = - \begin{pmatrix} Y_2 \frac{k_2}{k_{z2}} & 0 \\ 0 & Y_2 \frac{k_{z2}}{k_2} \end{pmatrix} \begin{pmatrix} E'_x \\ E'_y \end{pmatrix}. \quad (4.36)
$$

We can express the electric field vector in the $x - y$ coordinate system using the following relation

$$
\begin{pmatrix} E_x \\ E_y \end{pmatrix} = R(\theta) \begin{pmatrix} E'_x \\ E'_y \end{pmatrix}. \quad (4.37)
$$

Substituting (4.37) into (4.36) results in

$$
\left[ R^T(\theta) \begin{pmatrix} Y_{xx} & Y_{xy} \\ Y_{yx} & Y_{yy} \end{pmatrix} R(\theta) \right] \begin{pmatrix} E'_x \\ E'_y \end{pmatrix} = - \begin{pmatrix} Y_2 \frac{k_2}{k_{z2}} & 0 \\ 0 & Y_2 \frac{k_{z2}}{k_2} \end{pmatrix} R^T(\theta) \begin{pmatrix} E_x \\ E_y \end{pmatrix}.
$$

$$(4.38)$$

Applying the $R(\theta)$ operator to the matrices on both sides of the equation yields

$$
R(\theta) \left[ R^T(\theta) \begin{pmatrix} Y_{xx} & Y_{xy} \\ Y_{yx} & Y_{yy} \end{pmatrix} R(\theta) \right] \begin{pmatrix} E'_x \\ E'_y \end{pmatrix} = R(\theta) \begin{pmatrix} -Y_2 \frac{k_2}{k_{z2}} & 0 \\ 0 & -Y_2 \frac{k_{z2}}{k_2} \end{pmatrix} R^T(\theta) \begin{pmatrix} E_x \\ E_y \end{pmatrix}.
$$

$$(4.39)$$

The expression above simplifies to

$$
\left[ \begin{pmatrix} Y_{xx} & Y_{xy} \\ Y_{yx} & Y_{yy} \end{pmatrix} \right] \begin{pmatrix} E_x \\ E_y \end{pmatrix} = R(\theta) \begin{pmatrix} -Y_2 \frac{k_2}{k_{z2}} & 0 \\ 0 & -Y_2 \frac{k_{z2}}{k_2} \end{pmatrix} R^T(\theta) \begin{pmatrix} E_x \\ E_y \end{pmatrix}. \quad (4.40)
$$

Noting that $R^T(\theta) = R(-\theta)$, and $R(\theta) = R^T(-\theta)$,

$$\left[ \begin{pmatrix} Y_{xx} & Y_{xy} \\ Y_{yx} & Y_{yy} \end{pmatrix} \right] \begin{pmatrix} E_x \\ E_y \end{pmatrix} = R^T(-\theta) \begin{pmatrix} -Y_2 \frac{k_2}{k_{z2}} & 0 \\ 0 & -Y_2 \frac{k_{z2}}{k_2} \end{pmatrix} R(-\theta) \begin{pmatrix} E_x \\ E_y \end{pmatrix}.$$

(4.41)

The surface admittance (in $x - y$ coordinate system)

$$\overline{\overline{Y}}_{surf} = \begin{pmatrix} Y_{xx} & Y_{xy} \\ Y_{yx} & Y_{yy} \end{pmatrix},$$

(4.42)

appears in square brackets on the left hand side of (4.41). The transverse resonance expression for a PCTIS is now be manipulated into a similar form to reveal the effective surface impedance of a PCTIS. The transverse resonance equation (4.32) for the PCTIS can be rewritten as:

$$\left[ R^T(\theta) \begin{pmatrix} Y^s_{xx} & Y^s_{xy} \\ Y^s_{yx} & Y^s_{yy} \end{pmatrix} R(\theta) + \begin{pmatrix} -j\left(Y_1\frac{k_1}{k_{z1}}\right)\cot(k_{z1}d) & 0 \\ 0 & -j\left(Y_1\frac{k_{z1}}{k_1}\right)\cot(k_{z1}d) \end{pmatrix} \right] \begin{pmatrix} E'_x \\ E'_y \end{pmatrix}$$
$$= - \begin{pmatrix} Y_2\frac{k_2}{k_{z2}} & 0 \\ 0 & Y_2\frac{k_{z2}}{k_2} \end{pmatrix} \begin{pmatrix} E'_x \\ E'_y \end{pmatrix}.$$

(4.43)

Applying the same manipulations shown above for the TIBC, this equation can be recast as

$$
\left[ \begin{pmatrix} Y_{xx}^s & Y_{xy}^s \\ Y_{yx}^s & Y_{yy}^s \end{pmatrix} + R^T(-\theta) \begin{pmatrix} -j\left(Y_1\frac{k_1}{k_{z1}}\right)\cot(k_{z1}d) & 0 \\ 0 & -j\left(Y_1\frac{k_{z1}}{k_1}\right)\cot(k_{z1}d) \end{pmatrix} R(-\theta) \right] \begin{pmatrix} E_x \\ E_y \end{pmatrix}
$$
$$
= R^T(-\theta) \begin{pmatrix} -Y_2\frac{k_2}{k_{z2}} & 0 \\ 0 & -Y_2\frac{k_{z2}}{k_2} \end{pmatrix} R(-\theta) \begin{pmatrix} E_x \\ E_y \end{pmatrix}.
$$

$$(4.44)$$

The right hand sides of (4.44) and (4.41) are the same. Comparing the left hand sides, it is clear that the surface admittance of the PCTIS is given by the quantity within the square brackets of (4.44). Therefore, the effective surface admittance of a PCTIS in the $x - y$ coordinate system is

$$
\overline{\overline{Y}}_{surf}(\theta) = \begin{pmatrix} Y_{xx}(\theta) & Y_{xy}(\theta) \\ Y_{yx}(\theta) & Y_{yy}(\theta) \end{pmatrix}
$$
$$
= \begin{pmatrix} Y_{xx}^s & Y_{xy}^s \\ Y_{yx}^s & Y_{yy}^s \end{pmatrix} + R^T(-\theta) \begin{pmatrix} -j\left(Y_1\frac{k_1}{k_{z1}}\right)\cot(k_{z1}d) & 0 \\ 0 & -j\left(Y_1\frac{k_{z1}}{k_1}\right)\cot(k_{z1}d) \end{pmatrix} R(-\theta).
$$

$$(4.45)$$

It is equal to the sum of the sheet admittance and the rotated admittance of the grounded dielectric by an angle $-\theta$. Equation (4.45) shows that when the tensor sheet (modeling the metallic cladding) and the grounded dielectric substrate are treated as a single surface, the surface impedance/admittance becomes dependent on $k_{z1}$. The normal wave number $(k_{z1})$, however, is a function of the propagation angle along the surface. Therefore, the surface impedance/admittance of a PCTIS is a function of propagation angle. This is in contrast to the single TIBC (4.42), which is angle independent. In other words, the surface impedance of a PCTIS exhibits spatial dispersion due to its dielectric thickness.
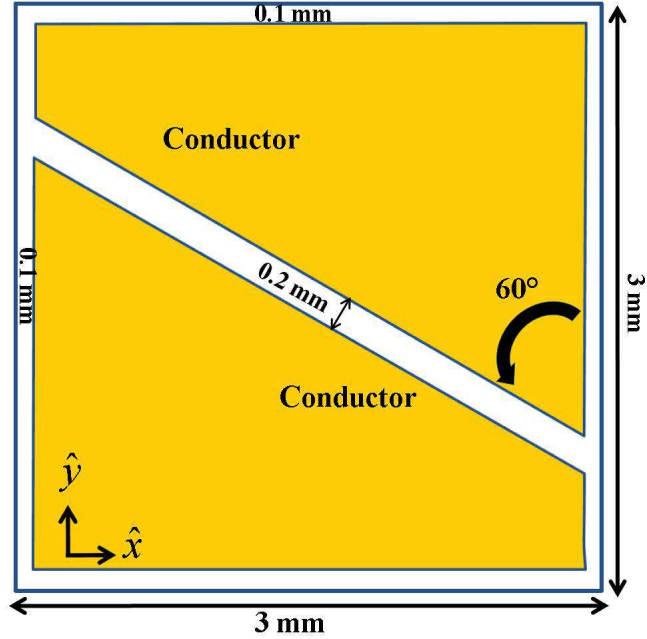
Figure 4.6: Patterned metallic cladding printed over a RO3010 grounded dielectric substrate with thickness, $d = 1.27$ mm , $\epsilon_{r1} = 10.2$, and unit cell length: $a = 3$ mm. The dark areas represent metallization.

### 4.4.1 Verification of the Angle-Dependent Tensor Surface Impedance for a PCTIS

Next, an example is presented that verifies the expression for the effective surface admittance (4.45) of a PCTIS. A PCTIS with the periodic metallic cladding shown in Fig. 4.6 was analyzed in Chapter III [53]. The extracted sheet impedance for this structure was found to be

$$\bar{\bar{\eta}}_{sheet} = -j \begin{pmatrix} 121.93 & 59.76 \\ 59.66 & 220.5 \end{pmatrix} \Omega. \tag{4.46}$$

at 8 GHz. The dispersion curves for the first guided mode of this PCTIS were generated using (4.33). They are shown in Fig. 4.7 with solid lines for for 7.5 GHz, 8 GHz, and 8.5 GHz. There is close agreement with full-wave eigenmode results from Ansys HFSS (dashed lines in Fig. 4.7), within the homogeneous limit. As previously
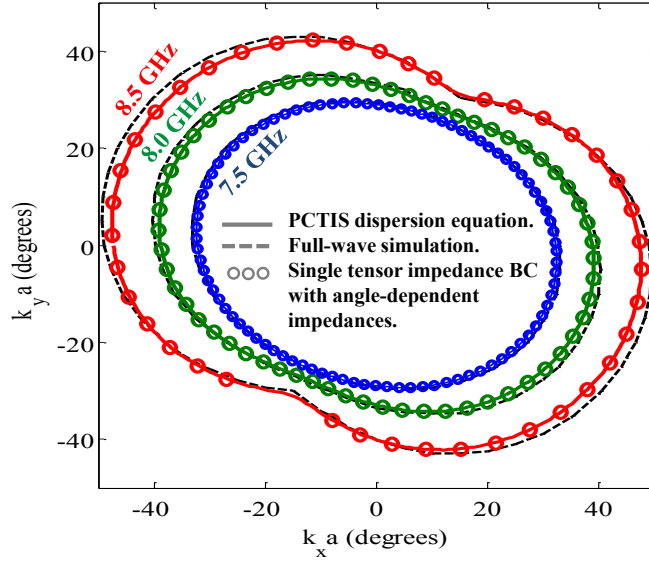
Figure 4.7: Isofrequency dispersion contours for 7.5 GHz, 8.0 GHz, 8.5 GHz. Dashed lines are full-wave results from an eigenmode solver. Solid lines are analytical predictions using dispersion equation (4.33) for a PCTIS. Circles are analytical predictions using dispersion equation (4.48) for a single TIBC with angle-dependent surface impedances/admittances (4.45).

described in Chapter III, a least squares method is used to fit the full-wave data (dashed lines) to (4.29), in order to find the closest surface admittance tensor that is independent of $\theta$,

$$\bar{\bar{\eta}}_{fitted} = j \begin{pmatrix} 364.34 & -88.55 \\ -88.55 & 226.48 \end{pmatrix} \Omega. \tag{4.47}$$

The closest fit (solid lines) is compared to full-wave simulation results (dashed lines) in Fig. 4.8.

The angle-independent surface admittance roughly approximates the dispersion curve at the fitting frequency of 8 GHz. It does not accurately predict the dispersion curves at other frequencies when a linear frequency dependence for the fitted surface impedance (4.47) is assumed. These results demonstrate that, in general, the dispersion characteristics of the PCTIS cannot be accurately modeled by (4.29): the
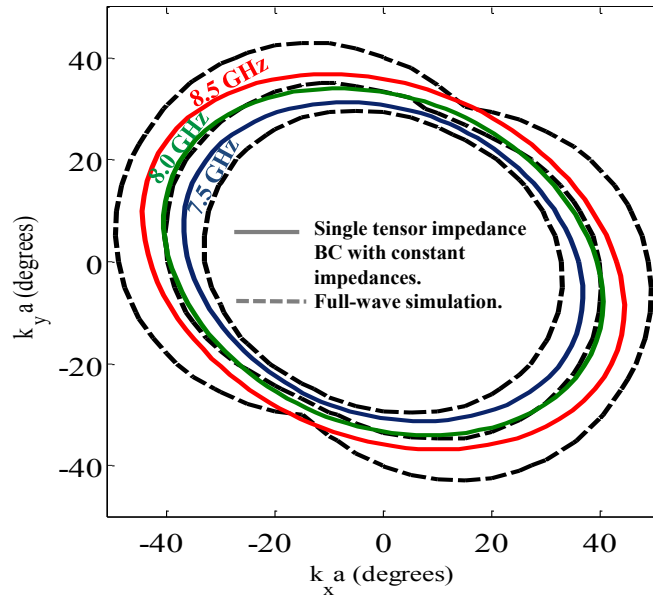
Figure 4.8: Isofrequency dispersion contours for 7.5 GHz, 8.0 GHz, 8.5 GHz. Dashed lines are full-wave results from an eigenmode solver. Solid lines are analytical predictions using the dispersion equation (4.29) for a single TIBC with a constant tensor impedance/admittance. The least squares fit (4.47) was performed at 8 GHz. Other frequencies were predicted by assuming a linear frequency dependence for the surface reactance of the TIBC.

dispersion equation for a TIBC. However, using a modified version of (4.29),

$$k_0^2 \left( \frac{Y'_{yy}(\theta)}{Y_0} \right) + k_z^2 \left( \frac{Y'_{xx}(\theta)}{Y_0} \right) + k_0 k_z \left( 1 + \frac{Y'_{xx}(\theta)}{Y_0} \frac{Y'_{yy}(\theta)}{Y_0} - \frac{Y'_{xy}(\theta)}{Y_0} \frac{Y'_{yx}(\theta)}{Y_0} \right) = 0,$$

(4.48)

where the tensor admittances are angle-dependent, the dispersion characteristics of the PCTIS can be accurately predicted. The angle-dependent tensor admittances are given by (4.45). The circles in Fig. 4.7 show the dispersion curves generated using dispersion equation (4.48) for a TIBC with angle-dependent surface admittances. The close agreement verifies that (4.45) is indeed the expression for the angle-dependent effective surface impedance of a PCTIS. Fig. 4.9 shows the angle-dependent tensor surface impedance entries used to generate the circles in Fig. 4.7 at 8 GHz. A log scale is used for the surface impedance values since the variation is large. For comparison purposes, the closest $\theta$-independent surface impedance tensor (found using a least squares fitting at 8 GHz), given by (4.47), is overlaid (dashed lines) in Fig. 4.9. The kinks that create the peanut shape in Fig. 4.7 occur when the tensor impedance sheet resonates with the grounded dielectric substrate. That is, the effective surface impedance exhibits a parallel resonance and therefore, the determinant of (4.45) approaches zero. The surface impedance entries plotted in Fig. 4.9, given by the inverse of (4.45), spike at these points. This drastic increase in surface impedance causes a dramatic change (kink) in the shape of the dispersion curve of Fig. 4.7 at $\theta \approx 60°$ and $\theta \approx 240°$.

The effective surface impedance of a PCTIS (4.45) is analogous to the surface impedance of a TIS (4.42) in that it represents the ratio of tangential electric field to tangential magnetic field at its surface. However, due to spatial dispersion, a PCTIS can have the same surface impedance (4.45) as a TIS (4.42) for a given $\theta$, but support a different direction of power flow. The analysis presented above can be used in design, to find the sheet impedance necessary to implement a desired surface
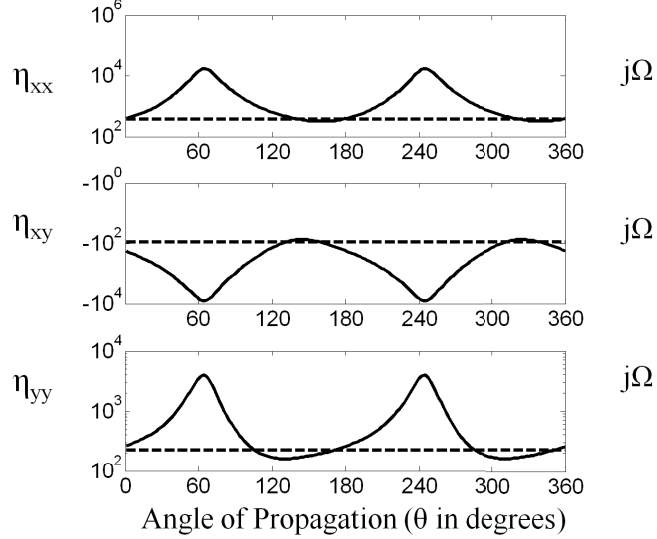
Figure 4.9: Surface impedance (solid lines) of the structure shown in Fig. 4.6 as a function of propagation angle along the surface at 8 GHz. $\eta_{yx}$ is not plotted since it is identical to $\eta_{xy}$. Dashed lines represent the closest $\theta$-independent tensor (4.47) found using a single TIBC.

impedance for a specific angle of propagation.

In the next section, the expressions for group velocity and the direction of power flow are found for both an idealized TIBC and a practical PCTIS. From their respective surface impedance expressions (4.42) and (4.45), the power flow along a TIBC and a PCTIS is derived as a function of tangential wave vector. The PCTIS exhibits spatial dispersion due to its electrical thickness. As a result, a PCTIS can have the same surface impedance as a TIBC, but a different direction of power flow. The expressions for direction of power along a TIBC and a PCTIS are verified with a full-wave electromagnetic solver.

## 4.5  Group Velocity and Power Flow along TISs and PCTISs

In the previous section, it was shown that a TIBC can model a PCTIS if the surface impedance of the TIBC is replaced with an effective surface impedance that is a function of the direction of propagation along the surface (wave vector). In other
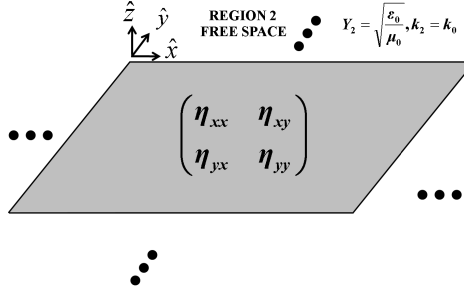
Figure 4.10: Idealized TIBC in the $x - y$ plane.

words, the effective surface impedance of a PCTIS is a function of the transverse wave vector $(\bar{k}_t)$ and is therefore spatially dispersive. The spatial dispersion results from the PCTIS's thickness: thickness of the grounded dielectric substrate.

In general, an angle-independent TIBC and a PCTIS can have the same surface impedance but different directions of power flow. This difference arises due to the spatial dispersion inherent to PCTISs. In the next section, expressions are derived for the group velocity of an idealized TIBC and a PCTIS as a function of the transverse wave number. Expressions for the direction of power flow are valuable since arbitrary control of fields on a surface often requires knowledge of the wave vector and power flow at every point on the surface [75, 76].

### 4.5.1 Direction of power flow along an idealized TIBC

The TIBC can be represented with an admittance tensor:

$$
\bar{\bar{\eta}}_{surf} = \begin{pmatrix} \eta_{xx} & \eta_{xy} \\ \eta_{yx} & \eta_{yy} \end{pmatrix} = \begin{pmatrix} Y_{xx} & Y_{xy} \\ Y_{yx} & Y_{yy} \end{pmatrix}^{-1}
$$
$$
= \frac{1}{\det Y} \begin{pmatrix} Y_{yy} & -Y_{xy} \\ -Y_{yx} & Y_{xx} \end{pmatrix}.
$$

$$(4.49)$$

The dispersion equation for an idealized TIBC, can be rewritten in a different form than (4.23),

$$
k_2 k_{z2}(Y_{xx}Y_{yy} - Y_{xy}Y_{yx} + Y_2^2) + k_x k_y Y_2(-Y_{xy} - Y_{yx})
$$
$$
+ (k_2^2 - k_x^2)(Y_{xx}Y_2) + (k_2^2 - k_y^2)(Y_{yy}Y_2) = 0, \tag{4.50}
$$

where $k_x^2 + k_y^2 + k_{z2}^2 = k_2^2$. The dispersion equation (4.50) is a function of frequency and transverse wave number and can be represented as:

$$
f(\omega, k_x, k_y) = 0. \tag{4.51}
$$

The group velocity is given by

$$
\vec{v_g} = v_{gx}\hat{x} + v_{gy}\hat{y} = \frac{\partial \omega}{\partial k_x}\hat{x} + \frac{\partial \omega}{\partial k_y}\hat{y}. \tag{4.52}
$$

Differentiating the dispersion equation with respect to $k_x$, and $k_y$ separately yields

$$
\frac{\partial}{\partial k_x}f(\omega, k_x, k_y) =
$$
$$
\left[\frac{\partial}{\partial k_x}Y_{xx}\right](k_2^2 Y_2 - k_x^2 Y_2 + k_2 k_{z2}Y_{yy})
$$
$$
- \left[\frac{\partial}{\partial k_x}Y_{xy}\right](k_x k_y Y_2 + k_2 k_{z2}Y_{yx})
$$
$$
- \left[\frac{\partial}{\partial k_x}Y_{yx}\right](k_x k_y Y_2 + k_2 k_{z2}Y_{xy})
$$
$$
+ \left[\frac{\partial}{\partial k_x}Y_{yy}\right](k_2^2 Y_2 - k_y^2 Y_2 + k_2 k_{z2}Y_{xx}) \tag{4.53}
$$
$$
+ \left[\frac{\partial}{\partial k_x}k_{z2}\right](Y_2^2 - Y_{xy}Y_{yx} + Y_{xx}Y_{yy})k_2
$$
$$
+ \left[\frac{\partial}{\partial k_x}k_2\right](2k_2 Y_2(Y_{xx} + Y_{yy})
$$
$$
+ k_{z2}(Y_2^2 - Y_{xy}Y_{yx} + Y_{xx}Y_{yy}))
$$
$$
- Y_2(2k_x Y_{xx} + k_y(Y_{xy} + Y_{yx})) = 0
$$

and

$$\frac{\partial}{\partial k_y} f(\omega, k_x, k_y) =$$

$$\left[\frac{\partial}{\partial k_y} Y_{xx}\right] (k_2^2 Y_2 - k_x^2 Y_2 + k_2 k_{z2} Y_{yy})$$

$$- \left[\frac{\partial}{\partial k_y} Y_{xy}\right] (k_x k_y Y_2 + k_2 k_{z2} Y_{yx})$$

$$- \left[\frac{\partial}{\partial k_y} Y_{yx}\right] (k_x k_y Y_2 + k_2 k_{z2} Y_{xy})$$

$$+ \left[\frac{\partial}{\partial k_y} Y_{yy}\right] (k_2^2 Y_2 - k_y^2 Y_2 + k_2 k_{z2} Y_{xx}) \qquad (4.54)$$

$$+ \left[\frac{\partial}{\partial k_y} k_{z2}\right] (Y_2^2 - Y_{xy} Y_{yx} + Y_{xx} Y_{yy}) k_2$$

$$+ \left[\frac{\partial}{\partial k_y} k_2\right] (2 k_2 Y_2 (Y_{xx} + Y_{yy})$$

$$+ k_{z2} (Y_2^2 - Y_{xy} Y_{yx} + Y_{xx} Y_{yy}))$$

$$- Y_2 (2 k_y Y_{yy} + k_x (Y_{xy} + Y_{yx})) = 0,$$

respectively. The $[\frac{\partial}{\partial k_x} Y_{**}]$ and $[\frac{\partial}{\partial k_y} Y_{**}]$ terms in (4.53) and (4.54) are given by $-\frac{Y_{**}}{\omega} \frac{\partial \omega}{\partial k_x}$ and $-\frac{Y_{**}}{\omega} \frac{\partial \omega}{\partial k_y}$ respectively, if the surface is purely inductive. These expressions are fairly simple since the tensor admittance entries depend on frequency, but not the tangential wave number. Substituting the simplified derivatives (F.2)-(F.5) from Appendix F into (4.53) and solving for $\frac{\partial w}{\partial k_x}$ yields the group velocity in the $x$-direction,

$$v_{gx}^{\text{TIS}} = \frac{\partial \omega}{\partial k_x} = \frac{\omega(k_{z2} Y_2 (2 k_x Y_{xx} + k_y (Y_{xy} + Y_{yx})) + k_2 k_x (Y_2^2 + \det Y))}{k_2^2 k_{z2} Y_2 (Y_{xx} + Y_{yy}) + k_{z2} Y_2 (k_x^2 Y_{xx} + k_x k_y (Y_{xy} + Y_{yx}) + k_y^2 Y_{yy}) + k_2 k_{z2}^2 (Y_2^2 - \det Y) + k_2^3 (Y_2^2 + \det Y)}. \qquad (4.55)$$

Substituting the derivatives from Appendix F into (4.54) and solving for $\frac{\partial w}{\partial k_y}$ yields the group velocity in the $y$-direction,

$$v_{gy}^{\text{TIS}} = \frac{\partial \omega}{\partial k_y} = \frac{\omega(k_{z2} Y_2 (2 k_y Y_{yy} + k_x (Y_{xy} + Y_{yx})) + k_2 k_y (Y_2^2 + \det Y))}{k_2^2 k_{z2} Y_2 (Y_{xx} + Y_{yy}) + k_{z2} Y_2 (k_x^2 Y_{xx} + k_x k_y (Y_{xy} + Y_{yx}) + k_y^2 Y_{yy}) + k_2 k_{z2}^2 (Y_2^2 - \det Y) + k_2^3 (Y_2^2 + \det Y)}, \qquad (4.56)$$

98
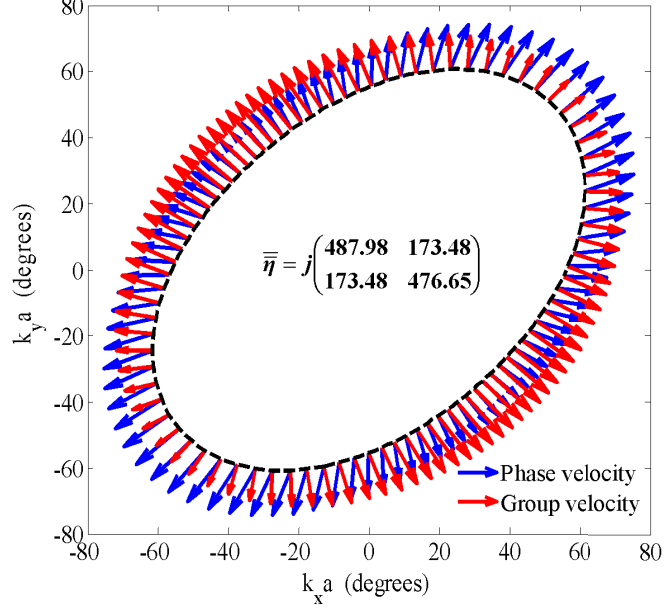
Figure 4.11: Arrows point in the group velocity (red) and phase velocity (blue) directions for an idealized inductive TIS (4.58) at 10 GHz. The group and phase velocities co-align along the principal axes of the surface. The length of the red arrows represent the normalized magnitude of the group velocity. The transverse unit cell dimension is $a = 3$ mm.

The direction of power flow along the TIBC, $\theta_s^{\text{TIBC}}$, is then given by:

$$
\begin{aligned}
\tan \theta_s^{\text{TIBC}} &= \frac{v_{gy}^{\text{TIBC}}}{v_{gx}^{\text{TIBC}}} \\
&= \frac{k_{z2} Y_2 (k_x (Y_{xy} + Y_{yx}) + 2 k_y Y_{yy}) + k_2 k_y (Y_2^2 + \det Y)}{k_{z2} Y_2 (k_y (Y_{xy} + Y_{yx}) + 2 k_x Y_{xx}) + k_2 k_x (Y_2^2 + \det Y)}
\end{aligned}
\tag{4.57}
$$

For a given TIBC, the direction of power flow can be calculated as a function of transverse wave number via (4.57). Fig. 4.11 shows the 10 GHz isofrequency contour for the following TIBC

$$
\overline{\overline{\eta}}_{surf} = j \begin{pmatrix} 487.98 & 173.48 \\ 173.48 & 476.48 \end{pmatrix},
\tag{4.58}
$$

plotted using (4.50). The phase velocity directions (blue arrows) and group velocity

99

directions (red arrows) are overlaid on the isofrequency contour. The direction of the group velocity (direction of power flow) along the surface is calculated from (4.57). The direction of phase velocity along the surface, $\theta_{k_t}$, is given by

$$\tan \theta_{k_t} = \frac{k_y}{k_x}. \tag{4.59}$$

An anisotropic impedance boundary condition is used in a full-wave eigenmode solver (HFSS) to verify the eigenfrequency and directions of power flow for points on the isofrequency contour of Fig. 4.11. Table 4.1 shows good agreement between the direction of power flow calculated analytically using (4.57) and full-wave simulation.

Table 4.1: Full-wave verification of Modal frequency and group velocity direction for TIBC

| Prop. Angle $\theta_{k_t}$ (deg) | phase in $x$ $k_x a$ (deg) | phase in $y$ $k_y a$ (deg) | Analytic freq (GHz) | Sim. freq (GHz) | Analytic $\theta_s^{\text{TIBC}}$ (deg) | Sim. $\theta_s^{\text{TIBC}}$ (deg) |
|---|---|---|---|---|---|---|
| 0 | 56.06 | 0 | 10 | 9.99 | -22.956 | -23.11 |
| 46.13 | 32.25 | $-33.55$ | 10 | 9.99 | -46.01 | -46.00 |
| -136.38 | $-52.30$ | $-49.84$ | 10 | 9.98 | -136.97 | -136.98 |
| 133.37 | $-31.97$ | 33.83 | 10 | 9.99 | 133.80 | 133.81 |
| 89.25 | 0.73 | 55.60 | 10 | 9.99 | 111.92 | 112.04 |
| 45.12 | 50.96 | 51.18 | 10 | 9.98 | 46.52 | 46.54 |

In the next section, (4.53) and (4.54) is used to solve for the group velocity of a PCTIS. For a PCTIS, the $Y_{**}$ terms in (4.53) and (4.54) represent the effective surface impedance, which depends on frequency and the transverse wave numbers ($k_x$ and $k_y$).

### 4.5.2 Direction of power flow along a PCTIS

The effective surface admittance tensor of a PCTIS (see Fig. 4.12), analogous to $Y_{xx}$, $Y_{xy}$, $Y_{yx}$, and $Y_{yy}$ of an idealized surface, is a function of transverse wave number [77]. Even though the surface impedance still relates the ratio of $E_t$ to $H_t$, the direction of power flow along the PCTIS is generally different from that along
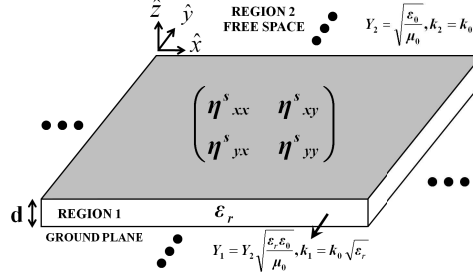
Figure 4.12: PCTIS consisting of a tensor sheet impedance over a grounded dielectric substrate. The tensor sheet impedance/admittance, which models a generalized metallic cladding, is denoted with a superscript 's'.

a TIBC with the same surface impedance. This is due to the presence of spatial dispersion, resulting from the substrate thickness of the PCTIS. As given by (4.45) in Section 4.4 [77], the effective surface admittance of a PCTIS is,

$$
\begin{aligned}
\overline{\overline{Y}}_{surf}(\theta_{k_t}) &= \begin{pmatrix} Y_{xx}(\theta_{k_t}) & Y_{xy}(\theta_{k_t}) \\ Y_{yx}(\theta_{k_t}) & Y_{yy}(\theta_{k_t}) \end{pmatrix} = \begin{pmatrix} Y^s_{xx} & Y^s_{xy} \\ Y^s_{yx} & Y^s_{yy} \end{pmatrix} + \\
R^T(-\theta_{k_t}) &\begin{pmatrix} -j\left(Y_1 \frac{k_1}{k_{z1}}\right)\cot(k_{z1}d) & 0 \\ 0 & -j\left(Y_1 \frac{k_{z1}}{k_1}\right)\cot(k_{z1}d) \end{pmatrix} R(-\theta_{k_t}).
\end{aligned}
\tag{4.60}
$$

where

$$
R(-\theta_{k_t}) = \begin{pmatrix} \cos\theta_{k_t} & \sin\theta_{k_t} \\ -\sin\theta_{k_t} & \cos\theta_{k_t} \end{pmatrix},
\tag{4.61}
$$

and $k_1^2 = k_x^2 + k_y^2 + k_{z1}^2$. The effective surface admittance is equal to the sum of the sheet admittance and the admittance of the grounded dielectric substrate rotated by $-\theta_{k_t}$, where $\theta_{k_t}$ is the direction of propagation along the surface with respect to the $x$-axis. In terms of the wave vector components,

$$\overline{\overline{Y}}_{surf}(\theta_{k_t}) = \begin{pmatrix} Y_{xx}^s & Y_{xy}^s \\ Y_{yx}^s & Y_{yy}^s \end{pmatrix} +$$

$$= \frac{-jY_1 \cot(k_{z1}d)}{k_x^2 + k_y^2} \begin{pmatrix} k_x & -k_y \\ k_y & k_x \end{pmatrix} \begin{pmatrix} \frac{k_1}{k_{z1}} & 0 \\ 0 & \frac{k_{z1}}{k_1} \end{pmatrix} \begin{pmatrix} k_x & k_y \\ -k_y & k_x \end{pmatrix}. \tag{4.62}$$

The elements of the effective surface admittance tensor can therefore be rewritten as:

$$Y_{xx} = Y_{xx}^s - \frac{jY_1 \cot(k_{z1}d)}{k_1 k_{z1}}(k_1^2 - k_y^2) \tag{4.63}$$

$$Y_{xy} = Y_{xy}^s - \frac{jY_1 \cot(k_{z1}d)}{k_1 k_{z1}}(k_x k_y) \tag{4.64}$$

$$Y_{yx} = Y_{yx}^s - \frac{jY_1 \cot(k_{z1}d)}{k_1 k_{z1}}(k_x k_y) \tag{4.65}$$

$$Y_{yy} = Y_{yy}^s - \frac{jY_1 \cot(k_{z1}d)}{k_1 k_{z1}}(k_1^2 - k_x^2) \tag{4.66}$$

Differentiating (4.63)-(4.66) with respect to $k_x$ or $k_y$ yields

$$\begin{aligned}
\frac{\partial}{\partial k_q} Y_{xx} = & \frac{Y_{xx}^s}{\omega}\frac{\partial \omega}{\partial k_q} \\
& - jY_1[\cot(k_{z1}d)(k_1^2 - k_y^2)(\frac{1}{k_1}\frac{\partial F}{\partial k_q} + \frac{1}{k_{z1}}\frac{\partial E}{\partial k_q}) \\
& + \frac{1}{k_1 k_{z1}}(\cot(k_{z1}d)\frac{\partial D}{\partial k_q} + (k_1^2 - k_y^2)\frac{\partial C}{\partial k_q})]
\end{aligned} \tag{4.67}$$

$$\frac{\partial}{\partial k_q} Y_{xy} = \frac{Y^s_{xy}}{\omega} \frac{\partial \omega}{\partial k_q}$$
$$- jY_1 [\cot(k_{z1}d) k_x k_y (\frac{1}{k_1}\frac{\partial F}{\partial k_q} + \frac{1}{k_{z1}}\frac{\partial E}{\partial k_q}) \qquad (4.68)$$
$$+ \frac{1}{k_1 k_{z1}}(\cot(k_{z1}d)\frac{\partial G}{\partial k_q} + k_x k_y \frac{\partial C}{\partial k_q})]$$

$$\frac{\partial}{\partial k_q} Y_{yx} = \frac{Y^s_{yx}}{\omega} \frac{\partial \omega}{\partial k_q}$$
$$- jY_1 [\cot(k_{z1}d) k_x k_y (\frac{1}{k_1}\frac{\partial F}{\partial k_q} + \frac{1}{k_{z1}}\frac{\partial E}{\partial k_q}) \qquad (4.69)$$
$$+ \frac{1}{k_1 k_{z1}}(\cot(k_{z1}d)\frac{\partial G}{\partial k_q} + k_x k_y \frac{\partial C}{\partial k_q})]$$

$$\frac{\partial}{\partial k_q} Y_{yy} = \frac{Y^s_{yy}}{\omega} \frac{\partial \omega}{\partial k_q}$$
$$- jY_1 [\cot(k_{z1}d)(k_1^2 - k_x^2)(\frac{1}{k_1}\frac{\partial F}{\partial k_q} + \frac{1}{k_{z1}}\frac{\partial E}{\partial k_q}) \qquad (4.70)$$
$$+ \frac{1}{k_1 k_{z1}}(\cot(k_{z1}d)\frac{\partial J}{\partial k_q} + (k_1^2 - k_y^2)\frac{\partial C}{\partial k_q})]$$

where $q = x$ or $y$, and the derivatives of $C$, $D$, $E$, $F$, $G$, and $J$ are given in Appendix F. The group velocity of a PCTIS is found by substituting (4.63)-(4.70) into the expressions for an idealized TIBC (4.53)-(4.54), and then solving for $\frac{\partial \omega}{\partial k_x}$ and $\frac{\partial \omega}{\partial k_y}$. The $x$ and $y$ components of the group velocity for a PCTIS can be expressed compactly as:

$$v^{\text{PCTIS}}_{gq} = \frac{\partial \omega}{\partial k_q}$$
$$= \frac{-B_7 + \frac{k_q}{k_{z2}}B_4 - \xi_1 B_1 + \xi_2(B_2 + B_6) - \xi_4 B_3}{\chi_1 B_1 - \chi_2 B_2 - \chi_3 B_6 + \chi_4 B_3 + \nu B_4 + \zeta B_5} \qquad (4.71)$$

where

$$q = x \text{ or } y, r = \begin{cases} y \text{ if } q = x \\ x \text{ if } q = y \end{cases}. \tag{4.72}$$

and $B_n$, $\chi$, $\zeta$, $\nu$ and $\xi$ terms are given in Table F.2 in Appendix F. It should be noted that the expressions for the group velocity along a TIBC can also be found from (4.71) by using the appropriate terms from Table F.1. The direction of power flow for a PCTIS is given by

$$\tan \theta_s^{\text{PCTIS}} = \frac{v_{gy}^{\text{PCTIS}}}{v_{gx}^{\text{PCTIS}}}. \tag{4.73}$$

Fig. 4.13 shows the phase velocity and group velocity directions, overlaid onto a 10 GHz isofrequency contour, for a specific PCTIS. The PCTIS consists of a capacitive sheet impedance,

$$\overline{\overline{\eta}}^s = -j \begin{pmatrix} 382.58 & 65.00 \\ 65.00 & 157.42 \end{pmatrix}, \tag{4.74}$$

over a grounded dielectric substrate ($d = 1.27$ mm, $\epsilon_r = 10.2$). Close agreement between the direction of power flow calculated analytically using (4.73) and full-wave simulation is shown in Table II.

Table 4.2: Full-wave verification of Modal frequency and group velocity direction for PCTIS

| Prop. Angle $\theta_{k_t}$ (deg) | phase in $x$ $k_x a$ (deg) | phase in $y$ $k_y a$ (deg) | Analytic freq (GHz) | Sim. freq (GHz) | Analytic $\theta_s^{\text{PCTIS}}$ (deg) | Sim. $\theta_s^{\text{PCTIS}}$ (deg) |
|---|---|---|---|---|---|---|
| 0 | 40.06 | 0 | 10 | 10.00 | 9.99 | 9.88 |
| -75 | 13.05 | $-48.69$ | 10 | 10.01 | -75.00 | -75.00 |
| -45 | 30.05 | 30.05 | 10 | 10.00 | 30.58 | 30.66 |
| 15 | 37.76 | 10.17 | 10 | 10.00 | 15.00 | 15.01 |
| 159 | $-40.77$ | 15.65 | 10 | 10.00 | 173.69 | 173.61 |
| -111 | $-16.89$ | $-44.01$ | 10 | 10.00 | -122.81 | -122.75 |

In this section, expressions for the group velocity (4.55)-(4.56) and the direction of
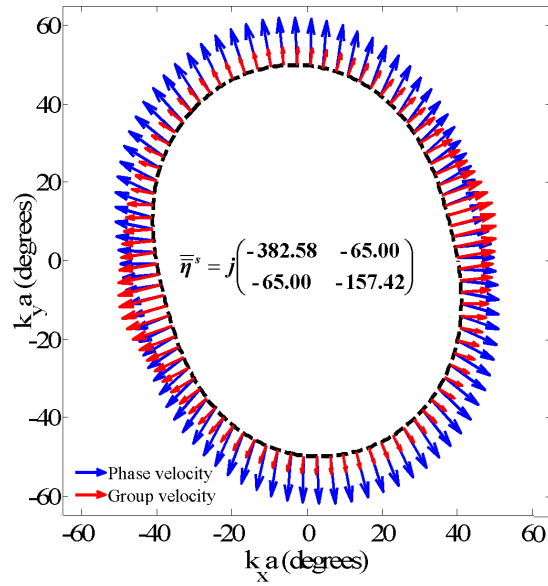
Figure 4.13: Arrows point in the group velocity (red) and phase velocity (blue) directions for an idealized PCTIS consisting of a capacitive sheet (4.74) over a grounded dielectric substrate at 10 GHz. The substrate thickness is 1.27 mm and the dielectric constant is $\epsilon_r = 10.2$. The group and phase velocities co-align along the principal axes of the surface. The length of the red arrows represent the normalized magnitude of the group velocity. The transverse unit cell dimension is $a = 3$ mm.

power flow (4.57) along an idealized TIBC were found. Additionally, expressions for the group velocity and the direction of power flow, that account for spatial dispersion, were found for a PCTIS. The direction of power flow along the TIBC and the PCTIS was verified using a commercial full-wave solver. These expressions provide a valuable tool toward the design of inhomogeneous anisotropic surfaces that support arbitrary wave vector and power flow distributions (Chapter V).

## 4.6 Thin PCTISs

In general, (4.45) and Fig. 4.8 show that a PCTIS cannot be approximated by an idealized TIBC. However, under certain conditions, it may be possible to lump the patterned metallic cladding and the grounded dielectric substrate together and treat it as a single surface.

A high dielectric constant ($\epsilon_{r1} \gg 1$) ensures that the normal wave number, $k_{z1}$, approaches $k_1$ (wave number in the dielectric of the PCTIS) due to the phase matching condition at the interface between regions 1 and 2 [51, 78]. In other words, propagation in the dielectric is nearly normal ($\frac{k_{z1}}{k_1} \approx 1$). Making this approximation in (4.45) yields:

$$\overline{\overline{Y}}_{surf}(\theta) = \begin{pmatrix} Y^s_{xx} & Y^s_{xy} \\ Y^s_{yx} & Y^s_{yy} \end{pmatrix} + R^T(-\theta) \begin{pmatrix} -jY_1 \cot(k_1 d) & 0 \\ 0 & -jY_1 \cot(k_1 d) \end{pmatrix} R(\theta).$$

(4.75)

Notice that the second term is unaffected by rotation since it is isotropic. Therefore, the effective surface impedance becomes

$$\overline{\overline{Y}}_{surf} = \begin{pmatrix} Y^s_{xx} & Y^s_{xy} \\ Y^s_{yx} & Y^s_{yy} \end{pmatrix} + \begin{pmatrix} -jY_1 \cot(k_1 d) & 0 \\ 0 & -jY_1 \cot(k_1 d) \end{pmatrix}$$

(4.76)

and the surface impedance is no longer $\theta$ dependent. Making the additional assumption that the structure is electrically thin, $(k_1 d << 1)$ yields,

$$\overline{\overline{Y}}_{surf} = \begin{pmatrix} Y_{xx}^s & Y_{xy}^s \\ Y_{yx}^s & Y_{yy}^s \end{pmatrix} + \begin{pmatrix} \frac{1}{j\eta_1 k_1 d} & 0 \\ 0 & \frac{1}{j\eta_1 k_1 d} \end{pmatrix}. \tag{4.77}$$

In this limit, the ground plane and dielectric substrate effectively act as an inductor and the PCTIS can be lumped. In the case of a purely capacitive sheet (e.g. the sheet from Fig. 4.6), the surface admittance is given by

$$\begin{aligned} \overline{\overline{Y}}_{surf} &= \begin{pmatrix} j\omega C_{xx}^s & j\omega C_{xy}^s \\ j\omega C_{yx}^s & j\omega C_{yy}^s \end{pmatrix} + \begin{pmatrix} \frac{1}{j\omega(\mu_1 d)} & 0 \\ 0 & \frac{1}{j\omega(\mu_1 d)} \end{pmatrix} \\ &= \begin{pmatrix} j\omega C_{xx}^s + \frac{1}{j\omega L_0} & j\omega C_{xy}^s \\ j\omega C_{yx}^s & j\omega C_{yy}^s + \frac{1}{j\omega L_0} \end{pmatrix}, \end{aligned} \tag{4.78}$$

where $L_0 = \mu_1 d$. The surface impedance becomes independent of $\epsilon_{r1}$. In fact, (4.78) suggests a PCTIS can be treated as a single TIBC when it possesses an electrically-thin substrate $(k_1 d << 1)$ of high dielectric constant $(k_{z1}/k_1 \approx 1)$. To test this hypothesis, two separate cases are considered: Case A, where the inductive surface impedance is low, and Case B where the inductive surface impedance is high.

### 4.6.1 Low surface impedance values

First, we examine a PCTIS with a low surface impedance. The sheet impedance and physical thickness of the PCTIS remains fixed and variations of dielectric constant are explored. The sheet impedance is set equal to (4.46) at 10 GHz, resulting in a sheet capacitance of: $C_{xx}^s = 188.22$ fF, $C_{xy}^s = C_{yx}^s = -50.85$ fF, and $C_{yy}^s = 104.01$ fF. The substrate thickness is chosen to be $d = 0.27386$ mm, such that it remains electrically thin for all three values of permittivity considered: $\epsilon_{r1} = 2.2$, 10.2, and
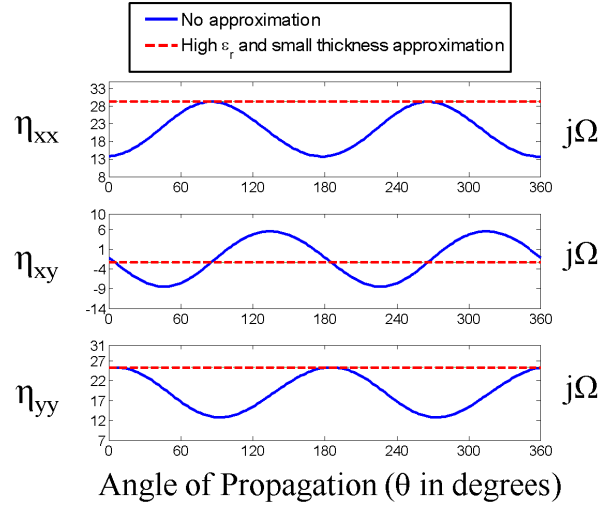
(a) $\epsilon_{r1} = 2.2$, $d = \lambda_d/73.9$.
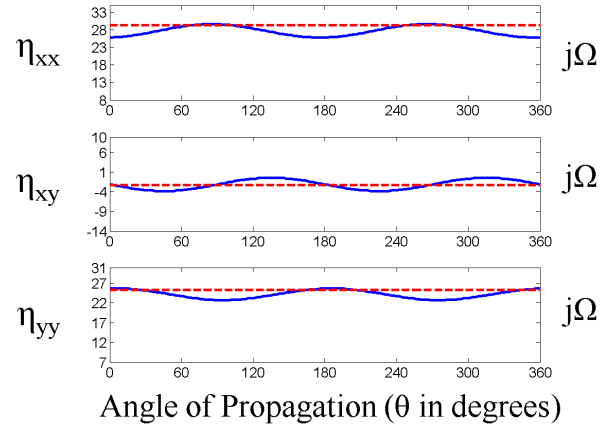


(b) $\epsilon_{r1} = 10.2$, $d = \lambda_d/34.3$.
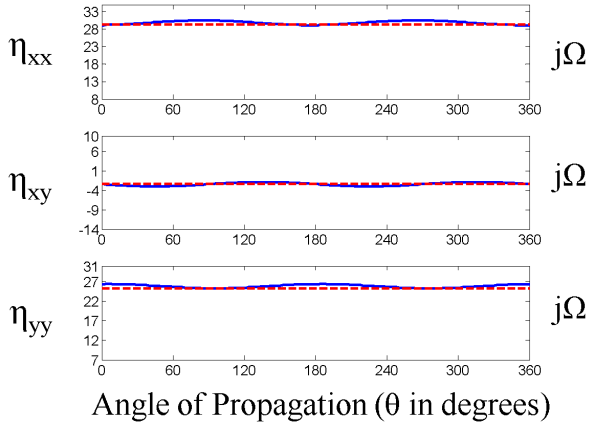


(c) $\epsilon_{r1} = 30$, $d = \lambda_d/20$.

Figure 4.14: Angle-dependent (solid lines) and angle-independent (dashed lines) tensor surface impedance for a fixed tensor sheet over a grounded dielectric substrate at 10 GHz. The sheet parameters are given by: $C_{xx}^s = 188.22$ fF, $C_{xy}^s = C_{yx}^s = -50.85$ fF, and $C_{yy}^s = 104.01$ fF, and $L_0 = \mu_1 d$. The substrate thickness is $d = 0.27386$ mm.

30. Since the lumped (angle-independent) surface impedance (4.78) does not depend on $\epsilon_{r1}$, it remains invariant for all three dielectric constants. This angle-independent impedance, given by

$$\bar{\bar{\eta}}_{surf} = j \begin{pmatrix} 29.27 & -2.355 \\ -2.355 & 25.37 \end{pmatrix} \Omega \tag{4.79}$$

at 10 GHz, is shown with dashed lines in Fig. 4.14. Figs. 4.14(a), 4.14(b), and 4.14(c) compare the angle-dependent surface impedance (4.45) to this lumped surface impedance (4.79), for dielectric constants of $\epsilon_{r1} = 2.2$, 10.2, and 30 respectively. It is clear that, with increasing dielectric constant, the surface impedance of the PCTIS becomes nearly independent of $\theta$, and approaches the lumped surface impedance given by (4.79). Therefore, a PCTIS with a low surface impedance can be treated as a single, angle-independent TIBC under the conditions of high $\epsilon_{r1}$ and $k_1 d << 1$.

### 4.6.2 High surface impedance values

Now, we consider a PCTIS with a higher (on the order of 100 $j\Omega$) surface impedance. The surface impedance of a practical/useful PCTIS must be of this order to support dispersion curves that differ appreciably from those of free space [11, 22, 47]. For an inductive surface, a low surface impedance results in a loosely bound surface wave with circular dispersion curves and wave number approaching that of free space.

As before, the sheet impedance and physical thickness of the substrate are fixed and the dielectric constant is varied ($\epsilon_{r1} = 2.2$, and 30). The physical thickness of the substrate is set to $d = 0.152$ mm and the sheet capacitance to: $C_{xx}^s = 1.1277$ pF, $C_{xy}^s = C_{yx}^s = -67.97$ fF, and $C_{yy}^s = 1.2402$ pF. These parameters are chosen to establish a higher surface impedance value than in Case A. Again, the lumped
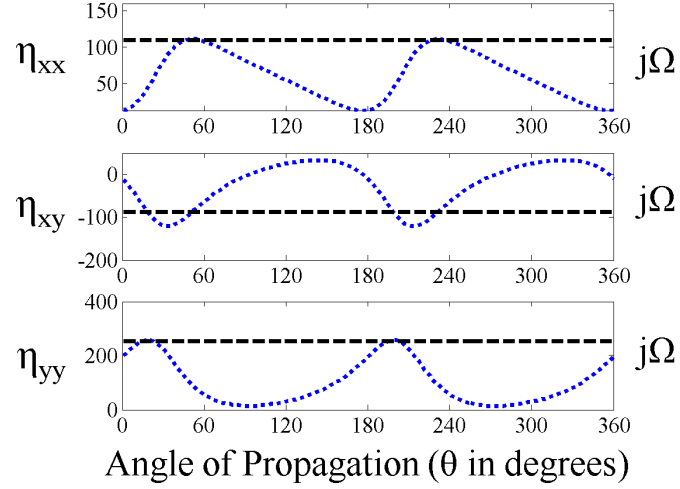
(a) $\epsilon_{r1} = 2.2$, $d = \lambda_d/132.9$.
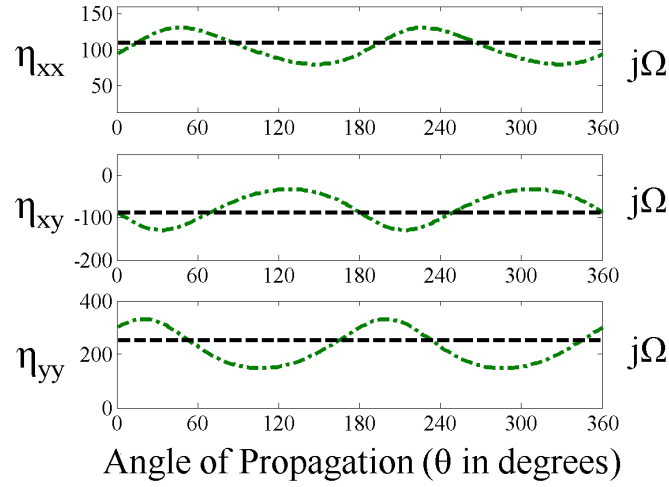


(b) $\epsilon_{r1} = 30$, $d = \lambda_d/36$.

Figure 4.15: Angle-dependent (dotted and dash-dot lines) and angle-independent (dashed lines) surface impedance for a fixed tensor sheet over a grounded dielectric substrate at 10 GHz. The sheet parameters are given by: $C_{xx}^s = 1.1277$ pF, $C_{xy}^s = C_{yx}^s = -67.97$ fF, $C_{yy}^s = 1.2402$ pF, and $L_0 = \mu_1 d$. The substrate thickness is $d = 0.152$ mm.

(angle-independent) surface impedance (4.78) does not depend on $\epsilon_{r1}$. It is equal to

$$\overline{\overline{\eta}}_{surf} = j \begin{pmatrix} 110 & -87 \\ -87 & 254 \end{pmatrix} \Omega \tag{4.80}$$

at 10 GHz and shown with dashed lines in Fig.4.15. Figs. 4.15(a), and 4.15(b) compare the angle-dependent surface impedance (4.45) to the lumped surface impedance (4.80), for dielectric constants of $\epsilon_{r1} = 2.2$, and 30, respectively. The structure remains electrically thin for both variants of dielectric constant. However, in contrast to Case A, the angle-dependent surface impedance (4.45) does not converge to the lumped (angle-independent) surface impedance (4.80) with increasing dielectric constant. This may seem unexpected, but there is a simple explanation for this. The higher surface impedance of Case B is achieved by operating close to the resonance of the capacitive sheet and the grounded dielectric substrate. Therefore, even small changes in $k_{z1}$ resulting from changes in propagation angle $\theta$ can cause fairly large changes in surface impedance. As a result, the angle dependence of the PCTIS's surface impedance does not vanish with increasing dielectric constant. In summary, the angle dependence of the surface impedance tensor persists for high values of dielectric constant, for PCTISs with practical values of surface impedance. We have shown that a PCTIS with a high dielectric constant and small electrical thickness can be modeled as a single surface impedance tensor with reasonable accuracy for the case of low surface impedance. For surfaces possessing a higher surface impedance, the lumped surface approximation may be adequate for approximate designs at a specified frequency of operation. However, if accurate propagation characteristics are desired, (4.45) should be used to determine the surface impedance as a function of propagation angle along the surface.

## 4.7    Chapter Summary

In this chapter, a modified transverse resonance technique for TISs was introduced. First, it was used to derive the surface admittance of a printed-circuit scalar impedance surface, consisting of a scalar admittance sheet over a grounded dielectric substrate. Then, it was used to derive the dispersion equation for an idealized TIBC. These results were combined to derive the dispersion equation for a PCTIS, which consists of a tensor sheet impedance (representing a patterned metallic cladding) over a grounded dielectric substrate. The angle-dependent effective surface impedance of the PCTIS was derived and verified. This angle dependence is equivalent to a dependence on transverse wave number. Therefore, the surface impedance of the PCTIS exhibits spatial dispersion. It was shown, that in general, a PCTIS cannot be modeled as an idealized TIBC that is independent of propagation angle. However, the PCTIS can be modeled with a TIBC when the angle-dependent effective surface impedance tensor is used. Expressions for the group velocity and the direction of power flow along a TIBC and a PCTIS are found. This chapter also discusses electrically-thin PCTISs, showing that even these PCTISs can only be approximately modeled with angle-independent surface impedance tensors. If accurate propagation characteristics are desired, the angle-dependent effective tensor surface impedance of the PCTIS must be used. Antenna designs and cloaking applications often assume an incident plane wave at a specified angle. When implementing such devices with PCTISs, the impedance sheet needs to be designed with the angle dependence of (4.45) in mind, in order for the structure to have the desired surface impedance along a specified direction. The modified transverse resonance technique presented in this chapter can be extended to handle multi-layer surfaces in a straightforward manner.

Up to this point, various aspects of TIBCs and PCTISs have been analyzed. Their dispersion equations were derived using two methods: field analysis (Chapter III), and the more intuitive modified transverse resonance technique (this chapter). The

dispersion equation of a PCTIS was directly related to the dispersion equation of a TIBC via the angle-dependent effective surface impedance of the PCTIS. Their group velocity expressions were also derived. In the next chapter, a method for designing transformation electromagnetics devices using TIBCs and PCTISs is presented. This method, which combines all the aforementioned analysis, allows the design of TIBCs and PCTISs that support prescribed wave vector and Poynting vector distributions along the surface.

# CHAPTER V

# Transformation Electromagnetics Devices Based on Printed-Circuit Tensor Impedance Surfaces

## 5.1 Introduction

Transformation electromagnetics was first introduced in 2006 [33]. Since that time, transformation electromagnetics methods have been applied to the design of novel microwave and optical devices such as cloaks, polarization splitters, and beam-benders [33, 34, 39]. Transformation electromagnetics allows a field distribution to be transformed from an initial configuration to a desired one through a change of material parameters via a coordinate transformation. In addition to volumetric designs, planar transformation-based devices using transmission-line networks have been recently introduced in [36], and subsequently pursued by other groups [35, 38, 79, 80, 81]. As mentioned in previous chapters, great strides have been made in realizing practical printed devices such as holographic antennas, polarization controlling surfaces, and surface-wave guiding surfaces using the anisotropic properties of tensor impedance surfaces (TISs) [11, 16, 17, 18, 20, 22, 82]. In this chapter, a method for designing transformation electromagnetics devices using TISs is presented.

We first present a method to implement transformation electromagnetics devices using an idealized tensor impedance boundary condition (TIBC) [10, 11]. Later in

the chapter, the method is adapted for practical printed-circuit tensor impedance surfaces (PCTISs) [53, 54, 55, 77]. The TIBC is given by: $\bar{E}_t = \bar{\bar{\eta}}_{surf}\hat{n} \times \bar{H}_t$, where $\bar{E}_t$ and $\bar{H}_t$ are components of the total electric and magnetic field tangential to the surface (at $z = 0$)[10]. This boundary condition can be represented in matrix form as

$$\begin{pmatrix} E_x \\ E_y \end{pmatrix} = \bar{\bar{\eta}}_{surf} \begin{pmatrix} -H_y \\ H_x \end{pmatrix} = \begin{pmatrix} \eta_{xx} & \eta_{xy} \\ \eta_{yx} & \eta_{yy} \end{pmatrix} \begin{pmatrix} -H_y \\ H_x \end{pmatrix}, \tag{5.1}$$

or in terms of admittances,

$$\begin{pmatrix} -H_y \\ H_x \end{pmatrix} = \bar{\bar{Y}}_{surf} \begin{pmatrix} E_x \\ E_y \end{pmatrix} = \begin{pmatrix} Y_{xx} & Y_{xy} \\ Y_{yx} & Y_{yy} \end{pmatrix} \begin{pmatrix} E_x \\ E_y \end{pmatrix}, \tag{5.2}$$

where

$$\bar{\bar{Y}}_{surf} = \bar{\bar{\eta}}_{surf}^{-1} \tag{5.3}$$

A TIS can support $TM$ (Fig. 5.1(a)), $TE$ (Fig. 5.1(b)), or hybrid modes. Recently, a surface impedance cloak was designed [40] using the $TM$ index profile, characteristic of beam-shifters [83]. In the present work, the surface impedance profile needed to implement transformation electromagnetics devices is found from the transformed wave vector and Poynting vector distributions along a surface [76, 84]. Specifically, surface impedance profiles are found that support modes ($TM$, $TE$, or hybrid) with these transformed phase and power characteristics. The method ensures that only the surface impedance entries need to be designed, and the free space above the TIS need not be transformed. The method is later adapted to design practical PCTISs that support modes with transformed wave vector and Poynting vector distributions. A PCTIS is a practical realization of a TIBC (as explained in Chapter III. When designing PCTISs, the tensor sheet impedance entries are the unknowns: the quantities of interest.

In the next section of this chapter, transformation electromagnetics in two dimensions (2D) is reviewed. Section 5.3 outlines an approach for designing 2D transformation electromagnetics devices using TIBCs. In Section 5.4, a beam-shifting device is designed and simulated with a commercial full-wave solver to verify the design method outlined in Section 5.3. In Section 5.5, transformation electromagnetics is applied to PCTISs and a beam-shifter is designed using a PCTIS in Section 5.6. The proposed design methodology is a step towards the realization of practical, transformation electromagnetics-based devices realized using PCTISs [11, 53].
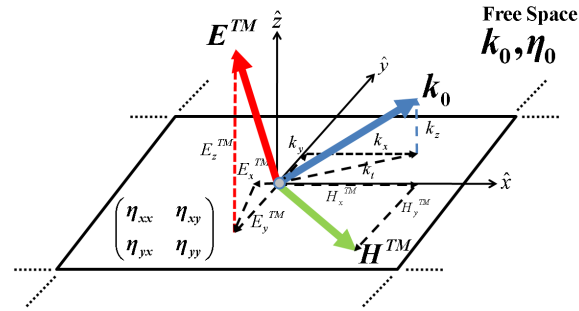


(a) TIS supporting a $TM$ wave.
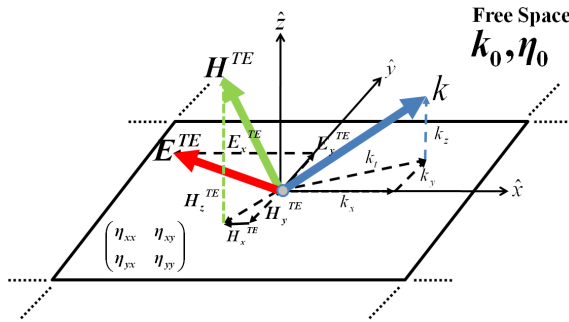


(b) TIS supporting a $TE$ wave.

Figure 5.1: Waves interacting with a tensor impedance surface (TIS). In general, tensor impedance surfaces can support both $TM$, $TE$, and hybrid modes. The $TM$ wave has an $E_z$ component and the $TE$ wave has an $H_z$ component.

## 5.2 Two-Dimensional Transformations

In transformation electromagnetics [33], fields are transformed from an initial state to a desired one via a change in material parameters based on a coordinate transformation. The transformed material tensors ($\overline{\overline{\mu''}}$ and $\overline{\overline{\epsilon''}}$) are related to the initial material parameters ($\overline{\overline{\mu}}$ and $\overline{\overline{\epsilon}}$) in the following manner:

$$\overline{\overline{\mu''}} = \frac{\overline{\overline{J}}\,\overline{\overline{\mu}}\,(\overline{\overline{J}})^T}{|\overline{\overline{J}}|} \qquad \overline{\overline{\epsilon''}} = \frac{\overline{\overline{J}}\,\overline{\overline{\epsilon}}\,(\overline{\overline{J}})^T}{|\overline{\overline{J}}|}, \qquad (5.4)$$

where

$$\overline{\overline{J}} = \begin{pmatrix} \frac{\partial x''}{\partial x} & \frac{\partial x''}{\partial y} & \frac{\partial x''}{\partial z} \\ \frac{\partial y''}{\partial x} & \frac{\partial y''}{\partial y} & \frac{\partial y''}{\partial z} \\ \frac{\partial z''}{\partial x} & \frac{\partial z''}{\partial y} & \frac{\partial z''}{\partial z} \end{pmatrix}, \qquad (5.5)$$

is the Jacobian of the transformation from the $(x, y, z)$ coordinate system to the $(x'', y'', z'')$ system. When two-dimensional transformations are applied in the $x - y$ plane, the Jacobian reduces to

$$\overline{\overline{J}} = \begin{pmatrix} \frac{\partial x''}{\partial x} & \frac{\partial x''}{\partial y} \\ \frac{\partial y''}{\partial x} & \frac{\partial y''}{\partial y} \end{pmatrix} = \begin{pmatrix} J_{11} & J_{12} \\ J_{21} & J_{22} \end{pmatrix}. \qquad (5.6)$$

In transformation electromagnetics, material parameters transform as in (5.4). However, when designing TISs, the surface impedance/admittance is the quantity of interest rather than material parameters. Therefore, we must find how the surface admittance transforms. Transformation electromagnetics dictates that the transformed fields are related to the initial fields as [34, 85]:

$$\overline{E} = \overline{\overline{J}}^T \overline{E''}, \qquad (5.7)$$

$$\overline{H} = \overline{\overline{J}}^T \overline{H}''$$  (5.8)

or equivalently,

$$\begin{pmatrix} E_x \\ E_y \end{pmatrix} = \begin{pmatrix} J_{11} & J_{21} \\ J_{12} & J_{22} \end{pmatrix} \begin{pmatrix} E_x'' \\ E_y'' \end{pmatrix},$$  (5.9)

$$\begin{pmatrix} H_x \\ H_y \end{pmatrix} = \begin{pmatrix} J_{11} & J_{21} \\ J_{12} & J_{22} \end{pmatrix} \begin{pmatrix} H_x'' \\ H_y'' \end{pmatrix}.$$  (5.10)

Rearranging the magnetic field components in (5.10), yields

$$\begin{pmatrix} -H_y \\ H_x \end{pmatrix} = \begin{pmatrix} J_{22} & -J_{12} \\ -J_{21} & J_{11} \end{pmatrix} \begin{pmatrix} -H_y'' \\ H_x'' \end{pmatrix} = |\overline{\overline{J}}|\overline{\overline{J}}^{-1} \begin{pmatrix} -H_y'' \\ H_x'' \end{pmatrix}.$$  (5.11)

Substituting (5.9) and (5.11) into the tensor admittance boundary condition (5.2) yields

$$\begin{pmatrix} -H_y'' \\ H_x'' \end{pmatrix} = \overline{\overline{Y}}''_{surf} \begin{pmatrix} E_x'' \\ E_y'' \end{pmatrix} = \frac{\overline{\overline{J}}\overline{\overline{Y}}_{surf}\overline{\overline{J}}^T}{|\overline{\overline{J}}|} \begin{pmatrix} E_x'' \\ E_y'' \end{pmatrix}.$$  (5.12)

Comparing equations (5.2) and (5.12) reveals that the traditional transformation electromagnetics method transforms the surface admittance in the same manner that $\overline{\overline{\epsilon}}$ and $\overline{\overline{\mu}}$ are transformed in (5.4).

The transverse resonance equation that determines the guided modes, for propagation along the x-axis of an idealized TIBC is given by (4.20):

$$\begin{pmatrix} Y_{xx} & Y_{xy} \\ Y_{yx} & Y_{yy} \end{pmatrix} \begin{pmatrix} E_x \\ E_y \end{pmatrix} = \begin{pmatrix} Y_0 \frac{k_0}{k_z} & 0 \\ 0 & Y_o \frac{k_z}{k_0} \end{pmatrix} \begin{pmatrix} E_x \\ E_y \end{pmatrix},$$  (5.13)

118

where $Y_0 = \sqrt{\frac{\epsilon_0}{\mu_0}}$, and $k_0 = k_t^2 + k_z^2$. In general, the transverse wave number, $k_t$, is given by $k_t^2 = k_x^2 + k_y^2$ but in this particular case, $k_t = k_x$. The matrix on the right-hand-side (RHS) of (5.13) contains the $TM$ and $TE$ admittances of free space. Manipulating both sides of (5.13) yields

$$\left[ \frac{\overline{\overline{J}}}{|\overline{\overline{J}}|} \begin{pmatrix} Y_{xx} & Y_{xy} \\ Y_{yx} & Y_{yy} \end{pmatrix} \overline{\overline{J}}^T \right] \left( \left( \overline{\overline{J}}^T \right)^{-1} \begin{pmatrix} E_x \\ E_y \end{pmatrix} \right)$$
$$= \frac{\overline{\overline{J}}}{|\overline{\overline{J}}|} \begin{pmatrix} Y_o \frac{k_o}{k_z} & 0 \\ 0 & Y_o \frac{k_z}{k_o} \end{pmatrix} \overline{\overline{J}}^T \left( \left( \overline{\overline{J}}^T \right)^{-1} \begin{pmatrix} E_x \\ E_y \end{pmatrix} \right).$$

(5.14)

The term in square brackets on the LHS of (5.14) can be substituted with (5.12), yielding the following equation,

$$\begin{pmatrix} Y_{xx}'' & Y_{xy}'' \\ Y_{yx}'' & Y_{yy}'' \end{pmatrix} \begin{pmatrix} E_x'' \\ E_y'' \end{pmatrix} = \left[ \frac{\overline{\overline{J}}}{|\overline{\overline{J}}|} \begin{pmatrix} Y_o \frac{k_o}{k_z} & 0 \\ 0 & Y_o \frac{k_z}{k_o} \end{pmatrix} \overline{\overline{J}}^T \right] \begin{pmatrix} E_x'' \\ E_y'' \end{pmatrix}.$$

(5.15)

Therefore, not only does the surface admittance, $\overline{\overline{Y}}_{surf}$, have to be transformed but so does the free space above the surface (term in square brackets of (5.15)), if the guidance condition is to be satisfied. This is impractical, since in many applications the space above the impedance surface is fixed. This conclusion is verified through full-wave simulation in Section 5.4.

## 5.3 Transformation Electromagnetics Applied to an Idealized Tensor Impedance Boundary Condition (TIBC)

In the previous section, it was shown that the transformed surface admittance $(\overline{\overline{Y}}_{surf}'')$ can be found from an initial surface impedance $(\overline{\overline{Y}}_{surf})$ in the same manner

119
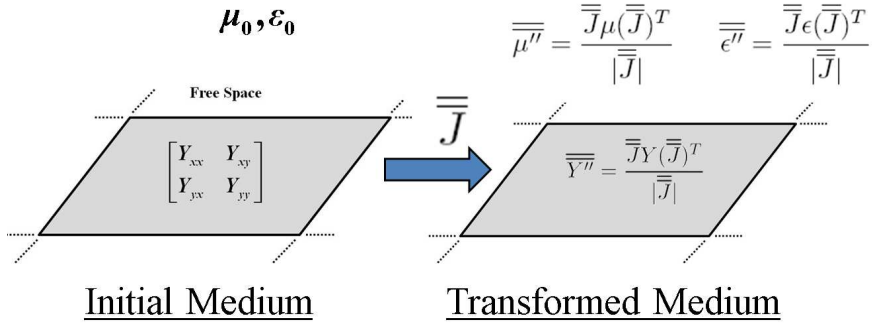
Figure 5.2: Transforming the surface via the traditional transformation electromagnetics method (5.12) results in a transformation of all space. An alternate method that does not transform the space above the surface, but rather the TIBC alone is presented in Section 5.3.

that the transformed material parameters are computed. However, to maintain the guidance condition, the free space above the surface must also be transformed. This section proposes an alternative design approach. In this alternative approach, tensor impedance entries ($\eta''_{xx}, \eta''_{xy} = \eta''_{yy}$, and $\eta''_{yy}$) are found that support the spatially varying wave vector and Poynting vector of the transformation electromagnetics device, while maintaining free space above the surface.

The wave vector and Poynting vector tangential to the surface transform as [75]:

$$\overline{k''_t} = \begin{pmatrix} k''_x \\ k''_y \end{pmatrix} = (J^T)^{-1}\overline{k_t},$$

(5.16)

$$\overline{S''_t} = \begin{pmatrix} S''_x \\ S''_y \end{pmatrix} = (\frac{J}{|J|})\overline{S_t}.$$

(5.17)

At a given spatial coordinate, the Poynting vector points at an angle, $\theta''_{power}$, with respect to the x-axis,

$$\frac{S''_y}{S''_x} = \tan(\theta''_{power}) = b.$$

(5.18)

Similarly, the transformed wave vector points at an angle, $\theta''_{k_t} = k''_y/k''_x$ with respect to the $x$-axis. In addition to supporting the transformed wave vector and Poynting

120

vector, the tensor impedance entries of interest ($\eta''_{xx}$, $\eta''_{xy} = \eta''_{yy}$, and $\eta''_{yy}$) must also satisfy the guidance condition for propagation along the surface.

## 5.3.1 Propagation along TIBCs

The following eigenvalue equation ((3.5) in Chapter III) can be written to find the modes supported by a TIBC [53]:

$$\begin{pmatrix} b_{11} & b_{12} \\ b_{21} & b_{22} \end{pmatrix} \begin{pmatrix} E''_z \\ H''_z \end{pmatrix} = 0, \tag{5.19}$$

where

$$\begin{aligned}
b_{11} &= k''_x k''_z + \frac{k''_x k_0 \eta''_{xx}}{\eta_0} + \frac{k''_y k_0 \eta''_{xy}}{\eta_0} \\
b_{12} &= k_0 k''_y \eta_0 + k''_y k''_z \eta''_{xx} - k''_x k''_z \eta''_{xy} \\
b_{21} &= k''_y k''_z + \frac{k''_x k_0 \eta''_{yx}}{\eta_0} + \frac{k''_y k_0 \eta''_{yy}}{\eta_0} \\
b_{22} &= -k_0 k''_x \eta_0 + k''_y k''_z \eta''_{yx} - k''_x k''_z \eta''_{yy}.
\end{aligned} \tag{5.20}$$

The eigenvalue equation above is found by expressing the tangential field components ($E''_x$, $E''_y$, $H''_x$, and $H''_y$) in terms of the normal components $E''_z$ and $H''_z$ corresponding to $TM$ and $TE$ fields, respectively (see (3.1) and (3.2) in Chapter III). It should be noted that the double primes denote field quantities corresponding to the transformed wave vector (5.16) and Poynting vector (5.17), not the transformed fields ((5.7), (5.8)) from transformation electromagnetics. From (5.19), the dispersion equation of a TIBC ((3.7) in Chapter III) can be derived [10, 53]:

$$b_{11}b_{22} - b_{12}b_{21} = 0, \tag{5.21}$$

and the direction of power flow along a TIBC (4.57):

$$\tan \theta''_{power} =$$
$$\frac{k''_z Y_0(k''_x(Y''_{xy} + Y''_{yx}) + 2k''_y Y''_{yy}) + k_0 k''_y(Y_0^2 + \det Y''_{surf})}{k''_z Y_2(k''_y(Y''_{xy} + Y''_{yx}) + 2k''_x Y''_{xx}) + k_0 k''_x(Y_0^2 + \det Y''_{surf})}, \qquad (5.22)$$

can be found as shown in Chapter IV [74]. The eigenvalue equation (5.19) will be used to design TIBCs that support surface waves with the transformed wave vector and Poynting vector distributions given by (5.16) and (5.17).

### 5.3.2 Design Approach

In transformation electromagnetics, the transformed material parameters are derived from an initial medium. This initial medium is typically free space. Since the intent here is to apply transformation electromagnetics to TIBCs, an initial isotropic surface impedance,

$$\overline{\overline{\eta}}_{surf} = \begin{pmatrix} \eta & 0 \\ 0 & \eta \end{pmatrix}, \qquad (5.23)$$

in free space is chosen that supports a surface wave at a desired frequency of operation. The surface impedance supporting a $TM$ surface wave is given by

$$\eta = \eta_0 \sqrt{1 - \left(\frac{k_t}{k_0}\right)^2}, \qquad (5.24)$$

The tangential wave number $(k_t)$ along the surface is chosen to be greater than that of free space $(k_t > k_0)$ to ensure a bound surface wave. Next, a surface impedance,

$$\overline{\overline{\eta}}''_{surf} = \begin{pmatrix} \eta''_{xx} & \eta''_{xy} \\ \eta''_{yx} & \eta''_{yy} \end{pmatrix}, \qquad (5.25)$$

is found which supports the transformed wave vector and Poynting vector distributions on the surface. By writing the Poynting vector components $(S''_x, S''_y)$ in terms of $E''_z$ and $H''_z$, (5.18) can be recast as

$$\frac{E''_z}{H''_z} = \frac{\eta_0(k''_x + bk''_y)k''_z}{k_0(bk''_x - k''_y)} \pm \frac{j\sqrt{\eta_0^2(-k_0^2(-bk''_x + k''_y)^2 - (k''_x + bk''_y)^2 k''^2_z)}}{k_0(bk''_x - k''_y)}. \tag{5.26}$$

Therefore, the transformed wave vector $(k''_x, k''_y)$ and direction of the Poynting vector $(b = \tan(\theta''_{power}))$ on the surface, uniquely defines the ratio of the normal electric and magnetic fields (ratio of $TM$ to $TE$ fields) supported by the TIBC. Even though the isotropic medium supports a $TM$ wave only, the anisotropic region can support a mixture of $TM$ and $TE$ waves, as indicated by (5.26). Substituting (5.26) into (5.19) yields two equations for finding the surface impedance entries: $\eta''_{xx}, \eta''_{xy} = \eta''_{yx}$, and $\eta''_{yy}$. Setting the determinant of the transformed surface impedance tensor equal to the square of the initial surface impedance $(\eta)$, results in a third equation,

$$\eta''_{xx}\eta''_{yy} - \eta''_{xy}\eta''_{yx} = \eta^2, \tag{5.27}$$

The transformed surface impedance entries can now be found using these three equations. This condition on the determinant of the surface impedance is analogous to the condition on the permittivity and permeability tensors in transformation electromagnetics devices [33, 34]. Solving this system of three equations yields the surface impedance tensor necessary (at each point on the surface) to ensure the desired distributions of wave vector (5.16) and direction of power flow (5.17) along the surface. Alternatively, the system of three equations needed to find the surface impedance entries can be chosen as: the dispersion equation (5.21), the direction of power flow (5.22), and (5.27).

## 5.4 Example: A Beam-shifting Surface using a TIBC

In this section, a transformation-based beam-shifter [37, 83] is designed using TIBCs. The device can bend a surface-wave beam by an angle of $\theta''_{power}$. The device consists of three regions (as shown in Fig. 5.3): an anisotropic region with surface impedance $\bar{\bar{\eta}}''_{surf}$ sandwiched between two isotropic regions with surface impedance $\bar{\bar{\eta}}_{surf}$. In the uppermost isotropic region, propagation is set to be purely in the $x$-direction. The wave number is chosen to be $k_x = 1.557 k_0 = 326.14$ rad/m at 10 GHz, to ensure a tightly bound wave. The corresponding surface impedance, given by (5.24), is

$$\eta_{surf} = j \begin{pmatrix} 450 & 0 \\ 0 & 450 \end{pmatrix} \Omega. \tag{5.28}$$

This surface will support a $TM$ surface wave with the following propagation characteristics:

$$\overline{k_t} = \begin{pmatrix} k_x \\ k_y \end{pmatrix} = \begin{pmatrix} 326.14 \\ 0 \end{pmatrix} rad/m, \tag{5.29}$$

$$\overline{S_t} = \begin{pmatrix} S_x \\ S_y \end{pmatrix} = \begin{pmatrix} S_x \\ 0 \end{pmatrix} W/m^2. \tag{5.30}$$

The anisotropic region is designed by finding the anisotropic surface impedance tensor $(\bar{\bar{\eta}}''_{surf})$ needed to bend the beam by an angle $\theta''_{power}$ (Fig. 5.3). A coordinate transformation is applied to $\bar{k}_t$ and $\bar{S}_t$ to find the transformed tangential wave vector $(\bar{k}''_t)$ and Poynting vector $(\bar{S}''_t)$ in the anisotropic region. The Jacobian of the coordinate transformation governing the anisotropic region of the beam-shifting device is given by [34]

$$J = \begin{pmatrix} 1 & 0 \\ b & 1 \end{pmatrix}, \tag{5.31}$$
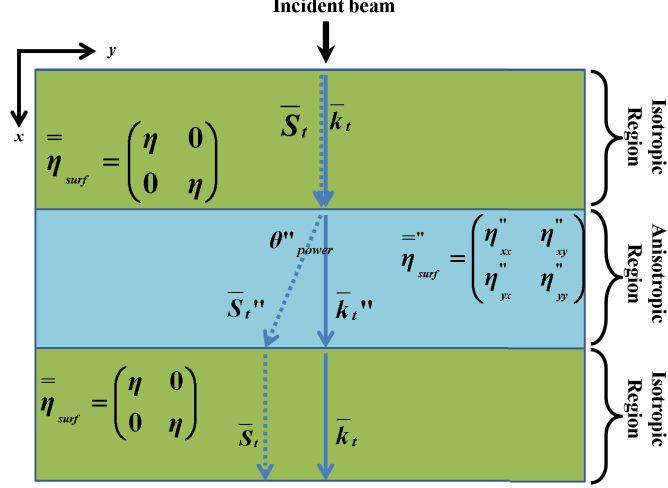
Figure 5.3: A beam-shifting surface consisting of three regions. Two different homogenized media need to be designed; one isotropic and one anisotropic. The anisotropic region is designed to bend the incident beam by $\theta''_{power}$.

where $b = \tan(\theta''_{power})$. The beam-shift angle is chosen to be $\theta_{power} = -23°$ or equivalently, $b = -0.424$. Applying the transformation to $\overline{k}_t$ and $\overline{S}_t$, using (5.16) and (5.17) yields,

$$\overline{k''_t} = \begin{pmatrix} k''_x \\ k''_y \end{pmatrix} = \begin{pmatrix} 326.14 \\ 0 \end{pmatrix} \tag{5.32}$$

and

$$\overline{S''_t} = \begin{pmatrix} S''_x \\ S''_y \end{pmatrix} = \begin{pmatrix} S_x \\ bS_x \end{pmatrix}. \tag{5.33}$$

Applying the design procedure described in the previous section yields the following surface impedance tensor for the anisotropic region:

$$\eta''_{surf} = \begin{pmatrix} \eta''_{xx} & \eta''_{xy} \\ \eta''_{yx} & \eta''_{yy} \end{pmatrix} = j \begin{pmatrix} 488.0 & 173.5 \\ 173.5 & 476.7 \end{pmatrix} \Omega. \tag{5.34}$$

Its dispersion contour is shown in Fig. 5.4.

The beam-shifter was simulated using Ansys HFSS. The isotropic and anisotropic regions (as shown in Fig. 5.3) were modeled using the screening impedance boundary

condition in HFSS. The boundaries of the simulation domain were terminated with radiation boundaries, and one edge was illuminated with a Gaussian beam. The results of the simulation at 10 GHz are shown in Fig. 5.5. As expected, the Gaussian excitation couples energy into the uppermost isotropic surface, and a surface wave propagates in the $x$-direction. Upon encountering the anisotropic medium, the beam is refracted by $-23°$. To an observer at the far edge of the lower isotropic region, (edge opposite of the source), the source appears to have shifted laterally.

Had the surface admittance (5.28) been transformed by (5.12), the transformed surface impedance would be:

$$\eta''_{surf} = \begin{pmatrix} \eta''_{xx} & \eta''_{xy} \\ \eta''_{yx} & \eta''_{yy} \end{pmatrix} = j \begin{pmatrix} 530.9 & 190.8 \\ 190.8 & 450.0 \end{pmatrix} \Omega. \tag{5.35}$$

This surface impedance tensor does not satisfy the guidance condition at 10 GHz unless the free space above the surface is transformed to

$$\epsilon'' = \epsilon_0 \begin{pmatrix} 1 & b \\ b & b^2 + 1 \end{pmatrix} = \epsilon_0 \begin{pmatrix} 1 & -0.424 \\ -0.424 & 1.180 \end{pmatrix} \tag{5.36}$$

$$\mu'' = \mu_0 \begin{pmatrix} 1 & b \\ b & b^2 + 1 \end{pmatrix} = \mu_0 \begin{pmatrix} 1 & -0.424 \\ -0.424 & 1.180 \end{pmatrix} \tag{5.37}$$

via (5.4). This fact was verified using HFSS's eigenmode solver by stipulating the wave vector given by (5.32), across the TIBC (5.35), implemented in HFSS with a screening impedance. The medium above the surface was assigned material parameters given by (5.36) and (5.37). As a result of this simulation, an eigenfrequency of 10 GHz is found by the eigenmode solver. Additionally, finding the ratio of $S''_y$ to $S''_x$ from the simulation verifies the direction of power flow as $\theta''_{power} = -23°$. When the free space above the surface is left untransformed in simulation, the guidance condition
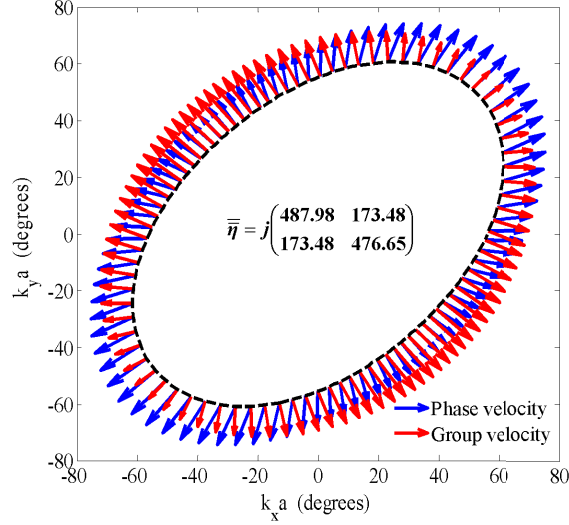
Figure 5.4: The 10 GHz isofrequency contour for the idealized inductive TIBC (anisotropic region) corresponding to the designed TIBC beam-shifter (5.34). Arrows point in the group velocity (red) and phase velocity (blue). The group and phase velocities co-align along the principal axes of the surface. The length of the red arrows represent the normalized magnitude of the group velocity. For propagation along the $x$-axis ($\theta''_{k_t} = 0$), the group velocity vector is separated from the phase velocity arrow by $-23°$ as designed.

is satisfied at 9.65 GHz, which agrees with analytical predictions from the dispersion equation.

In the next section, a beam-shifter is implemented with a PCTIS. In the case of a PCTIS, the unknowns are the sheet admittance tensor entries ($Y_{xx}^{s''}, Y_{xy}^{s''}$, and $Y_{yy}^{s''}$).

## 5.5 Transformation Electromagnetics Applied to Printed-Circuit Tensor Impedance Surfaces (PCTISs)

In this section, a procedure for designing transformation electromagnetics devices using PCTISs is presented. A PCTIS consists of a tensor impedance sheet over a grounded dielectric substrate, where the tensor sheet impedance models a patterned metallic cladding. As shown in the analytical model of a PCTIS (Fig. 5.6), the quantities of interest are the sheet admittance entries. The effective surface impedance
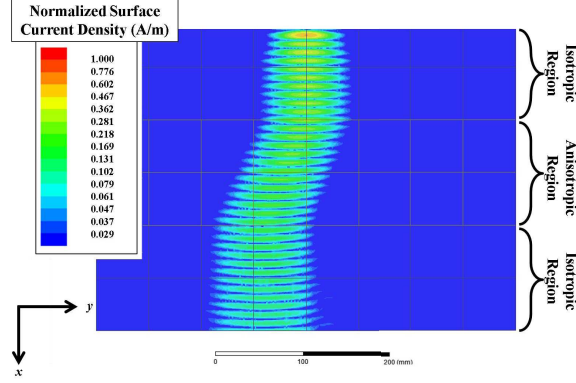
Figure 5.5: Normalized surface current density for the beam-shifting surface. The incoming beam is deflected by $-23°$ in the anisotropic region. The total size of the surface is $48 \times 30$ cm. Each region is $48 \times 10$ cm.
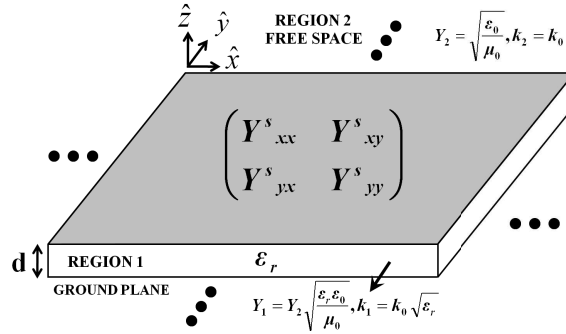


Figure 5.6: PCTIS consisting of a tensor sheet impedance over a grounded dielectric substrate. The tensor sheet impedance/admittance, which models a generalized metallic cladding, is denoted with a superscript 's'.

of a PCTIS was related to the surface impedance of an idealized TIBC in Chapter IV [77]. It was found that a PCTIS exhibits spatial dispersion due to its electrical thickness. As a result of this spatial dispersion, a PCTIS can have the same surface impedance as a TIBC, but a different direction of power flow [74]. The design method presented in the section is analogous to the design procedure for TIBCs from Section 5.3. However, in the case of a PCTIS, one must find the sheet admittance entries $(Y_{xx}^{s\prime\prime}, Y_{xy}^{s\prime\prime} = Y_{yx}^{s\prime\prime}$, and $Y_{yy}^{s\prime\prime})$ that support the transformed wave vector and Poynting vector distributions of a transformation electromagnetics device.

### 5.5.1 Propagation along PCTISs

The modes supported by a PCTIS can be found from eigenvalue equation (3.26) in Chapter III [53]. The dispersion equation for a PCTIS, derived in Chapters III and IV [53, 77], can be written as

$$
4\epsilon_1 k_1^2 k_2^2 k_{z1}'' k_{z2}'' \mu_2 \omega \cos^2(k_{z1}'' d)
$$

$$
+ j \sin(2k_{z1}'' d)
$$

$$
[2\epsilon_1 k_2^4 (k_{z1}'')^2 \mu_1 \omega + 2\epsilon_2 k_1^4 (k_{z2}'') \mu_2 \omega
$$

$$
+ k_1^4 k_2^2 k_{z2}'' \mu_2 Y_{xx}^{s''} + \epsilon_1 k_2^2 (k_{z1}'')^2 k_{z2}'' \mu_1 \mu_2 \omega^2 Y_{xx}^{s''}
$$

$$
+ k_1^4 k_2^2 k_{z2}'' \mu_2 Y_{yy}^{s''} + \epsilon_1 k_2^2 (k_{z1}'')^2 k_{z2}'' \mu_1 \mu_2 \omega^2 Y_{yy}^{s''}
$$

$$
- k_2^2 k_{z2}'' \mu_2 (k_1^4 - \epsilon_1 (k_{z1}'')^2 \mu_1 \omega^2)(Y_{xx}^{s''} - Y_{yy}^{s''}) \cos(2\theta_k'')
$$

$$
- k_2^2 k_{z2}'' \mu_2 (k_1^4 - \epsilon_1 (k_{z1}'')^2 \mu_1 \omega^2)(Y_{xy}^{s''} + Y_{yx}^{s''}) \sin(2\theta_k'')] \qquad (5.38)
$$

$$
- 2k_1^2 k_z'' \mu_1 \sin^2(k_{z1}'' d)
$$

$$
[2\epsilon_2 k_2^2 k_{z2}'' \omega + k_2^4 Y_{xx}^{s''} + \epsilon_2 k_{z2}^2 \mu_2 \omega^2 Y_{xx}^{s''}
$$

$$
- 2k_2^2 k_{z2}'' \mu_2 \omega Y_{xy}^{s''} Y_{yx}^{s''} + k_2^4 Y_{yy}^{s''} + \epsilon_2 (k_{z2}'')^2 \mu_2 \omega^2 Y_{yy}^{s''}
$$

$$
+ 2k_2^2 k_{z2}'' \mu_2 \omega Y_{xx}^{s''} Y_{yy}^{s''}
$$

$$
- (k_2^4 - \epsilon_2 (k_{z2}'')^2 \mu_2 \omega^2)(Y_{xx}^{s''} - Y_{yy}^{s''}) \cos(2\theta_k'')
$$

$$
- (k_2^4 - \epsilon_2 (k_{z2}'')^2 \mu_2 \omega^2)(Y_{xy}^{s''} + Y_{yx}^{s''}) \sin(2\theta_k'')] = 0.
$$

Furthermore, the group velocity and direction of power flow were derived in Section 4.5 of Chapter IV [74]. The dispersion equation and the direction of power flow constitute two of the three equations needed to design a PCTIS that supports a surface wave with transformed wave vector and Poynting vector distributions.

### 5.5.2 Design Approach

Similar to the design approach for TIBCs outlined in Section 5.3, an initial anisotropic medium must be determined. An isotropic sheet admittance,

$$\overline{\overline{Y}}_{sheet} = \begin{pmatrix} Y^s & 0 \\ 0 & Y^s \end{pmatrix}, \tag{5.39}$$

is chosen to support a surface wave, with a desired transverse wave number, $k_t$, at a frequency of operation. For a TM surface wave, the isotropic sheet impedance is found from the TM transverse resonance equation

$$Y^s = Y_{surf}^{TM} + jY_1 \frac{k_1}{k_{z1}} \cot(k_{z1}d). \tag{5.40}$$

or equivalently,

$$Y^s = \frac{Y_0}{\sqrt{1 - \left(\frac{k_t}{k_0}\right)^2}} + jY_1 \frac{k_1}{\sqrt{k_1^2 - k_t^2}} \cot(\sqrt{k_1^2 - k_t^2}d). \tag{5.41}$$

The transformed wave vector and Poynting vector are found from (5.16) and (5.17), respectively. Next, the sheet impedance tensor,

$$\overline{\overline{Y}}_{sheet}'' = \begin{pmatrix} Y_{xx}^{s\prime\prime} & Y_{xy}^{s\prime\prime} \\ Y_{yx}^{s\prime\prime} & Y_{yy}^{s\prime\prime} \end{pmatrix}, \tag{5.42}$$

that supports the transformed wave vector and Poynting vector, is found by solving a system of three equations: the dispersion equation for a PCTIS (5.38), the direction of power flow along a PCTIS (equation (4.71) from Chapter IV), and a condition on the determinant of the transformed sheet admittance,

$$Y_{xx}^{s\prime\prime}Y_{yy}^{s\prime\prime} - Y_{xy}^{s\prime\prime}Y_{yx}^{s\prime\prime} = (Y^s)^2. \tag{5.43}$$

Additionally, we must ensure that only a single $TM$ mode is supported by the PCTIS. That is, the next $TE$ mode should be avoided. The $TE$ mode cutoff occurs when $Y_{surf}^{TE} = 0$. The $TE$ transverse resonance equation is given by

$$Y_{critical}^s = jY_1 \frac{k_{z1}}{k_1} \cot(k_{z1}d), \tag{5.44}$$

where $Y_{critical}^s$ is the sheet admittance at cutoff. The eigenvalues ($Y_{\lambda_1}^s$ and $Y_{\lambda_2}^s$) of $Y_{sheet}''$ can be found by diagonalizing $Y_{sheet}''$,

$$\overline{\overline{P}}^{-1} \overline{\overline{Y}}_{sheet}'' \overline{\overline{P}} = \begin{pmatrix} Y_{\lambda_1}^s & 0 \\ 0 & Y_{\lambda_2}^s \end{pmatrix}, \tag{5.45}$$

where $\overline{\overline{P}}$ is a matrix containing the eigenvectors of $Y_{sheet}''$. In order to ensure that the $TE$ mode is not excited, the eigenvalues ($Y_{\lambda_1}^s$ and $Y_{\lambda_2}^s$) of $Y_{sheet}''$ must not exceed $Y_{critical}^s$. When either of the eigenvalues is equal to $Y_{critical}^s$, the $TE$ mode can be excited. Beyond this resonance, the surface impedance is capacitive and a $TE$ mode is supported in addition to the $TM$ mode. In other words, the following conditions must be satisfied in order to guarantee only one $TM$ mode exists:

$$Y_{\lambda_1}^s < Y_{critical}^s \tag{5.46}$$

and

$$Y_{\lambda_2}^s < Y_{critical}^s \tag{5.47}$$

where

$$Y_{\lambda_1}^s = \frac{Y_{xx}^{s\prime\prime} + Y_{yy}^{s\prime\prime} - \sqrt{Y_{xx}^{s\prime\prime 2} + 4Y_{xy}^{s\prime\prime}Y_{yx}^{s\prime\prime} - 2Y_{xx}^{s\prime\prime}Y_{yy}^{s\prime\prime} + Y_{yy}^{s\prime\prime 2}}}{2}, \tag{5.48}$$

$$Y_{\lambda_2}^s = \frac{Y_{xx}^{s\prime\prime} + Y_{yy}^{s\prime\prime} + \sqrt{Y_{xx}^{s\prime\prime 2} + 4Y_{xy}^{s\prime\prime}Y_{yx}^{s\prime\prime} - 2Y_{xx}^{s\prime\prime}Y_{yy}^{s\prime\prime} + Y_{yy}^{s\prime\prime 2}}}{2}. \tag{5.49}$$

Simultaneously solving the three aforementioned equations under the constraints of (5.46) and (5.47), the tensor sheet admittance entries $(Y_{xx}^{s\prime\prime}, Y_{xy}^{s\prime\prime}$, and $Y_{yy}^{s\prime\prime})$ can be found. The initial isotropic medium $(Y^s)$ may have to be adjusted in (5.43) in order to satisfy (5.46) and (5.47). Essentially, this condition places a limitation on the beam-shift angles achievable for a substrate with a given thickness and dielectric constant.

## 5.6 Example: A Beam-shifter using a PCTIS

In this section, a beam-shifter is designed using a PCTIS. The device can bend a surface-wave beam by $-13.93°$ at 10 GHz. It consists of three regions, as shown in Fig 3. The PCTIS beam-shifter consists of an isotropic sheet impedance in the upper and lower regions and an anisotropic sheet impedance in the middle. The sheets are on a 1.27 mm thick grounded dielectric substrate with $\epsilon_r=10.2$. In the isotropic region, propagation is chosen to be in the $x$-direction with a transverse wave number of $k_x = 1.1882k_0 = 248.85$ rad/m. The isotropic sheet impedance, calculated using (5.39) and (5.41) is

$$\eta_{sheet=}Y_{sheet}^{-1} = j \begin{pmatrix} -199.33 & 0 \\ 0 & -199.33 \end{pmatrix} \Omega. \tag{5.50}$$

The transformed wave and Poynting vectors are found to be

$$\overline{k_t''} = \begin{pmatrix} k_x'' \\ k_y'' \end{pmatrix} = \begin{pmatrix} 248.85 \\ 0 \end{pmatrix}, \tag{5.51}$$

and

$$\overline{S_t''} = \begin{pmatrix} S_x'' \\ S_y'' \end{pmatrix} = \begin{pmatrix} S_x \\ bS_x \end{pmatrix}. \tag{5.52}$$

132
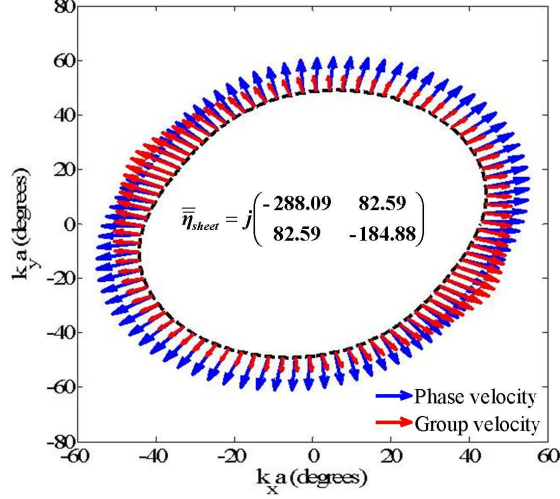
Figure 5.7: The 10 GHz isofrequency contour for the anisotropic region of the designed PCTIS beam-shifter (5.34). Arrows point in the group velocity (red) and phase velocity (blue). The group and phase velocities co-align along the principal axes of the surface. The length of the red arrows represent the normalized magnitude of the group velocity. For propagation along the $x$-axis ($\theta''_{k_t} = 0$), the group velocity vector is separated from the phase velocity arrow by $-13.93°$ as designed.

Solving the system of three equations ((5.38), (4.71), and (5.43)) discussed in the design procedure yields the following sheet impedance tensor for the anisotropic region:

$$\eta''_{sheet=}(Y''_{sheet})^{-1} = j \begin{pmatrix} -288.09 & 82.59 \\ 82.59 & -184.88 \end{pmatrix} \Omega. \tag{5.53}$$

The dispersion contour for this PCTIS is shown in Fig. 5.7.

The beam-shifter was simulated using HFSS. The isotropic and anisotropic regions were modeled using the screening impedance boundary condition over a grounded dielectric substrate. The boundaries of the simulation domain were terminated with radiation boundaries, and one edge was illuminated with a Gaussian beam. The results of the simulation at 10 GHz are shown in Fig. 5.8. As expected, the Gaussian beam is refracted by $-13.9°$ upon encountering the anisotropic medium.

For the chosen substrate, $Y^s_{critical} = 1/(-130j)$ S at 10 GHz. The eigenvalues
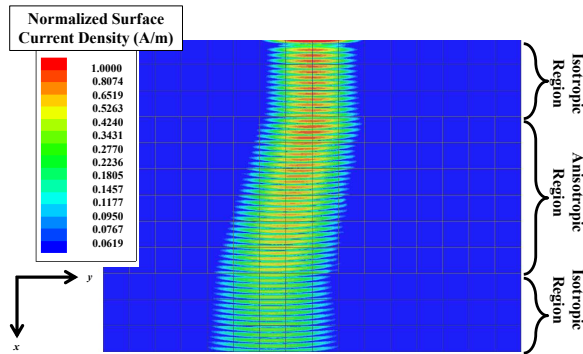
Figure 5.8: Normalized surface current density for the PCTIS beam-shifting surface. The incoming beam is deflected by $-13.93°$ in the anisotropic region. The total size of the surface is $96 \times 72$ cm. Each isotropic region is $48 \times 180$ cm. The dimensions of the anisotropic region are $48 \times 36$ cm.
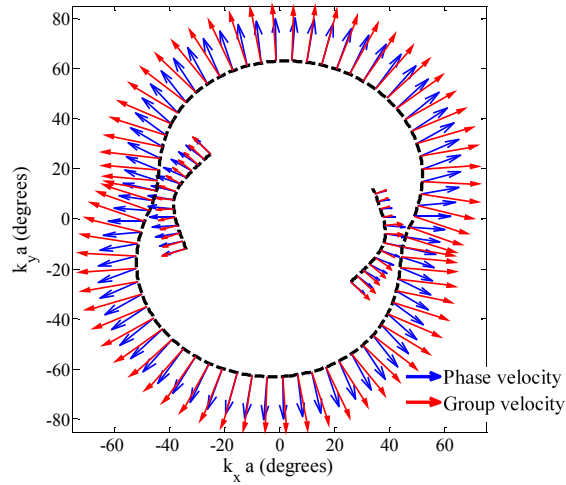


Figure 5.9: The 10 GHz isofrequency contour for the anisotropic region of a PCTIS beam-shifter with two modes present. (5.34).
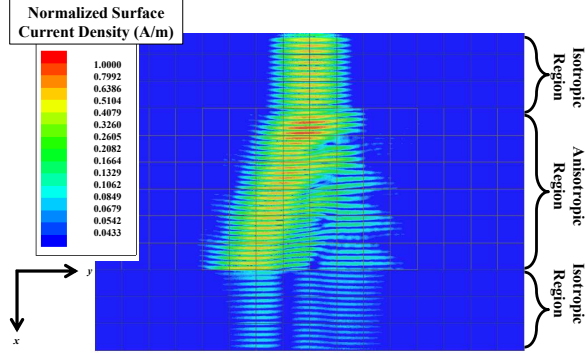
Figure 5.10: Normalized surface current density for the PCTIS beam-shifting surface. The incoming beam is deflected in two different directions in the anisotropic region. This is due to the presence of two modes as shown in Fig. 5.7. The total size of the surface is $96 \times 72$ cm. Each isotropic region is $48 \times 180$ cm. The dimensions of the anisotropic region are $48 \times 36$ cm.

(diagonalized sheet admittance values) of (5.53) are $Y_{\lambda_1}^s = 1/(-333.87j)$ S and $Y_{\lambda_2}^s = 1/(-139.10j)$ S, and therefore satisfy (5.46) and (5.47). If conditions (5.46) and (5.47) are not satisfied, a $TM$ and a $TE$ mode co-exist. The 10 GHz dispersion contour for such a situation is shown in Fig. 5.9. The sheet impedance corresponding to this dispersion contour is

$$\eta''_{sheet} = (Y''_{sheet})^{-1} = j \begin{pmatrix} -384.84 & 65.72 \\ 65.72 & -115.16 \end{pmatrix} \Omega. \tag{5.54}$$

and the eigenvalues of $Y''_{sheet}$ are $Y_{\lambda_1}^s = 1/(-100j)$ S and $Y_{\lambda_2}^s = 1/(-400j)$ S. In this case, propagation along certain directions of the the beam-shifter will produce two beams. This is verified with full-wave simulation (results shown in Fig. 5.10) for propagation along the $x$-axis.

## 5.7 Chapter Summary

In this chapter, it was shown how the idealized TIBC transforms according to the traditional transformation electromagnetics method. Further, it was shown that

transforming an impedance/admittance surface necessarily results in a transformation of the free space above it. An alternate procedure is proposed that allows transformation electromagnetics devices to be implemented using TISs, while maintaining free space above. The proposed method allows anisotropic TIBCs and PCTISs to be designed that support tangential wave vector and Poynting vector distributions specified by a coordinate transformation. Beam-shifters are designed (both a TIBC and a PCTIS version) that laterally shift a surface wave beam at 10 GHz. These designs highlight the TIS toolkit that has been developed in Chapters III and IV.

# CHAPTER VI

# Conclusion

## 6.1 Summary of Contributions

The aim of this thesis has been to provide an improved understanding of the guidance characteristics of scalar and tensor impedance surfaces, and to develop step-by-step methods for determining the surface impedance profile necessary to achieve desired radiative or wave-guiding properties. Developing methods to implement these surfaces as practical printed-circuit structures, and building and testing prototype devices were also goals of this thesis.

In Chapter II, sinusoidally modulated surface impedances were explored. A simplified design procedure was presented that allows phase and leakage constants to be independently controlled along a surface. This procedure allowed the design of surfaces with prescribed beam pointing directions (off-broadside) and beam widths. A leaky-wave antenna was realized by implementing the designed surface as a printed-circuit structure consisting of metallic strips over a grounded dielectric substrate. A method for determining the appropriate metal strip widths from normal incidence scattering simulations was presented. The antenna was fabricated and measured and showed close agreement with full-wave simulation.

Chapters III and IV were dedicated to idealized tensor impedance boundary conditions (TIBCs) and their implementation as printed-circuit tensor impedance surfaces

(PCTISs). A PCTIS consists of a tensor impedance sheet over a grounded dielectric substrate. The tensor impedance sheet models a patterned metallic cladding. The respective dispersion equations for a TIBC and a PCTIS were derived using field analysis in Chapter III, and then again using a modified transverse resonance technique in Chapter IV. The modified transverse resonance technique is a generalization of the conventional transverse resonance technique [41] that is valid for tensor impedances. It provides an elegant method for analyzing the modes supported by TIBCs and PCTISs. An extraction method, which allow the sheet impedance of a PCTIS's metallic cladding to be found using two normal incidence scattering simulations (without prior knowledge of the structure's principal axes), was introduced in Chapter III. Combining the extraction method and the dispersion equation for a PCTIS, the dispersion characteristics of a few example PCTISs were accurately predicted over a range of frequencies. This was accomplished with better accuracy and less simulation time compared to previous methods in literature. An explicit expression for the effective surface impedance of a PCTIS was derived, allowing PCTISs and TIBCs to be directly related. It was found that the effective surface impedance is, in general, dependent on the direction of propagation along the PCTIS. Therefore, it exhibits spatial dispersion. The conditions necessary to approximate the PCTIS as an angle-independent TIBC were discussed. Additionally, expressions for the group velocity and direction of power flow along TIBCs and PCTISs were derived.

In Chapter V, a method for designing transformation electromagnetics devices using tensor impedance surfaces (TISs) was outlined. The transformed wave vector and Poynting vector distributions of the device were found using transformation electromagnetics. The method allowed TIBCs and PCTISs to be designed that support the transformed wave-vector and Poynting vector distributions, while maintaining free space above the surface. Finally, beam-shifters that shifted a surface-wave beam laterally were designed using both a TIBC and a PCTIS.

## 6.2 Future Work

The research presented in the previous chapters aimed to extend the theoretical understanding of TISs and improve the way that devices based on TISs are currently characterized. We have established a fertile platform that can be used for many applications. However, there are many aspects of the research presented in this thesis that deserve further attention.

### 6.2.1 Realization of PCTIS Beam-shifter

In Chapter V, a method for designing transformation electromagnetics devices using TIBCs was introduced. The method was also adapted for PCTISs. A PCTIS beam-shifter was designed by finding the necessary sheet impedances for the isotropic and anisotropic regions of the beam-shifting device. Some work for the near future could include fabricating this device. The metallic cladding must be patterned to realize the required sheet impedances. Once the appropriate cladding patterns are found, the beam-shifter can be realized on a printed-circuit board (PCB) and its performance tested.

The PCTIS beam-shifter designed in the Chapter V can be implemented by patterning the metallic cladding above a 1.27 mm thick grounded dielectric substrate with $\epsilon_r = 10.2$. Using the extraction method from Chapter III [53], a unit cell can be designed for the anisotropic region (see Fig. 6.1) that has a sheet impedance identical to that of (5.54). The isotropic region of the beam-shifter can be implemented by printing a square patch over the grounded dielectric substrate, similar to Fig. 6.1, but without the diagonal gap through it.

### 6.2.2 Circuit-model for tensor impedance sheets

In Chapter V, we presented a method to design transformation electromagnetics devices using PCTISs. This method maps a desired wave vector and Poynting vector
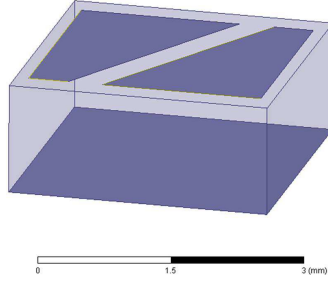
Figure 6.1: Unit cell of PCTIS beam-shifter implementation (anisotropic region). Dark areas represent metal. The sheet impedance can be designed to be identical to (5.54).

distribution to the required sheet impedance tensors at every point on the surface. Therefore, when realizing these anisotropic and inhomogeneous surfaces with PCBs, there is a need for a design database that maps sheet impedance tensors to metallic cladding patterns. In Chapter III of this thesis, we presented an efficient way to map metallic cladding patterns to sheet impedance tensors (tensor sheet extraction method), which would allow a design database to be constructed with significantly fewer full-wave simulations than methods reported previously in literature. However, full-wave simulation would still be necessary. Future work could include developing analytical methods (based on expressions for gap capacitance, for example) for mapping sheet impedance to metallic cladding patterns. Combining this with a circuit model, similar to the one introduced in [36], could ultimately allow wave vector and Poynting vector distributions to be mapped analytically to cladding geometries.

### 6.2.3 Leaky-waves

The dispersion equations presented in Chapters III and IV were solved for their surface wave solutions. These dispersion equations are also valid for leaky-waves. Future work could include solving these equations for their leaky wave roots. For leaky waves, the transverse wave number can be complex.

### 6.2.4 Multi-layer structures

The modified transverse resonance technique, introduced in Chapter IV, was elegant in the sense that dispersion equations for a TIBC and a PCTIS could be found virtually by inspection. Future work could include generalizing this method to handle multi-layer stackups.

## 6.3 List of Publications

The work in this thesis has been published in the following peer-reviewed journals and conference proceedings.

### 6.3.1 Journal Papers

1. **A. M. Patel** and A. Grbic, "Transformation Electromagnetics Devices based on Tensor Impedance Surfaces," Manuscript in preparation for *IEEE Transactions on Microwave Theory and Techniques*, Mar. 2013.

2. **A. M. Patel** and A. Grbic, "The Effects of Spatial Dispersion on Power Flow along a Printed-Circuit Tensor Impedance Surface," Manuscript in preparation for *IEEE Transactions on Antennas and Propagation*, Mar. 2013.

3. **A. M. Patel** and A. Grbic, "Effective Surface Impedance of a Printed-circuit Tensor Impedance Surface (pctis)," To appear in *IEEE Transactions on Microwave Theory and Techniques*, pp. 1-11, Accepted Feb. 2013.

4. **A. M. Patel** and A. Grbic, "Modeling and Analysis of Printed-circuit Tensor Impedance Surfaces," *IEEE Transactions on Antennas and Propagation*, vol. 61, no. 1, pp. 211-220, Jan. 2013.

5. **A. M. Patel** and A. Grbic, "A printed leaky-wave antenna based on a sinusoidally-modulated reactance surface," *IEEE Transactions on Antennas and Propaga-*

*tion*, vol. 59, no. 6, pp. 2087-2096, Jun. 2011.

### 6.3.2 Conference Proceedings

1. **A. M. Patel** and A. Grbic, "Transformation electromagnetics devices using tensor impedance surfaces," in *IEEE International Microwave Symposium*, 2013., Seattle, WA, Jun. 2-7, 2013.

2. A. Grbic, G. Gok, M. F. Imani, **A.M. Patel**, C. Pfeiffer, and M. Ettorre. "Metamaterial Surfaces for Near and Far-Field Applications." EuCAP 2013, Gothenburg, Sweden, Apr 8-12, 2013. (Invited Paper).

3. **A. M. Patel** and A. Grbic, "Dispersion analysis of printed-circuit tensor impedance surfaces," in *IEEE Antennas and Propagation Society International Symposium* (APSURSI), 2012, Chicago, IL, Jul. 8-14 2012, pp. 1-2. (Student Paper Competition - 2nd prize).

4. **A. M. Patel** and A. Grbic, "Analytical modeling of a printed-circuit tensor impedance surface," in *IEEE MTT-S International Microwave Symposium Digest (MTT)*, 2012, Montreal, QC, Canada, Jun. 17-22 2012, pp. 1-3.

5. **A. M. Patel** and A. Grbic, "A printed leaky-wave antenna with a sinusoidally modulated surface reactance," in *IEEE Antennas and Propagation Society International Symposium*, 2009. APSURSI '09., Charleston, SC, Jun. 1-5 2009, pp. 1-4. (Student Paper Competition - 1st prize).

### 6.3.3 Conference Summaries

1. **A. M. Patel** and A. Grbic, "Transformation electromagnetics devices using tensor impedance surfaces," in *USNC/URSI National Radio Science Meeting*, 2013. APSURSI '13., Lake Buena Vista, FL, Jul. 7-12, 2013.

142

2. **A. M. Patel**, A. Grbic, "Multi-layer Tensor Impedance Surface Analysis."
*URSI National Radio Science Meeting*, Boulder, CO, Jan 4-7, 2012.

# APPENDICES

# APPENDIX A

# Sheet Impedance Approximation At Normal Incidence

The extraction method presented in Chapter II is approximate since the sheet impedance extracted from normal incidence scattering simulations ($\beta = 0$), is used to find the modal surface impedance (away from $\beta = 0$). In general, the sheet impedance can be a function of $\beta$. This is typically true for frequency selective surfaces (FSSs) where the unit cell size is comparable to a wavelength. However, for low frequencies, where the unit cell size is much smaller than a wavelength, the sheet impedance at normal incidence ($\beta = 0$) is accurate even for oblique incidence ($\beta$ away from zero). This fact is verified in this Appendix.

The equivalent admittance of a printed-circuit FSS is expressed in [56], as the parallel combination of the sheet admittance of the FSS ($Y_{sheet}(\beta, \omega)$) and the grounded dielectric substrate. For a TM wave, the sheet admittance is given by (4) in [56]:

$$Y_{sheet}^{TM}(\beta, \omega) = \frac{j\omega C_0^{TM}(\omega^2 - [\omega_{z1}^{TM}(\beta)]^2)(\omega^2 - [\omega_{z2}^{TM}(\beta)]^2)...}{(\omega^2 - [\omega_{p1}^{TM}(\beta)]^2)(\omega^2 - [\omega_{p2}^{TM}(\beta)]^2)...}. \tag{A.1}$$

where $C_0^{TM}$ is a constant and $\omega_{zn}^{TM}(\beta)$ and $\omega_{pn}^{TM}(\beta)$ are the zeroes and poles of the sheet admittance. The poles and zeros can be identified from full-wave reflection
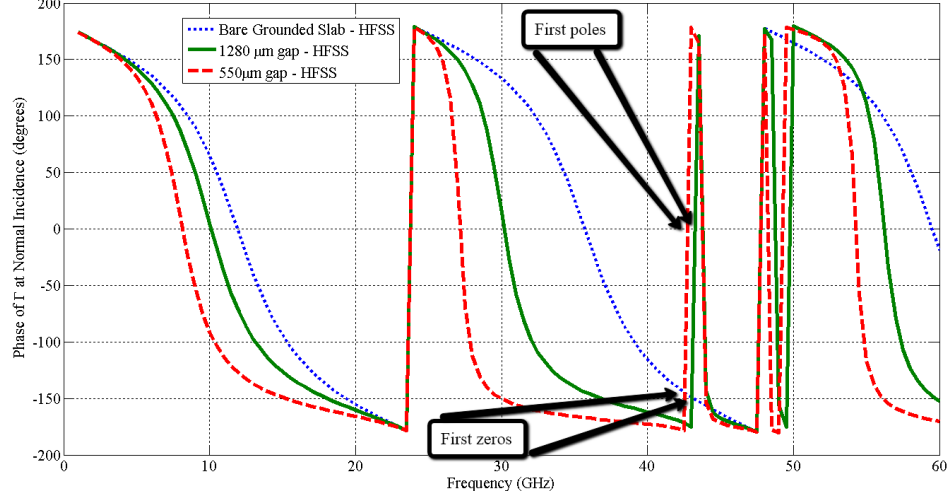
Figure A.1: Phase of reflection coefficient at normal incidence for a bare grounded slab (blue dotted), 1280 $\mu$m gap (green solid), and 550 $\mu$m gap (red dashed).

coefficient data. The phase of the reflection coefficient is denoted $\angle\Gamma$. The poles are at those frequencies where $\angle\Gamma$ transitions from $+180°$ to $-180°$. The zeroes occur at the frequencies where $\angle\Gamma$ equals the phase of the reflection coefficient of the bare grounded dielectric slab.

Fig. A.1 shows the phase of the reflection coefficient at normal incidence for the largest (1280 $\mu$m) and smallest (550 $\mu$m) printed gap geometries used in the leaky-wave antenna of Chapter II. Fig. A.2 shows the phase of the reflection coefficient at 45° incidence. At the operating frequency of 10 GHz (unit cell size of about $\lambda/11$), we are operating far from poles and zeros. The resonance at approximately 24 GHz is where the thickness of the slab is $\lambda_{dielectric}/2$.

The dashed lines in Fig. A.3 and Fig. A.4 show the simulated phase of the reflection coefficient at 45° incidence for both gap geometries. The solid lines with markers show the analytically calculated reflection coefficient phases, assuming a sheet impedance extracted from normal incidence HFSS simulations. There is very close agreement (in Figs. A.3 and A.4) up to approximately 24 GHz between simulated
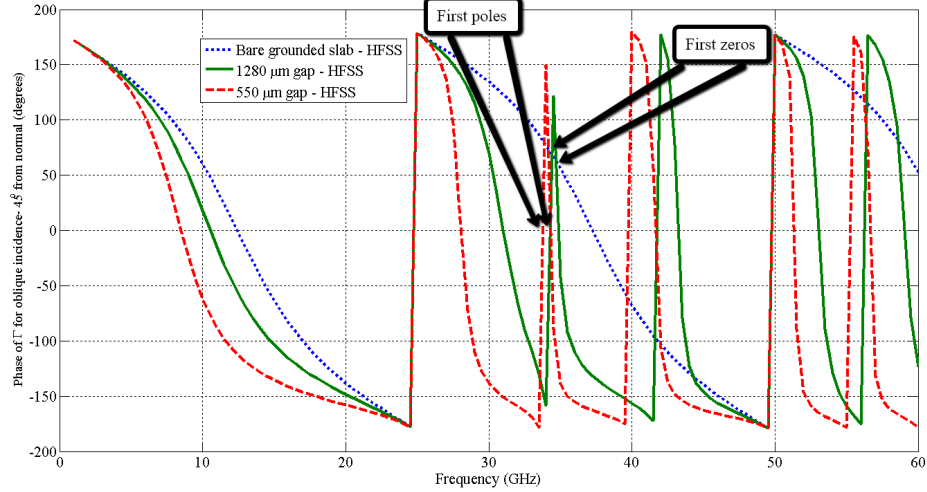
Figure A.2: Phase of reflection coefficient for oblique incidence (45 degrees from normal) for a bare grounded slab (blue dotted), $1280\mu$m gap (green solid), and 550 $\mu$m gap (red dashed).

and analytically calculated reflection coefficient phase. This indicates that the sheet impedance extracted from normal incidence simulation is a valid approximation for the sheet impedance even away from $\beta = 0$ when the cell size is small compared to the wavelength. The design frequency of our antenna is 10 GHz, which is well within the range where the approximation holds.

Fig. 2.13 in Chapter II is a plot comparing the Driven Method (proposed in Section 2.4 of this thesis) to the Eigenmode Method. The Eigenmode Method does not use normal-incidence simulations to determine the sheet impedance. We see close agreement between the two methods further indicating that the sheet impedance does not vary significantly as a function of $\beta$ for our frequency range of operation.
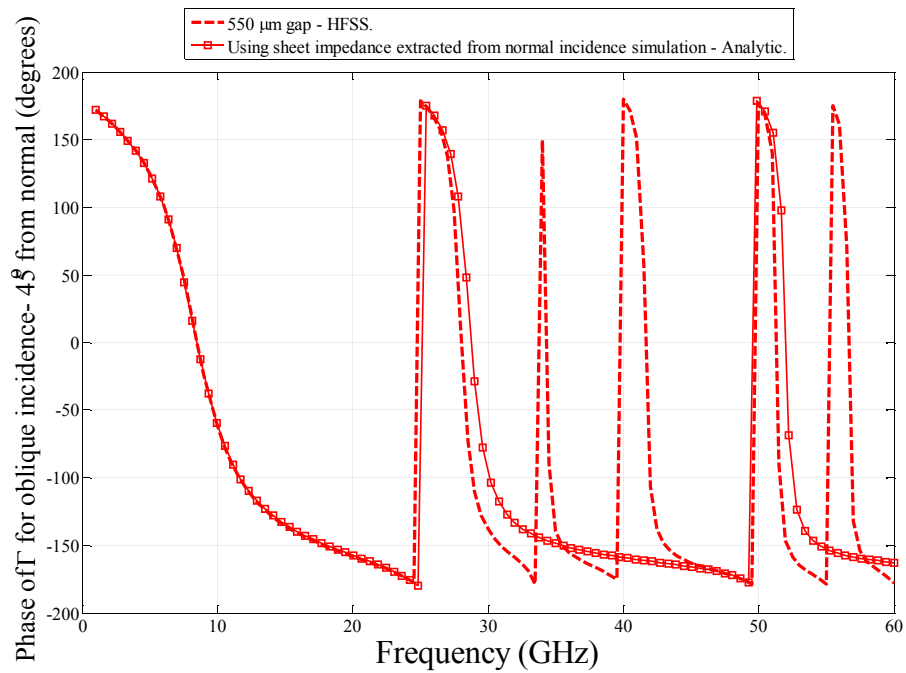
Figure A.3: Phase of reflection coefficient for oblique incidence (45 degrees from normal) from HFSS simulation of $550\mu$m gap geometry (red dashed), and analytical calculation using the sheet impedance extracted from normal incidence scattering simulation (red solid with markers).
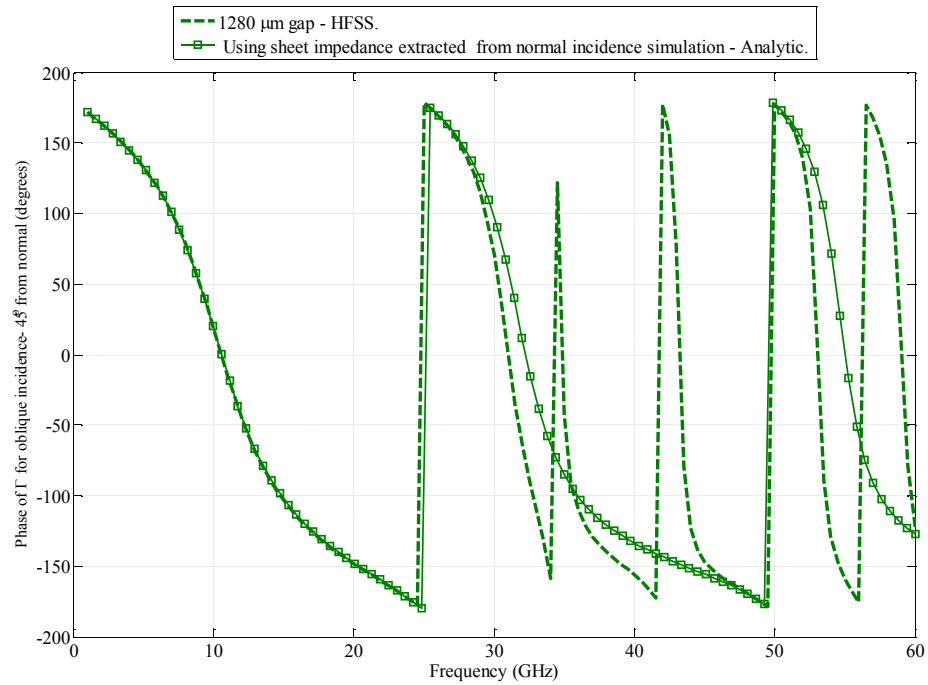
Figure A.4: Phase of reflection coefficient for oblique incidence (45 degrees from normal) from HFSS simulation of $1280\mu$m gap geometry (green dashed), and analytical calculation using the sheet impedance extracted from normal incidence scattering simulation (green solid with markers).

# APPENDIX B

# Modified Formulation Accounting for Dielectric Thickness and Periodic Sheet Impedance

## B.1 Dispersion Equation for an Arbitrary Periodic Sheet Impedance over a Grounded Dielectric Substrate

This formulation seeks to accurately predict both $\alpha$ and $\beta$ for a arbitrary periodic sheet impedance over a grounded dielectric substrate by accounting for dielectric thickness (see Fig. B.1). The fields in regions 1 and 2 can be expressed in terms of their Floquet harmonics due to the periodicity of $\eta_{sheet}$. The fields in regions 1 and 2 are:
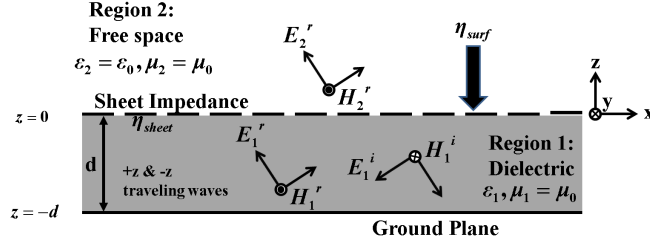
Figure B.1: Geometry of modified formulation for finding $\kappa$ accounting for dielectric thickness and arbitrary periodic sheet impedance.

$$H_{y1} = \sum_{n=-\infty}^{\infty} A_n \cos(k_{zn1}(d+z))e^{-jk_{xn}x} \tag{B.1}$$

$$E_{z1} = \sum_{n=-\infty}^{\infty} A_n \frac{-k_{xn}}{\omega\epsilon_1} \cos(k_{zn1}(d+z))e^{-jk_{xn}x} \tag{B.2}$$

$$E_{x1} = \sum_{n=-\infty}^{\infty} A_n \frac{jk_{zn1}}{\omega\epsilon_1} \sin(k_{zn1}(d+z))e^{-jk_{xn}x} \tag{B.3}$$

$$H_{y2} = \sum_{n=-\infty}^{\infty} B_n e^{-jk_{zn2}z}e^{-jk_{xn}x} \tag{B.4}$$

$$E_{z2} = \sum_{n=-\infty}^{\infty} B_n \frac{-k_{xn}}{\omega\epsilon_2} e^{-jk_{zn2}z}e^{-jk_{xn}x} \tag{B.5}$$

$$E_{x2} = \sum_{n=-\infty}^{\infty} B_n \frac{k_{zn2}}{\omega\epsilon_2} e^{-jk_{zn2}z}e^{-jk_{xn}x} \tag{B.6}$$

where $k_{xn} = \kappa + \frac{2\pi n}{a}$ and the coefficients $A_n$ and $B_n$ represent the amplitudes of the magnetic field spatial harmonics inside the dielectric and in free space, respectively. Applying the PEC (perfect electric conductor) boundary conditions at $z = 0$, the total tangential electric field must vanish and $E_{x1} - E_{x2} = 0$. This yields

$$\sum_{n=-\infty}^{\infty} A_n \frac{jk_{zn1}}{\omega\epsilon_1} \sin(k_{zn1}d)e^{-j\left(\kappa+\frac{2\pi n}{a}\right)x} \tag{B.7}$$

$$= \sum_{n=-\infty}^{\infty} B_n \frac{k_{zn2}}{\omega\epsilon_2} e^{-j\left(\kappa+\frac{2\pi n}{a}\right)x}$$

The magnetic field boundary condition at $z = 0$ states that $H_{y1} - H_{y2} = J_x = \frac{E_{x2}}{\eta_{sheet}}$ where $J_x$ represents the surface currents. This equation yields

$$\frac{\displaystyle\sum_{n=-\infty}^{\infty} B_n \frac{k_{zn2}}{\omega\epsilon_2} e^{-j\left(\kappa+\frac{2\pi n}{a}\right)x}}{\eta_{sheet}(x)} \tag{B.8}$$

$$= \sum_{n=-\infty}^{\infty} A_n \cos(k_{zn1}d)e^{-j\left(\kappa+\frac{2\pi n}{a}\right)x} - B_n e^{-j\left(\kappa+\frac{2\pi n}{a}\right)x}$$

Taking the inner product of (B.7) and $e^{j\left(\kappa+\frac{2\pi g}{a}\right)x}$ over one period, and invoking orthogonality yields

$$A_n \frac{jk_{zn1}}{\epsilon_1} \sin(k_{zn1}d) = B_n \frac{k_{zn2}}{\epsilon_2}, \tag{B.9}$$

which relates the $A_n$ coefficients to the $B_n$ coefficients. Using (B.9) to substitute for $A_n$ in (B.8) yields an expression solely in terms of $B_n$'s which are the magnetic field amplitudes of the spatial harmonics in free space.

$$\sum_{n=-\infty}^{\infty} B_n \frac{k_{zn2}}{\omega\epsilon_2} e^{-j\left(\kappa+\frac{2\pi n}{a}\right)x} \tag{B.10}$$

$$= \eta_{sheet} \left[ \sum_{n=-\infty}^{\infty} B_n(-j)\frac{k_{zn2}}{k_{zn1}}\frac{\epsilon_1}{\epsilon_2}\cot(k_{zn1}d)e^{-j\left(\kappa+\frac{2\pi n}{a}\right)x} \right.$$

$$\left. - \sum_{n=-\infty}^{\infty} B_n e^{-j\left(\kappa+\frac{2\pi n}{a}\right)x} \right]$$

The $\eta_{sheet}$ due to a certain $\eta_{surf}$ can be found using (2.11). Since $\eta_{sheet}$ is periodic, it can be represented by a Fourier series

$$\eta_{sheet} = \sum_{m=-\infty}^{\infty} \eta_m e^{-j\frac{2\pi m}{a}x} \tag{B.11}$$

where $\eta_m$ represents the Fourier series weighting coefficient of the $m^{th}$ term. Substituting (B.11) into (B.10) and then taking the inner product of the resulting equation and $e^{j\left(\kappa+\frac{2\pi p}{a}\right)x}$ over one period gives

$$\frac{1}{\omega\epsilon_2}B_p k_{zp2} = \sum_{n=-\infty}^{\infty} B_n \eta_{p-n}\left(-j\frac{k_{zn2}}{k_{zn1}}\frac{\epsilon_1}{\epsilon_2}\cot(k_{zn1}d)-1\right)$$

This can be written in the form of a matrix equation representing an infinite number of equations and an infinite number of unknowns.

$$\bar{\bar{Q}}\bar{B}_n = \frac{1}{\omega\epsilon_2}\bar{B}_p \tag{B.12}$$

where the entries of the matrix $Q$ are functions of $\kappa$ and are given by

$$Q_{p,n} = \frac{1}{k_{zp2}}\left(-j\frac{k_{zn2}}{k_{zn1}}\frac{\epsilon_1}{\epsilon_2}\cot(k_{zn1}d)-1\right)\eta_{p-n} \tag{B.13}$$

By truncating indicies $n$ and $p$ symmetrically about zero and to identical ranges (for example, $n = -2$ to $2$ and $p = -2$ to $2$) equation (B.12) can be rewritten as

$$\left[\bar{\bar{Q}} - \frac{1}{\omega\epsilon_2}\bar{\bar{I}}\right]\bar{B}_n = \bar{\bar{Q}}'\bar{B}_n = 0 \tag{B.14}$$

where the $B_n$'s are unknowns that represent the amplitudes of the spatial harmonics and

$$\bar{\bar{Q}}' = \begin{bmatrix} Q_{-2,-2} - \frac{1}{\omega\epsilon_2} & Q_{-2,-1} & Q_{-2,0} & Q_{-2,1} & Q_{-2,2} \\ Q_{-1,-2} & Q_{-1,-1} - \frac{1}{\omega\epsilon_2} & Q_{-1,0} & Q_{-1,1} & Q_{-1,2} \\ Q_{0,-2} & Q_{0,-1} & Q_{0,0} - \frac{1}{\omega\epsilon_2} & Q_{0,1} & Q_{0,2} \\ Q_{1,-2} & Q_{1,-1} & Q_{1,0} & Q_{1,1} - \frac{1}{\omega\epsilon_2} & Q_{1,2} \\ Q_{2,-2} & Q_{2,-1} & Q_{2,0} & Q_{2,1} & Q_{2,2} - \frac{1}{\omega\epsilon_2} \end{bmatrix} \tag{B.15}$$

Since the determinant of $\bar{\bar{Q}}'$ must be zero for non-trivial solutions of equation B.14, and all the entries in $\bar{\bar{Q}}'$ are functions of $\kappa$, the value of $\kappa$ that satisfies this zero determinant condition will be the solution of interest. Solving this eigenvalue equation can be challenging since $\kappa$ may be complex, and is beyond the scope of this thesis.

## B.2 Dispersion Equation for a Sinusoidally-modulated Sheet Impedance over a Grounded Dielectric Substrate

The formulation presented in the previous section if valid for an arbitrary, periodic variation of $\eta_{sheet}$. In the special case when $\eta_{sheet}$ varies sinusoidally,

$$\eta_{sheet} = jX_s(1 + M_s\cos(\frac{2\pi}{a})x) = jX_s + \frac{jX_sM_s}{2}(e^{j\frac{2\pi}{a}x} + e^{-j\frac{2\pi}{a}x}), \tag{B.16}$$

where $X_s$ is the average sheet reactance, and $M_s$ is the modulation factor for the sheet reactance. Substituting (B.16) this into (B.10), taking the inner product of the

resulting equation and $e^{j(\kappa + \frac{2\pi m}{a} x)}$ over one period, and invoking orthogonality yields

$$
\begin{aligned}
B_m \frac{k_{zm2}}{\omega \epsilon_2} =\; & jX_s B_m (-j)\frac{k_{zm2}}{k_{zm1}}\frac{\epsilon_1}{\epsilon_2}\cot(k_{zm1}d) - jX_s B_m \\
& + \frac{jX_s M_s}{2} B_{m+1}(-j)\frac{k_{z(m+1)2}}{k_{z(m+1)1}}\frac{\epsilon_1}{\epsilon_2}\cot(k_{z(m+1)1}d) - \frac{jX_s M_s}{2} B_{m+1} \\
& + \frac{jX_s M_s}{2} B_{m-1}(-j)\frac{k_{z(m-1)2}}{k_{z(m-1)1}}\frac{\epsilon_1}{\epsilon_2}\cot(k_{z(m-1)1}d) - \frac{jX_s M_s}{2} B_{m-1},
\end{aligned}
\tag{B.17}
$$

or equivalently,

$$
\begin{aligned}
0 =\; & \frac{jX_s M_s}{2}\left[(-j)\frac{k_{z(m-1)2}}{k_{z(m-1)1}}\frac{\epsilon_1}{\epsilon_2}\cot(k_{z(m-1)1}d) - 1\right]B_{m-1} \\
& + \frac{jX_s M_s}{2}\left[(-j)\frac{k_{z(m+1)2}}{k_{z(m+1)1}}\frac{\epsilon_1}{\epsilon_2}\cot(k_{z(m+1)1}d) - 1\right]B_{m+1} \\
& + \left[jX_s\left((-j)\frac{k_{zm2}}{k_{zm1}}\frac{\epsilon_1}{\epsilon_2}\cot(k_{zm1}d) - 1\right) - \frac{k_{zm2}}{\omega\epsilon_2}\right]B_m.
\end{aligned}
\tag{B.18}
$$

This infinite set of equations can be expressed as an eigenvalue equation,

$$
0 = 
\begin{bmatrix}
\ddots & \ddots & \vdots & \vdots & \vdots & \vdots & \\
\ddots & Q_{m-2} & P_{m-1} & 0 & 0 & 0 & \cdots \\
\ddots & P_{m-2} & Q_{m-1} & P_m & 0 & 0 & \cdots \\
\cdots & 0 & P_{m-1} & Q_m & P_{m+1} & 0 & \cdots \\
\cdots & 0 & 0 & P_m & Q_{m+1} & P_{m+2} & \ddots \\
\cdots & 0 & 0 & 0 & P_{m+1} & Q_{m+2} & \ddots \\
& \vdots & \vdots & \vdots & \vdots & \ddots & \ddots
\end{bmatrix}
\begin{bmatrix}
\vdots \\
B_{m-2} \\
B_{m-1} \\
B_m \\
B_{m+1} \\
B_{m+2} \\
\vdots
\end{bmatrix}.
\tag{B.19}
$$

Therefore, the dispersion equation can be expressed as

$$
P_{m-1}B_{m-1} + Q_m B_m + P_{m+1}B_{m+1} = 0
\tag{B.20}
$$

where

$$
P_m = \frac{jX_s M_s}{2}\left[(-j)\frac{k_{zm2}}{k_{zm1}}\frac{\epsilon_1}{\epsilon_2}\cot(k_{zm1}d) - 1\right],
\tag{B.21}
$$

$$Q_m = \left[ jX_s \left( (-j)\frac{k_{zm2}}{k_{zm1}}\frac{\epsilon_1}{\epsilon_2}\cot(k_{zm1}d) - 1 \right) - \frac{k_{zm2}}{\omega\epsilon_2} \right]. \tag{B.22}$$

Dividing (B.20) by $P_{m+1}B_m$ yields

$$\frac{P_{m+1}B_{m+1}}{P_{m+1}B_m} + \frac{Q_m B_m}{P_{m+1}B_m} + \frac{P_{m-1}B_{m-1}}{P_{m+1}B_m} = 0, \tag{B.23}$$

$$\frac{B_{m+1}}{B_m} + \frac{Q_m}{P_{m+1}} + \frac{P_{m-1}}{P_{m+1}}\frac{B_{m-1}}{B_m} = 0, \tag{B.24}$$

$$\frac{B_{m+1}}{B_m} = -\left( \frac{Q_m}{P_{m+1}} + \frac{P_{m-1}}{P_{m+1}}\frac{B_{m-1}}{B_m} \right). \tag{B.25}$$

Therefore,

$$\frac{B_m}{B_{m+1}} = -\frac{1}{\left( \frac{Q_m}{P_{m+1}} + \frac{P_{m-1}}{P_{m+1}}\frac{B_{m-1}}{B_m} \right)} = -\frac{1}{\frac{P_{m-1}}{P_{m+1}}\left( \frac{Q_m}{P_{m-1}} + \frac{B_{m-1}}{B_m} \right)}, \tag{B.26}$$

and

$$\frac{B_{m-1}}{B_m} = -\frac{1}{\left( \frac{Q_{m-1}}{P_m} + \frac{P_{m-2}}{P_m}\frac{B_{m-2}}{B_{m-1}} \right)} = -\frac{1}{\frac{P_{m-2}}{P_m}\left( \frac{Q_{m-1}}{P_{m-2}} + \frac{B_{m-2}}{B_{m-1}} \right)}. \tag{B.27}$$

Dividing (B.20) by $P_{m-1}B_m$ yields

$$\frac{P_{m+1}B_{m+1}}{P_{m-1}B_m} + \frac{Q_m B_m}{P_{m-1}B_m} + \frac{P_{m-1}B_{m-1}}{P_{m-1}B_m} = 0, \tag{B.28}$$

$$\frac{P_{m+1}B_{m+1}}{P_{m-1}B_m} + \frac{Q_m}{P_{m-1}} + \frac{B_{m-1}}{B_m} = 0, \tag{B.29}$$

$$\frac{B_{m-1}}{B_m} = -\left( \frac{P_{m+1}B_{m+1}}{P_{m-1}B_m} + \frac{Q_m}{P_{m-1}} \right), \tag{B.30}$$

and

$$\frac{B_m}{B_{m+1}} = -\left( \frac{P_{m+2}B_{m+2}}{P_m B_{m+1}} + \frac{Q_{m+1}}{P_m} \right). \tag{B.31}$$

Taking the inverse of (B.30) yields

$$\frac{B_m}{B_{m-1}} = \frac{-1}{\left(\frac{P_{m+1}B_{m+1}}{P_{m-1}B_m} + \frac{Q_m}{P_{m-1}}\right)} = \frac{-1}{\frac{P_{m+1}}{P_{m-1}}\left(\frac{Q_m}{P_{m+1}} + \frac{B_{m+1}}{B_m}\right)}. \tag{B.32}$$

Equating (B.26) to (B.30) yields

$$\frac{P_{m+2}}{P_m}\frac{B_{m+2}}{B_{m+1}} + \frac{Q_{m+1}}{P_m} = \frac{1}{\frac{Q_m}{P_{m+1}} + \frac{P_{m-1}}{P_{m+1}}\frac{B_{m-1}}{B_m}} \tag{B.33}$$

Taking the inverse of (B.33) yields

$$\frac{Q_m}{P_{m+1}} + \frac{P_{m-1}}{P_{m+1}}\frac{B_{m-1}}{B_m} = \frac{1}{\frac{P_{m+2}}{P_m}\frac{B_{m+2}}{B_{m+1}} + \frac{Q_{m+1}}{P_m}}, \tag{B.34}$$

$$\frac{Q_m}{P_{m+1}} = \frac{1}{\frac{P_{m+2}}{P_m}\frac{B_{m+2}}{B_{m+1}} + \frac{Q_{m+1}}{P_m}} - \frac{P_{m-1}}{P_{m+1}}\left[\frac{B_{m-1}}{B_m}\right]. \tag{B.35}$$

Substituting (B.27) into (B.35) yields

$$\frac{Q_m}{P_{m+1}} = \frac{1}{\frac{P_{m+2}}{P_m}\frac{B_{m+2}}{B_{m+1}} + \frac{Q_{m+1}}{P_m}} + \frac{\frac{P_{m-1}}{P_{m+1}}}{\frac{Q_{m-1}}{P_m} + \frac{P_{m-2}}{P_m}\frac{B_{m-2}}{B_{m-1}}}, \tag{B.36}$$

$$\frac{Q_m}{P_{m+1}} = \frac{1}{\frac{P_{m+2}}{P_m}\left(\frac{Q_{m+1}}{P_{m+2}} + \frac{B_{m+2}}{B_{m+1}}\right)} + \frac{1}{\frac{P_{m+1}}{P_{m-1}}\frac{P_{m-2}}{P_m}\left(\frac{Q_{m-1}}{P_{m-2}} + \frac{B_{m-2}}{B_{m-1}}\right)}, \tag{B.37}$$

$$Q_m = \frac{P_{m+1}}{\frac{P_{m+2}}{P_m}\left(\frac{Q_{m+1}}{P_{m+2}} + \left[\frac{B_{m+2}}{B_{m+1}}\right]\right)} + \frac{P_{m-1}}{\frac{P_{m-2}}{P_m}\left(\frac{Q_{m-1}}{P_{m-2}} + \left[\frac{B_{m-2}}{B_{m-1}}\right]\right)}. \tag{B.38}$$

Substituting expressions similar to (B.26) and (B.32) into (B.37) yields

$$Q_m = \cfrac{P_{m+1}}{\frac{P_{m+2}}{P_m}\left(\frac{Q_{m+1}}{P_{m+2}} - \cfrac{1}{\frac{P_{m+3}}{P_{m+1}}\left(\frac{Q_{m+2}}{P_{m+3}} - \cfrac{1}{\frac{P_{m+4}}{P_{m+2}}\left(\frac{Q_{m+3}}{P_{m+4}} + \left[\frac{B_{m+4}}{B_{m+3}}\right]\right)}\right)\right)}$$
$$+ \cfrac{P_{m-1}}{\frac{P_{m-2}}{P_m}\left(\frac{Q_{m-1}}{P_{m-2}} - \cfrac{1}{\frac{P_{m-3}}{P_{m-1}}\left(\frac{Q_{m-2}}{P_{m-3}} - \cfrac{1}{\frac{P_{m-4}}{P_{m-2}}\left(\frac{Q_{m-3}}{P_{m-4}} + \left[\frac{B_{m-4}}{B_{m-3}}\right]\right)}\right)\right)}, \tag{B.39}$$

or equivalently,

$$Q_m = \cfrac{P_{m+1}}{\frac{P_{m+2}}{P_m}\left(\frac{Q_{m+1}}{P_{m+2}} - \cfrac{1}{\frac{P_{m+3}}{P_{m+1}}\left(\frac{Q_{m+2}}{P_{m+3}} - \cfrac{1}{\frac{P_{m+4}}{P_{m+2}}\left(\frac{Q_{m+3}}{P_{m+4}} + \cdots\right)}\right)\right)}$$
$$+ \cfrac{P_{m-1}}{\frac{P_{m-2}}{P_m}\left(\frac{Q_{m-1}}{P_{m-2}} - \cfrac{1}{\frac{P_{m-3}}{P_{m-1}}\left(\frac{Q_{m-2}}{P_{m-3}} - \cfrac{1}{\frac{P_{m-4}}{P_{m-2}}\left(\frac{Q_{m-3}}{P_{m-4}} + \cdots\right)}\right)\right)} \tag{B.40}$$

Equation (B.40) is the dispersion equation (in continued fraction form) of a sinusoidally varying sheet impedance over a grounded dielectric substrate.

# Matrix Coefficients of the Eigenvalue equation and Relative Amplitudes of Fresnel Coefficients for a PCTIS

## C.1   Matrix coefficients

The elements of $\bar{\bar{a}}$ from (3.26) are given by (C.1).

$$
\begin{aligned}
a_{11} =&\epsilon_1\omega\left[jk_2^4k_y(k_x^2+k_y^2)k_{z1}\mu_1\sin\left(k_{z1}d\right)\right.\\
&\left.+k_2^2(k_x^2+k_y^2)k_{z2}\mu_2\left(k_1^2k_y\cos\left(k_{z1}d\right)+jk_{z1}\mu_1w(k_xY_{yx}^s+k_yY_{yy}^s)\sin\left(k_{z1}d\right)\right)\right]\\
a_{12} =&\mu_1\left[-\epsilon_1k_2^2k_x(k_x^2+k_y^2)k_{z1}k_{z2}\mu_2\omega^2\cos\left(k_{z1}d\right)+\right.\\
&\left.jk_1^2\left(-\epsilon_2k_x(k_x^2+k_y^2)k_{z2}^2\mu_2\omega^2+k_2^2(k_x^2+k_y^2)k_{z2}\mu_2\omega(k_yY_{yx}^s-k_xY_{yy}^s)\right)\sin\left(k_{z1}d\right)\right]\\
a_{21} =&\epsilon_1\omega\left[jk_2^4k_x(k_x^2+k_y^2)k_{z1}\mu_1\sin\left(k_{z1}d\right)\right.\\
&\left.+k_2^2(k_x^2+k_y^2)k_{z2}\mu_2\left(k_1^2k_x\cos\left(k_{z1}d\right)+jk_{z1}\mu_1w(k_xY_{xx}^s+k_yY_{xy}^s)\sin\left(k_{z1}d\right)\right)\right]\\
a_{22} =&\mu_1\left[\epsilon_1k_2^2k_y(k_x^2+k_y^2)k_{z1}k_{z2}\mu_2\omega^2\cos\left(k_{z1}d\right)+\right.\\
&\left.jk_1^2\left(\epsilon_2k_y(k_x^2+k_y^2)k_{z2}^2\mu_2\omega^2+k_2^2(k_x^2+k_y^2)k_{z2}\mu_2\omega(k_yY_{xx}^s-k_xY_{xy}^s)\right)\sin\left(k_{z1}d\right)\right]
\end{aligned}
$$

$$(C.1)$$

## C.2 Relative Amplitudes of Fresnel Coefficients

The relative amplitudes of the Fresnel coefficients from illumination I (3.44) (in Chapter III) are given by:

$$
\begin{aligned}
\frac{B_I}{A_I} &= \frac{4e^{(3jk_1d)}k_2\mu_1(k_1\mu_2\cos{(k_1d)} + j\mu_1(k_2 + \mu_2\omega Y_{yy}^s)\sin{(k_1d)})}{U}\\[4pt]
\frac{C_I}{A_I} &= \frac{4e^{(3jk_1d)}jk_2\mu_1^2\mu_2\omega Y_{yx}^s\sin{(k_1d)}}{U}\\[4pt]
\frac{D_I}{A_I} &= \frac{4e^{(jk_1d)}k_2\mu_1(k_1\mu_2\cos{(k_1d)} + j\mu_1(k_2 + \mu_2\omega Y_{yy}^s)\sin{(k_1d)})}{U}\\[4pt]
\frac{E_I}{A_I} &= \frac{4e^{(jk_1d)}jk_2\mu_1^2\mu_2\omega Y_{yx}^s\sin{(k_1d)}}{U}\\[4pt]
\frac{F_I}{A_I} &= 2e^{(2jk_1d)}\left[-2k_1^2\mu_2^2\cos{(k_1d)}^2\right.\\[4pt]
&\qquad\qquad +2j^2\mu_1^2(k_2^2 + k_2\mu_2\omega(-Y_{xx}^s + Y_{yy}^s)\\[4pt]
&\qquad\qquad +\mu_2^2\omega^2(Y_{xy}^s Y_{yx}^s - Y_{xx}^s Y_{yy}^s))\sin{(k_1d)}^2\\[4pt]
&\qquad\qquad \left. -jk_1\mu_1\mu_2^2\omega(Y_{xx}^s + Y_{yy}^s)\sin{(2k_1d)}\right]/U\\[4pt]
\frac{G_I}{A_I} &= \frac{8e^{(2jk_1d)}j^2k_2\mu_1^2\mu_2\omega Y_{yx}^s\sin{(k_1d)}^2}{U}\\[4pt]
U &= 4e^{(2djk_1)}(j\mu_1\sin{(k_1d)}\left[j\mu_1\sin{(k_1d)}(k_2^2 + k_2\mu_2\omega(Y_{xx}^s + Y_{yy}^s)\right.\\[4pt]
&\qquad +\mu_2^2\omega^2(Y_{xx}^s Y_{yy}^s - Y_{xy}^s Y_{yx}^s)) + k_1\mu_2^2\omega(Y_{xx}^s + Y_{yy}^s)\cos{(k_1d)}\Big]\\[4pt]
&\qquad + 4e^{(2jk_1d)}\left[jk_1k_2\mu_1\mu_2\sin{(2k_1d)} + k_1^2\mu_2^2\cos^2{(k_1d)}\right]
\end{aligned}
$$

(C.2)

The relative amplitudes of the Fresnel coefficients from illumination II (3.48) (in

Chapter III) are given by:

$$\frac{B_{II}}{A_{II}} = \frac{4e^{(3jk_1d)}jk_2\mu_1^2\mu_2\omega Y_{xy}^s \sin(k_1d)}{U}$$

$$\frac{C_{II}}{A_{II}} = \frac{4e^{(3jk_1d)}k_2\mu_1(k_1\mu_2\cos(k_1d) + j\mu_1(k_2 + \mu_2\omega Y_{xx}^s)\sin(k_1d))}{U}$$

$$\frac{D_{II}}{A_{II}} = \frac{4e^{(jk_1d)}jk_2\mu_1^2\mu_2\omega Y_{xy}^s \sin(k_1d)}{U}$$

$$\frac{E_{II}}{A_{II}} = \frac{4e^{(jk_1d)}k_2\mu_1(k_1\mu_2\cos(k_1d) + j\mu_1(k_2 + \mu_2\omega Y_{xx}^s)\sin(k_1d))}{U}$$

$$\frac{F_{II}}{A_{II}} = \frac{8e^{(2jk_1d)}j^2k_2\mu_1^2\mu_2\omega Y_{xy}^s \sin(k_1d)^2}{U}$$

$$\frac{G_{II}}{A_{II}} = 2e^{(2jk_1d)}\left[-2k_1^2\mu_2^2\cos(k_1d)^2\right. \tag{C.3}$$

$$+2j^2\mu_1^2(k_2^2 + k_2\mu_2\omega(-Y_{xx}^s + Y_{yy}^s)$$

$$+\mu_2^2\omega^2(Y_{xy}^sY_{yx}^s - Y_{xx}^sY_{yy}^s))\sin(k_1d)^2$$

$$\left.-jk_1\mu_1\mu_2^2\omega(Y_{xx}^s + Y_{yy}^s)\sin(2k_1d)\right]/U$$

$$U = 4e^{(2djk_1)}(j\mu_1\sin(k_1d)\left[j\mu_1\sin(k_1d)(k_2^2 + k_2\mu_2\omega(Y_{xx}^s + Y_{yy}^s)\right.$$

$$+\mu_2^2\omega^2(Y_{xx}^sY_{yy}^s - Y_{xy}^sY_{yx}^s)) + k_1\mu_2^2\omega(Y_{xx}^s + Y_{yy}^s)\cos(k_1d)\right]$$

$$+ 4e^{(2jk_1d)}\left[jk_1k_2\mu_1\mu_2\sin(2k_1d) + k_1^2\mu_2^2\cos^2(k_1d)\right]$$

# APPENDIX D

# Alternate Derivation for Sheet Impedance Extraction using an Equivalent Transmission-Line

In this appendix, an alternative method for deriving the sheet extraction formula (3.65) using an equivalent transmission-line model is discussed. Assume an arbitrary tensor sheet admittance is given by

$$\overline{\overline{Y}}_{sheet} = \begin{pmatrix} Y_{xx}^s & Y_{xy}^s \\ Y_{yx}^s & Y_{yy}^s \end{pmatrix}. \tag{D.1}$$

Diagonalizing this matrix yields

$$\overline{\overline{Y^d}}_{sheet} = \begin{pmatrix} Y_{xx}^s{}' & 0 \\ 0 & Y_{yy}^s{}' \end{pmatrix}, \tag{D.2}$$

where

$$
\begin{aligned}
Y_{xx}^s{}' &= \frac{Y_{xx}^s + Y_{yy}^s - \sqrt{Y_{xx}^{s\,2} + 4Y_{xy}^s Y_{yx}^s - 2Y_{xx}^s Y_{yy}^s + Y_{yy}^{s\,2}}}{2} \\
Y_{yy}^s{}' &= \frac{Y_{xx}^s + Y_{yy}^s + \sqrt{Y_{xx}^{s\,2} + 4Y_{xy}^s Y_{yx}^s - 2Y_{xx}^s Y_{yy}^s + Y_{yy}^{s\,2}}}{2}
\end{aligned}
\tag{D.3}
$$
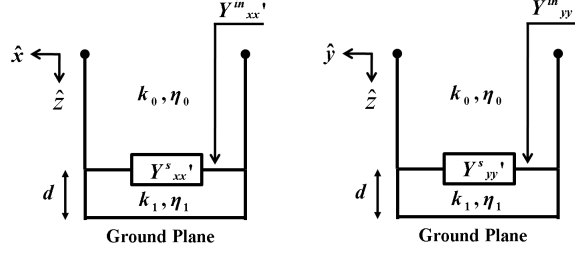
Figure D.1: Two orthogonal transmission-line models representing the diagonalized sheet impedance over a grounded dielectric substrate.

This diagonalized tensor sheet admittance over a grounded dielectric substrate can be represented by two orthogonal transmission lines (Fig. D.1) when the electric field is aligned with the principal axes of the sheet. Applying (2.11) from Chapter II to each transmission line separately, the following equation can be written.

$$
\begin{pmatrix} Y_{xx}^{in}{}' & 0 \\ 0 & Y_{yy}^{in}{}' \end{pmatrix} = \begin{pmatrix} Y_{xx}^{s}{}' & 0 \\ 0 & Y_{yy}^{s}{}' \end{pmatrix} + \begin{pmatrix} \frac{k_1 \cot k_1 d}{j\mu_1\omega} & 0 \\ 0 & \frac{k_1 \cot k_1 d}{j\mu_1\omega} \end{pmatrix}. \tag{D.4}
$$

Simplifying and rotating back to the original axes yields

$$
\begin{pmatrix} Y_{xx}^{in} & Y_{xy}^{in} \\ Y_{yx}^{in} & Y_{yy}^{in} \end{pmatrix} = \begin{pmatrix} Y_{xx}^{s} + \frac{k_1 \cot k_1 d}{j\mu_1\omega} & Y_{xy}^{s} \\ Y_{yx}^{s} & Y_{yy}^{s} + \frac{k_1 \cot k_1 d}{j\mu_1\omega} \end{pmatrix}. \tag{D.5}
$$

$$
= \overline{\overline{Y}}_{sheet} + \begin{pmatrix} \frac{1}{j\eta_1 \tan(k_1 d)} & 0 \\ 0 & \frac{1}{j\eta_1 \tan(k_1 d)} \end{pmatrix}, \tag{D.6}
$$

which agrees with (3.65) in Chapter III (Section 3.4).

163

# APPENDIX E

# Alternate Tensor Sheet Impedance Extraction Method using a Reflection Coefficient Matrix

A method for extracting the tensor sheet impedance of an arbitrarily patterned metallic cladding was presented in Section 3.4 of Chapter III. An alternate method is presented here. A normally incident plane wave is being reflected from a PCTIS as shown in Fig. 3.6. The electric and magnetic field at the surface ($z = 0$) of a printed-circuit tensor impedance surface (PCTIS) can be represented as a superposition of incident and reflected waves,

$$\begin{pmatrix} H_y \\ H_x \end{pmatrix} = \begin{pmatrix} H_y^+ \\ H_x^+ \end{pmatrix} + \begin{pmatrix} H_y^- \\ H_x^- \end{pmatrix}, \tag{E.1}$$

$$\begin{pmatrix} E_x \\ E_y \end{pmatrix} = \begin{pmatrix} E_x^+ \\ E_y^+ \end{pmatrix} + \begin{pmatrix} E_x^- \\ E_y^- \end{pmatrix}, \tag{E.2}$$

where "+" denotes the incident waves (traveling in the -z direction) and "-" denotes the reflected waves (traveling in the +z direction). The components of the incident electric field are related to the components of the reflected electric field by

$$\begin{pmatrix} E_x^- \\ E_y^- \end{pmatrix} = \begin{pmatrix} \Gamma_{xx} & \Gamma_{xy} \\ \Gamma_{yx} & \Gamma_{yy} \end{pmatrix} \begin{pmatrix} E_x^+ \\ E_y^+ \end{pmatrix}, \tag{E.3}$$

Applying Ampere's and Faraday's Law to plane waves yields,

$$\overline{E} = (-\hat{k} \times \overline{H})\eta, \tag{E.4}$$

$$\overline{H} = (\hat{k} \times \overline{E})\frac{1}{\eta}. \tag{E.5}$$

By substituting (E.4) into (E.3), the incident magnetic field can be related to the reflected magnetic field

$$\eta_0 \begin{pmatrix} H_y^- \\ -H_x^- \end{pmatrix} = \begin{pmatrix} \Gamma_{xx} & \Gamma_{xy} \\ \Gamma_{yx} & \Gamma_{yy} \end{pmatrix} \eta_0 \begin{pmatrix} -H_y^+ \\ H_x^+ \end{pmatrix}, \tag{E.6}$$

and consequently,

$$\begin{pmatrix} H_y^- \\ H_x^- \end{pmatrix} = \begin{pmatrix} -\Gamma_{xx} & \Gamma_{xy} \\ \Gamma_{yx} & -\Gamma_{yy} \end{pmatrix} \begin{pmatrix} H_y^+ \\ H_x^+ \end{pmatrix}. \tag{E.7}$$

Since the total magnetic field is given by,

$$\begin{pmatrix} H_y \\ H_x \end{pmatrix} = \begin{pmatrix} H_y^+ \\ H_x^+ \end{pmatrix} + \begin{pmatrix} H_y^- \\ H_x^- \end{pmatrix}, \tag{E.8}$$

it can be written as

$$\begin{pmatrix} H_y \\ H_x \end{pmatrix} = \left[ \begin{pmatrix} 1 & 0 \\ 0 & 1 \end{pmatrix} + \begin{pmatrix} -\Gamma_{xx} & \Gamma_{xy} \\ \Gamma_{yx} & -\Gamma_{yy} \end{pmatrix} \right] \begin{pmatrix} H_y^+ \\ H_x^+ \end{pmatrix}, \tag{E.9}$$

$$\begin{pmatrix} -H_y \\ H_x \end{pmatrix} = \left[ \begin{pmatrix} -1 & 0 \\ 0 & 1 \end{pmatrix} + \begin{pmatrix} \Gamma_{xx} & -\Gamma_{xy} \\ \Gamma_{yx} & -\Gamma_{yy} \end{pmatrix} \right] \begin{pmatrix} H_y^+ \\ H_x^+ \end{pmatrix}. \tag{E.10}$$

Given that

$$\begin{pmatrix} H_y^+ \\ H_x^+ \end{pmatrix} = \frac{1}{\eta_0} \begin{pmatrix} -E_x^+ \\ E_y^+ \end{pmatrix}, \tag{E.11}$$

the magnetic field can be written as

$$\begin{pmatrix} -H_y \\ H_x \end{pmatrix} = \left[ \begin{pmatrix} -1 & 0 \\ 0 & 1 \end{pmatrix} + \begin{pmatrix} \Gamma_{xx} & -\Gamma_{xy} \\ \Gamma_{yx} & -\Gamma_{yy} \end{pmatrix} \right] \begin{pmatrix} -E_x^+ \\ E_y^+ \end{pmatrix} \frac{1}{\eta_0}, \tag{E.12}$$

$$\begin{pmatrix} -H_y \\ H_x \end{pmatrix} = \left[ \begin{pmatrix} 1 & 0 \\ 0 & 1 \end{pmatrix} + \begin{pmatrix} -\Gamma_{xx} & -\Gamma_{xy} \\ -\Gamma_{yx} & -\Gamma_{yy} \end{pmatrix} \right] \begin{pmatrix} E_x^+ \\ E_y^+ \end{pmatrix} \frac{1}{\eta_0}. \tag{E.13}$$

Similarly, the total electric field at the surface can be expressed in terms of the incident electric field as

$$\begin{pmatrix} E_x \\ E_y \end{pmatrix} = \left[ \begin{pmatrix} 1 & 0 \\ 0 & 1 \end{pmatrix} + \begin{pmatrix} \Gamma_{xx} & \Gamma_{xy} \\ \Gamma_{yx} & \Gamma_{yy} \end{pmatrix} \right] \begin{pmatrix} E_x^+ \\ E_y^+ \end{pmatrix}. \tag{E.14}$$

At normal incidence, the tensor admittance boundary condition is given by

$$\begin{pmatrix} -H_y \\ H_x \end{pmatrix} = \overline{\overline{Y}}^{in} \begin{pmatrix} E_x \\ E_y \end{pmatrix} = \begin{pmatrix} Y_{xx}^{in} & Y_{xy}^{in} \\ Y_{yx}^{in} & Y_{yy}^{in} \end{pmatrix} \begin{pmatrix} E_x \\ E_y \end{pmatrix}. \tag{E.15}$$

Substituting (E.13) and (E.14) into (E.15) yields

$$\left[ \begin{pmatrix} 1 & 0 \\ 0 & 1 \end{pmatrix} + \begin{pmatrix} -\Gamma_{xx} & -\Gamma_{xy} \\ -\Gamma_{yx} & -\Gamma_{yy} \end{pmatrix} \right] \frac{1}{\eta_0} \begin{pmatrix} E_x^+ \\ E_y^+ \end{pmatrix} = \begin{pmatrix} Y_{xx}^{in} & Y_{xy}^{in} \\ Y_{yx}^{in} & Y_{yy}^{in} \end{pmatrix} \left[ \begin{pmatrix} 1 & 0 \\ 0 & 1 \end{pmatrix} + \begin{pmatrix} \Gamma_{xx} & \Gamma_{xy} \\ \Gamma_{yx} & \Gamma_{yy} \end{pmatrix} \right] \begin{pmatrix} E_x^+ \\ E_y^+ \end{pmatrix}, \tag{E.16}$$

$$
\left[ \begin{pmatrix} 1 & 0 \\ 0 & 1 \end{pmatrix} + \begin{pmatrix} -\Gamma_{xx} & -\Gamma_{xy} \\ -\Gamma_{yx} & -\Gamma_{yy} \end{pmatrix} \right] \frac{1}{\eta_0} = \begin{pmatrix} Y^{in}_{xx} & Y^{in}_{xy} \\ Y^{in}_{yx} & Y^{in}_{yy} \end{pmatrix} \left[ \begin{pmatrix} 1 & 0 \\ 0 & 1 \end{pmatrix} + \begin{pmatrix} \Gamma_{xx} & \Gamma_{xy} \\ \Gamma_{yx} & \Gamma_{yy} \end{pmatrix} \right].
$$

(E.17)

Solving for the input admittance tensor, $\overline{\overline{Y}}_{in}$ yields

$$
\begin{pmatrix} Y^{in}_{xx} & Y^{in}_{xy} \\ Y^{in}_{yx} & Y^{in}_{yy} \end{pmatrix} = Y_0 \begin{pmatrix} 1 - \Gamma_{xx} & -\Gamma_{xy} \\ -\Gamma_{yx} & 1 - \Gamma_{yy} \end{pmatrix} \begin{pmatrix} 1 + \Gamma_{xx} & \Gamma_{xy} \\ \Gamma_{yx} & 1 + \Gamma_{yy} \end{pmatrix}^{-1}.
$$

(E.18)

The value of $\overline{\overline{Y}}_{in}$ can be found from (E.18), once the reflection coefficients, $\Gamma_{xx}$, $\Gamma_{xy}$, $\Gamma_{yx}$, and $\Gamma_{yy}$ are known. These reflection coefficients can be found from two normal incidence scattering simulations or measurements. For example, $\Gamma_{yx}$ represents how much $y$-polarized field is reflected due to an incident $x$-polarized incident field.

# APPENDIX F

# Useful expressions for Calculating Group Velocity and Power Flow along TIBCs and PCTISs

## F.1 Useful derivatives for calculating group velocity of an idealized TIBC

The following expressions can be used in (4.53) and (4.54) to find the group velocity of a TIBC.

$$q = x \text{ or } y, r = \begin{cases} y \text{ if } q = x \\ x \text{ if } q = y \end{cases} \tag{F.1}$$

$$\frac{\partial k_2}{\partial k_q} = \frac{k_2}{\omega} \frac{\partial \omega}{\partial k_q} \tag{F.2}$$

$$\frac{\partial k_2^2}{\partial k_q} = \frac{2k_2^2}{\omega} \frac{\partial \omega}{\partial k_q} \tag{F.3}$$

$$\frac{\partial k_{z2}}{\partial k_q} = \frac{\frac{k_2^2}{\omega} \frac{\partial \omega}{\partial k_q} - k_q}{k_{z2}} \tag{F.4}$$

If the surface impedance is inductive and only a function of frequency:

168

$$\frac{\partial Y_{**}}{\partial k_q} = -\frac{Y_{**}}{\omega}\frac{\partial \omega}{\partial k_q} \tag{F.5}$$

Table F.1: Variables in the group velocity expression (4.71) of a TIBC

| $Variable$ | $TIS$ |
|---|---|
| $\chi_1$ | $-Y_{qq}/\omega$ |
| $\chi_2$ | $-Y_{qr}/\omega$ |
| $\chi_3$ | $-Y_{rq}/\omega$ |
| $\chi_4$ | $-Y_{rr}/\omega$ |
| $\xi_1$ | $0$ |
| $\xi_2$ | $0$ |
| $\xi_4$ | $0$ |
| $\nu$ | $k_2^2/(\omega k_{z2})$ |
| $\zeta$ | $k_2/\omega$ |
| $B_1$ | $k_2^2 Y_2 - k_q^2 Y_2 + k_2 k_{z2} Y_{rr}$ |
| $B_2$ | $k_q k_r Y_2 + k_2 k_{z2} Y_{rq}$ |
| $B_3$ | $k_2^2 Y_2 - k_r^2 Y_2 + k_2 k_{z2} Y_{qq}$ |
| $B_4$ | $(Y_2^2 + \det Y)k_2$ |
| $B_5$ | $2k_2 Y_2 (Y_{qq} + Y_{rr}) + k_{z2}(Y_2^2 + \det Y)$ |
| $B_6$ | $k_q k_r Y_2 + k_2 k_{z2} Y_{qr}$ |
| $B_7$ | $-Y_2(2k_q Y_{qq} + k_r(Y_{qr} + Y_{rq}))$ |

## F.2 Useful expressions for calculating group velocity of idealized PCTIS

The following expressions can be used in (4.67)-(4.70) to find the group velocity of a PCTIS.

$$q = x \text{ or } y, r = \begin{cases} y \text{ if } q = x \\ x \text{ if } q = y \end{cases} \tag{F.6}$$

$$\frac{\partial k_1}{\partial k_q} = \frac{k_1}{\omega}\frac{\partial \omega}{\partial k_q} \tag{F.7}$$

$$\frac{\partial k_1^2}{\partial k_q} = \frac{2k_1^2}{\omega}\frac{\partial \omega}{\partial k_q} \tag{F.8}$$

$$\frac{\partial k_{z1}}{\partial k_q} = \frac{\frac{k_1^2}{\omega}\frac{\partial \omega}{\partial k_q} - k_q}{k_{z2}} \tag{F.9}$$

$$C = \cot(k_{z1}d) \tag{F.10}$$

$$D = k_1^2 - k_y^2 \tag{F.11}$$

$$E = \frac{1}{k_1} \tag{F.12}$$

$$F = \frac{1}{k_{z1}} \tag{F.13}$$

$$G = k_x k_y \tag{F.14}$$

$$J = k_1^2 - k_x^2 \tag{F.15}$$

$$M = \frac{1}{k_1 k_{z1}^3 \omega} \tag{F.16}$$

$$\frac{\partial E}{\partial k_q} = -\frac{1}{\omega k_1} \frac{\partial \omega}{\partial k_q} \tag{F.17}$$

$$\frac{\partial F}{\partial k_q} = -\frac{1}{k_{z1}^3} \left( \frac{k_1^2}{\omega} \frac{\partial \omega}{\partial k_q} - k_q \right) \tag{F.18}$$

$$\frac{\partial C}{\partial k_q} = -\csc^2(k_{z1}d) \frac{d}{k_{z1}} \left( \frac{k_1^2}{\omega} \frac{\partial \omega}{\partial k_q} - k_q \right) \tag{F.19}$$

$$\frac{\partial D}{\partial k_x} = 2 \frac{k_1^2}{\omega} \frac{\partial \omega}{\partial k_x} \tag{F.20}$$

$$\frac{\partial D}{\partial k_y} = 2\frac{k_1^2}{\omega}\frac{\partial \omega}{\partial k_y} - 2k_y \tag{F.21}$$

$$\frac{\partial J}{\partial k_x} = 2\frac{k_1^2}{\omega}\frac{\partial \omega}{\partial k_x} - 2k_x \tag{F.22}$$

$$\frac{\partial J}{\partial k_y} = 2\frac{k_1^2}{\omega}\frac{\partial \omega}{\partial k_y} \tag{F.23}$$

$$\frac{\partial G}{\partial k_q} = k_r \tag{F.24}$$

Assuming a capacitive sheet:

$$\frac{\partial Y_{**}^s}{\partial k_q} = \frac{Y_{**}^s}{\omega}\frac{\partial \omega}{\partial k_q} \tag{F.25}$$

Table F.2: Variables in group velocity expression (4.71) of a PCTIS

| $Variable$ | $PCTIS$ |
|---|---|
| $\chi_1$ | $jM\left(C(Dk_1^2 + Dk_{z1}^2 - 2k_1^2 k_{z1}^2)Y_1 - jk_1 k_{z1}^3 Y_{qq}^s + Dk_1^2 k_{z1} dY_1 \csc^2(k_{z1}d)\right)$ |
| $\chi_2$ | $jM(CG(k_1^2 + k_{z1}^2)Y_1 - jk_1 k_{z1}^3 Y_{qr}^s + Gk_1^2 k_{z1} dY_1 \csc^2(k_{z1}d))$ |
| $\chi_3$ | $jM(CG(k_1^2 + k_{z1}^2)Y_1 - jk_1 k_{z1}^3 Y_{rq}^s + Gk_1^2 k_{z1} dY_1 \csc^2(k_{z1}d))$ |
| $\chi_4$ | $jM(C(Jk_{z1}^2 + k_1^2(J - 2k_{z1}^2))Y_1 - jk_1 k_{z1}^3 Y_{qq}^s + Jk_1^2 k_{z1} dY_1 \csc^2(k_{z1}d))$ |
| $\xi_1$ | $-j\omega M(k_1^2 - k_r^2)k_q Y_1(C + k_{z1}d\csc^2(k_{z1}d))$ |
| $\xi_2$ | $-j\omega MY_1(CGk_q + Ck_r k_{z1}^2 + Gk_q k_{z1} d\csc^2(k_{z1}d))$ |
| $\xi_4$ | $-j\omega Mk_q Y_1(C((k_1^2 - k_q^2) - 2k_{z1}^2) + (k_1^2 - k_q^2)k_{z1}d\csc^2(k_{z1}d))$ |
| $\nu$ | $k_2^2/(\omega k_{z2})$ |
| $\zeta$ | $k_2/\omega$ |
| $B_1$ | $k_2^2 Y_2 - k_q^2 Y_2 + k_2 k_{z2}[Y_{rr}^s - \frac{jY_1 C}{k_1 k_{z1}}(k_1^2 - k_q^2)]$ |
| $B_2$ | $k_q k_r Y_2 + k_2 k_{z2}[Y_{rq}^s - \frac{jY_1 C}{k_1 k_{z1}}(k_q k_r)]$ |
| $B_3$ | $k_2^2 Y_2 - k_r^2 Y_2 + k_2 k_{z2}[Y_{qq}^s - \frac{jY_1 C}{k_1 k_{z1}}(k_1^2 - k_r^2)]$ |
| $B_4$ | $(Y_2^2 + [\frac{(\det Y^s)k_1 k_{z1} + CY_1(-Ck_1 k_{z1} Y_1 + j(k_q^2 Y_{qq}^s + k_q k_r(Y_{qr}^s + Y_{rq}^s) + k_r^2 Y_{rr}^s - k_1^2(Y_{qq}^s + Y_{rr}^s)))}{k_1 k_{z1}}])k_2$ |
| $B_5$ | $2k_2 Y_2[\frac{-jC(k_1^2 + k_{z1}^2)Y_1 + k_1 k_{z1}(Y_{qq}^s + Y_{rr}^s)}{k_1 k_{z1}}] + \frac{k_{z2}}{k_2}B_4$ |
| $B_6$ | $k_q k_r Y_2 + k_2 k_{z2}[Y_{qr}^s - \frac{jY_1 C}{k_1 k_{z1}}(k_q k_r)]$ |
| $B_7$ | $-Y_2(2k_q[Y_{qq}^s - \frac{jY_1 C}{k_1 k_{z1}}(k_1^2 - k_r^2)] + k_r[Y_{qr}^s + Y_{rq}^s - 2\frac{jY_1 C}{k_1 k_{z1}}(k_q k_r)])$ |

# BIBLIOGRAPHY

# BIBLIOGRAPHY

[1] (2005, April) Nasa dryden flight research center photo collection. [Online]. Available: http://www.dfrc.nasa.gov/Gallery/Photo/index.html

[2] V. G. Veselago, "The Electrodynamics of Substances With Simultaneously Negative Values of $\epsilon$ and $\mu$ ," *Sov. Phys. Usp.*, vol. 10, pp. 509–514, Jan.-Feb. 1968.

[3] R. A. Shelby, D. R. Smith, and S. Schultz, "Experimental verification of a negative index of refraction," *Science*, vol. 292, no. 5514, pp. 77–79, 2001. [Online]. Available: http://www.sciencemag.org/content/292/5514/77.abstract

[4] D. R. Smith, W. J. Padilla, D. C. Vier, S. C. Nemat-Nasser, and S. Schultz, "Composite medium with simultaneously negative permeability and permittivity," *Phys. Rev. Lett.*, vol. 84, pp. 4184–4187, May 2000. [Online]. Available: http://link.aps.org/doi/10.1103/PhysRevLett.84.4184

[5] S. Maci, G. Minatti, M. Casaletti, and M. Bosiljevac, "Metasurfing: Addressing waves on impenetrable metasurfaces," *IEEE Antennas and Wireless Propagation Letters*, vol. 10, pp. 1499–1502, 2011.

[6] C. L. Holloway, E. F. Kuester, J. A. Gordon, J. O'Hara, J. Booth, and D. R. Smith, "An overview of the theory and applications of metasurfaces: The two-dimensional equivalents of metamaterials," *IEEE Antennas and Propagation Magazine*, vol. 54, no. 2, pp. 10–35, Apr. 2012.

[7] R. Collin and F. Zucker, *Antenna Theory, Part II*, 3rd ed. New York, NY: McGraw-Hill, 1969.

[8] A. Oliner and A. Hessel, "Guided waves on sinusoidally-modulated reactance surfaces," *IRE Transactions on Antennas and Propagation*, vol. 7, no. 5, pp. 201–208, Dec. 1959.

[9] R. B. Hwang and S. T. Peng, "Guidance characteristics of two-dimensionally periodic impedance surface," *IEEE Transactions on Microwave Theory and Techniques*, vol. 47, no. 12, pp. 2503–2511, Dec. 1999.

[10] H. J. Bilow, "Guided waves on a planar tensor impedance surface," *IEEE Transactions on Antennas and Propagation*, vol. 51, no. 10, pp. 2788–2792, Oct. 2003.

[11] B. H. Fong, J. S. Colburn, J. J. Ottusch, J. L. Visher, and D. F. Sievenpiper, "Scalar and tensor holographic artificial impedance surfaces," *IEEE Transactions on Antennas and Propagation*, vol. 58, no. 10, pp. 3212–3221, Oct. 2010.

[12] D. R. Jackson and N. G. Alexopoulos, "Gain enhancement methods for printed-circuit antennas," *IEEE Transactions on Antennas and Propagation*, vol. 33, pp. 976–987, Sep. 1985.

[13] A. P. Feresidis and J. C. Vardaxoglou, "High gain planar antenna using optimized partially reflective surfaces," *IEEE Transactions on Antennas and Propagation*, vol. 148, pp. 345–350, Dec. 2001.

[14] D. R. Jackson and A. A. Oliner, "A leaky-wave analysis of the High-Gain Printed Antenna Configuration," *IEEE Transactions on Antennas and Propagation*, vol. 36, pp. 905–910, Jul. 1988.

[15] A. P. Feresidis, G. Goussetis, S. Wang, and J. C. Vardaxoglou, "Artificial Magnetic Conductor Surfaces and Their Application to Low-Profile High-Gain Planar Antennas," *IEEE Transactions on Antennas and Propagation*, vol. 53, pp. 209–215, Jan. 2005.

[16] D. Sievenpiper, J. Colburn, B. Fong, J. Ottusch, and J. Visher, "Holographic artificial impedance surfaces for conformal antennas," in *IEEE Antennas and Propagation Society International Symposium, 2005*, vol. 1B, Jul. 2005, pp. 256–259.

[17] J. S. Colburn, D. F. Sievenpiper, B. H. Fong, J. J. Ottusch, J. L. Visher, and P. R. Herz, "Advances in artificial impedance surface conformal antennas," in *IEEE Antennas and Propagation Society International Symposium, 2007*, Jun. 2007, pp. 3820–3823.

[18] J. S. Colburn, A. Lai, D. F. Sievenpiper, A. Bekaryan, B. H. Fong, J. J. Ottusch, and P. Tulythan, "Adaptive artificial impedance surface conformal antennas," in *IEEE Antennas and Propagation Society International Symposium, 2009. APSURSI '09.*, Jun. 2009, pp. 1–4.

[19] D. F. Sievenpiper, J. S. Colburn, B. H. Fong, J. J. Ottusch, and J. L. Visher, "Holographic artificial impedance surfaces for conformal antennas," in *IEEE Antennas and Propagation Society International Symposium (APSURSI), 2005*, Jul. 2005.

[20] G. Minatti, F. Caminita, M. Casaletti, and S. Maci, "Leaky wave circularly polarized antennas based on surface impedance modulation," in *ICECom, 2010 Conference Proceedings*, Sept. 2010, pp. 1–4.

[21] ——, "Spiral leaky-wave antennas based on modulated surface impedance," *IEEE Transactions on Antennas and Propagation*, vol. 59, no. 12, pp. 4436 – 4444, dec. 2011.

[22] B. H. Fong, J. S. Colburn, P. R. Herz, J. J. Oltusch, D. F. Sievepiper, and J. L. Visher, "Polarization controlling holographic artificial impedance surfaces," in *Antennas and Propagation Society International Symposium, 2007 IEEE*, Jun. 2007, pp. 3824–3827.

[23] M. Bosiljevac, M. Casaletti, F. Caminita, Z. Sipus, and S. Maci, "Non-uniform metasurface luneburg lens antenna design," *IEEE Transactions on Antennas and Propagation*, vol. 60, no. 9, pp. 4065–4073, Sep. 2012.

[24] J. S. Colburn, A. Lai, and D. F. Sievenpiper, "Adaptive Artificial Impedance Surface Conformal Antennas," in *IEEE Antennas and Propagation Society International Symposium, 2009. APSURSI '09.*, June 1-5 2009, pp. 1–4.

[25] D. F. Sievenpiper, J. H. Schaffner, H. J. Song, R. Y. Loo, and G. Tangonan, "Two-dimensional beam steering using an electrically tunable impedance surface," *IEEE Transactions on Antennas and Propagation*, vol. 51, no. 10, pp. 2713–2722, Oct. 2003.

[26] D. F. Sievenpiper, J. H. Schaffner, H. J. Song, R. Y. Loo, and G. Tangonan, "Two-Dimensional Beam Steering Using an Electrically Tunable Impedance Surface," *IEEE Transactions on Antennas and Propagation*, vol. 51, pp. 2713–2722, Oct. 2003.

[27] D. F. Sievenpiper, "Forward and backward leaky wave radiation with large effective aperture from an electronically tunable textured surface," *IEEE Transactions on Antennas and Propagation*, vol. 53, no. 1, pp. 236–247, Jan. 2005.

[28] D. F. Sievenpiper, J. Schaffner, J. J. Lee, and S. Livingston, "A steerable leaky-wave antenna using a tunable impedance ground plane," *IEEE Antennas and Wireless Propagation Letters*, vol. 1, no. 1, pp. 179–182, 2002.

[29] M. Casaletti, F. Caminita, S. Maci, M. Bosiljevac, and Z. Sipus, "New type of horn based on variable metasurface," in *2011 IEEE International Symposium on Antennas and Propagation (APSURSI)*, Jul. 2011, pp. 1048–1050.

[30] H. Mosallaei and K. Sarabandi, "Antenna miniaturization and bandwidth enhancement using a reactive impedance substrate," *IEEE Transactions on Antennas and Propagation*, vol. 52, no. 9, pp. 2403–2414, Sep. 2004.

[31] ——, "Novel artificial reactive impedance surface for miniaturized wideband planar antenna design: concept and characterization," in *IEEE Antennas and Propagation Society International Symposium, 2003*, vol. 2, Jun. 2003, pp. 403–406.

[32] K. Sarabandi, A. Buerkle, and H. Mosallaei, "Compact wideband uhf patch antenna on a reactive impedance substrate," *IEEE Antennas and Wireless Propagation Letters*, vol. 5, no. 1, pp. 503–506, Dec. 2006.

[33] J. B. Pendry, D. Schurig, and D. R. Smith, "Controlling electromagnetic fields," *Science*, vol. 312, pp. 1780–1782, Jun. 2006.

[34] D.-H. Kwon and D. H. Werner, "Transformation electromagnetics: An overview of the theory and applications," *IEEE Antennas and Propagation Magazine*, vol. 52, no. 1, pp. 24–46, Feb. 2010.

[35] M. Zedler and G. V. Eleftheriades, "Anisotropic transmission-line metamaterials for 2-d transformation optics applications," *Proceedings of the IEEE*, vol. 99, no. 10, pp. 1634–1645, Oct. 2011.

[36] G. Gok and A. Grbic, "Tensor transmission-line metamaterials," *IEEE Transactions on Antennas and Propagation*, vol. 58, no. 5, pp. 1559 –1566, May 2010.

[37] ——, "A printed beam-shifting slab designed using tensor transmission-line metamaterials," *IEEE Transactions on Antennas and Propagation*, vol. 61, no. 2, pp. 728–734, Feb.

[38] D.-H. Kwon and C. Emiroglu, "Non-orthogonal grids in two-dimensional transmission-line metamaterials," *IEEE Transactions on Antennas and Propagation*, vol. 60, no. 9, pp. 4210–4218, Sept. 2012.

[39] N. B. Kundtz, D. R. Smith, and J. B. Pendry, "Electromagnetic design with transformation optics," *Proceedings of the IEEE*, vol. 99, no. 10, pp. 1622–1633, Oct. 2011.

[40] R. Quarfoth and D. Sievenpiper, "Anisotropic surface impedance cloak," in *IEEE Antennas and Propagation Society International Symposium (APSURSI), 2012*, Jul. 2012, pp. 1–2.

[41] N. Marcuvitz, *Waveguide Handbook*. New York: McGraw-Hill, 1951.

[42] C. Walter, *Traveling Wave Antennas*. McGraw-Hill, 1965.

[43] A. A. Oliner and A. Hessel, "Guided Waves on Sinusoidally-Modulated Reactance Surfaces," *IRE Trans. on Antennas and Propagation*, vol. 7, pp. 201–208, Dec. 1959.

[44] C. Lee and H. Son, "Periodically slotted dielectrically filled parallel-plate waveguide as a leaky-wave antenna: E-polarization case," *IEEE Transactions on Antennas and Propagation*, vol. 47, pp. 171–178, Jan. 1999.

[45] Jong-Ing Lee, Ung-Hee Cho, and Young-Ki Cho, "Analysis for a dielectrically filled parallel-plate waveguide with finite number of periodic slots in its upper wall as a leaky-wave antenna," *IEEE Transactions on Antennas and Propagation*, vol. 47, pp. 701–706, Apr. 1999.

[46] J. Jacobsen, "Analytical, numerical, and experimental investigation of guided waves on a periodically strip-loaded dielectric slab," *IEEE Transactions on Antennas and Propagation*, vol. 18, pp. 370–388, May 1970.

[47] A. M. Patel and A. Grbic, "A printed leaky-wave antenna based on a sinusoidally-modulated reactance surface," *IEEE Transactions on Antennas and Propagation*, vol. 59, no. 6, pp. 2087–2096, Jun. 2011.

[48] ——, "A printed leaky-wave antenna with a sinusoidally modulated surface reactance," in *IEEE Antennas and Propagation Society International Symposium, 2009. APSURSI '09.*, Jun. 2009, pp. 1–4.

[49] J. S. Colburn, D. F. Sievenpiper, B. H. Fong, J. J. Ottusch, J. L. Visher, and P. R. Herz, "Advances in artificial impedance surface conformal antennas," in *IEEE Antennas and Propagation Society International Symposium (APSURSI), 2007*, Jun. 2007.

[50] M. Guglielmi and D. R. Jackson, "Broadside Radiation from Periodic Leaky-Wave Antennas," *IEEE Transactions on Antennas and Propagation*, vol. 41, pp. 31–37, Jan. 1993.

[51] S. Tretyakov, *Analytical Modeling in Applied Electromagnetics*, 2nd ed. Englewood Cliffs, NJ: Prentice-Hall, 1968.

[52] A. B. Yakovlev, M. Silveirinha, O. Luukkonen, C. Simovski, I. Nefedov, and S. Tretyakov, "Characterization of surface-wave and leaky-wave propagation on wire-medium slabs and mushroom structures based on local and nonlocal homogenization models," *IEEE Transactions on Microwave Theory and Techniques*, vol. 57, no. 11, pp. 2700 –2714, nov. 2009.

[53] A. M. Patel and A. Grbic, "Modeling and analysis of printed-circuit tensor impedance surfaces," *IEEE Transactions on Antennas and Propagation*, vol. 61, no. 1, pp. 211–220, Jan. 2013.

[54] ——, "Analytical modeling of a printed-circuit tensor impedance surface," in *IEEE MTT-S International Microwave Symposium Digest (MTT), 2012*, Jun. 2012, pp. 1–3.

[55] ——, "Dispersion analysis of printed-circuit tensor impedance surfaces," in *IEEE Antennas and Propagation Society International Symposium (APSURSI), 2012*, Jul. 2012, pp. 1–2.

[56] S. Maci, M. Caiazzo, A. Cucini, and M. Casaletti, "A pole-zero matching method for ebg surfaces composed of a dipole fss printed on a grounded dielectric slab," *IEEE Transactions on Antennas and Propagation*, vol. 53, no. 1, pp. 70–81, Jan. 2005.

[57] B. Stupfel, "Impedance boundary conditions for finite planar or curved frequency selective surfaces embedded in dielectric layers," *IEEE Transactions on Antennas and Propagation*, vol. 53, no. 11, pp. 3654 – 3663, nov. 2005.

[58] J. A. Kong, *Electromagnetic Wave Theory*. Cambridge, MA: EMW Publishing, 2008.

177

[59] X. Ni, N. K. Emani, A. V. Kildashev, A. Boltasseva, and V. M. Shalaev, "Broadband light bending with plasmonic nanoantennas," *Science*, vol. 335 (6067), p. 427, Jan. 2012.

[60] A. Taflove and S. C. Hagness, *Computational Electrodynamics: The Finite-Difference Time-Domain Method.* Norwood, MA: Artech House, 2005.

[61] S. Rudolph and A. Grbic, "The design of broadband, volumetric nri media using multiconductor transmission-line analysis," *IEEE Transactions on Antennas and Propagation*, vol. 58, no. 4, pp. 1144–1154, 2010.

[62] C. R. Brewitt-Taylor and P. B. Johns, "On the construction and numerical solution of transmission-line and lumped network models of maxwell's equations," *Int. J. Numer. Methods Eng.*, vol. 15, no. 1, pp. 13–30, 1980.

[63] W. Rotman, *The Channel Guide Antenna.* Cambridge, MA: Air force Cambridge Res. Center, Rept. E5054, January, 1950.

[64] R. C. Honey, *Horizontally Polarized Long Slot Array.* Menlo Park, CA: Stanford Res. Inst. Tech. Rept. 47, August, 1954.

[65] F. J. Zucker, "The guiding and radiation of surface waves," in *Proc. Symp. Mod. Advan. Microwave tech., Polytechnic Institute of Brooklyn*, Nov. 1954, pp. 403–436.

[66] L. O. Goldstone and A. A. Oliner, "Leaky wave antennas i: Rectangular waveguides," *IRE Transactions on Antennas and Propagation*, vol. AP, no. 7, pp. 307–319, Oct. 1959.

[67] ——, "Leaky wave antennas ii: Circular waveguides," *IRE Transactions on Antennas and Propagation*, vol. AP, no. 9, pp. 280–290, Oct. 1961.

[68] S. T. Peng, T. Tamir, and H. L. Bertoni, "Theory of periodic dielectric waveguides," *IEEE Transactions on Microwave Theory and Techniques*, vol. 23, no. 1, pp. 123–133, Jan. 1975.

[69] S.-T. Peng and A. A. Oliner, "Guidance and leakage properties of a class of open dielectric waveguides: Part i–mathematical formulations," *IEEE Transactions on Microwave Theory and Techniques*, vol. 29, no. 9, pp. 843–855, Sep. 1981.

[70] T. Itoh, "Spectral domain immitance approach for dispersion characteristics of generalized printed transmission lines," *IEEE Transactions on Microwave Theory and Techniques*, vol. 28, no. 7, pp. 733–736, Jul. 1980.

[71] T. Tamir and S. Zhang, "Modal transmission-line theory of multilayered grating structures," *Journal of Lightwave Technology*, vol. 14, no. 5, pp. 914–927, May 1996.

[72] Y.-J. Park, A. Herschlein, and W. Wiesbeck, "A photonic bandgap (pbg) structure for guiding and suppressing surface waves in millimeter-wave antennas," *IEEE Transactions on Microwave Theory and Techniques*, vol. 49, no. 10, pp. 1854–1859, Oct. 2001.

[73] R. Abhari and G. Eleftheriades, "Metallo-dielectric electromagnetic bandgap structures for suppression and isolation of the parallel-plate noise in high-speed circuits," *IEEE Transactions on Microwave Theory and Techniques*, vol. 51, no. 6, pp. 1629–1639, Jun. 2003.

[74] A. M. Patel and A. Grbic, "The effects of spatial dispersion on power flow along a printed-circuit tensor impedance surface (pctis)," *Manuscript in Preparation for IEEE Transactions on Antennas and Propagation*, 2013.

[75] G. Gok and A. Grbic, "Alternative material parameters for transformation electromagnetics designs," *Accepted to IEEE Transactions on Microwave Theory and Techniques*, vol. 61, no. 4, pp. 1–11, Apr. 2013.

[76] A. M. Patel and A. Grbic, "Transformation electromagnetics devices using tensor impedance surfaces," in *IEEE International Microwave Symposium, 2013.*, Jun. 2013.

[77] ——, "Effective surface impedance of a printed-circuit tensor impedance surface (pctis)," *Accepted for publication in IEEE Transactions on Microwave Theory and Techniques*, vol. 61, no. 4, pp. 1–11, Apr. 2013.

[78] D. J. Hoppe and Y. Rahmat-Samii, *Impedance Boundary Conditions in Electromagnetics*, 1st ed. Washington, DC: Taylor and Francis, 1995.

[79] G. Liu, C. Li, C. Chen, Z. Lu, and G. Fang, "Experimental verification of field rotating with invisibility by full tensor transmission-line metamaterials," *Applied Physics Letters*, vol. 101, no. 22, p. 224105, 2012. [Online]. Available: http://link.aip.org/link/?APL/101/224105/1

[80] M. Selvanayagam and G. Eleftheriades, "A sheared transmission-line metamaterial unit cell with a full material tensor," in *2011 IEEE International Symposium on Antennas and Propagation (APSURSI)*, July, pp. 2872–2875.

[81] ——, "Transmission-line metamaterials on a skewed lattice for transformation electromagnetics," *IEEE Transactions on Microwave Theory and Techniques*, vol. 59, no. 12, pp. 3272–3282, Dec. 2011.

[82] D. J. Gregoire and A. V. Kabakian, "Surface-wave waveguides," *IEEE Antennas and Wireless Propagation Letters*, vol. 10, pp. 1512–1515, 2011.

[83] M. Y. Wang, J. J. Zhang, H. Chen, Y. Luo, S. Xi, L. X. Ran, and J. A. Kong, "Design and application of a beam shifter by transformation media," *Progress In Electromagnetics Research*, vol. 83, pp. 147–155, 2008.

[84] A. M. Patel and A. Grbic, "Transformation electromagnetics devices based on printed-circuit tensor impedance surfaces," *Manuscript in Preparation for IEEE Transactions on Microwave Theory and Techniques*, 2013.

[85] B. Kuprel and A. Grbic, "Anisotropic inhomogeneous metamaterials using nonuniform transmission-line grids aligned with the principal axes," *IEEE Antennas and Wireless Propagation Letters*, vol. 11, pp. 358–361, 2012.